Scylla. III. The Outside-in Radial Age Gradient in the Small Magellanic Cloud and the Star Formation Histories of the Main Body, Wing, and Outer Regions

Roger Cohen, Kristen Mcquinn, Claire Murray, Benjamin Williams, Yumi Choi, Christina Lindberg, Clare Burhenne, Karl Gordon, Petia Yanchulova Merica-Jones, Caroline Bot, et al.

The Astrophysical Journal, 975:43 (30pp), 2024 November 1 https://doi.org/10.3847/1538-4357/ad76a6

Scylla. III. The Outside-in Radial Age Gradient in the Small Magellanic Cloud and the Star Formation Histories of the Main Body, Wing, and Outer Regions

Roger E. Cohen[1], Kristen B. W. McQuinn[1,2], Claire E. Murray[2,3], Benjamin F. Williams[4], Yumi Choi[5], Christina W. Lindberg[2,3], Clare Burhenne[1], Karl D. Gordon[2], Petia Yanchulova Merica-Jones[2], Caroline Bot[6], Andrew E. Dolphin[7,8], Karoline M. Gilbert[2,3], Steven Goldman[2], Alec S. Hirschauer[2], Karin M. Sandstrom[9], and O. Grace Telford[1,10,11,12]

[1] Department of Physics and Astronomy, Rutgers, The State University of New Jersey, 136 Frelinghuysen Road, Piscataway, NJ 08854, USA; rc1273@physics.rutgers.edu
[2] Space Telescope Science Institute, 3700 San Martin Drive, Baltimore, MD 21218, USA
[3] The William H. Miller III Department of Physics & Astronomy, Bloomberg Center for Physics and Astronomy, Johns Hopkins University, 3400 N. Charles Street, Baltimore, MD 21218, USA
[4] Department of Astronomy, University of Washington, Box 351580, U. W., Seattle, WA 98195-1580, USA
[5] NSF National Optical-Infrared Astronomy Research Laboratory, 950 N. Cherry Avenue, Tucson, AZ 85719, USA
[6] Observatoire Astronomique de Strasbourg, Université de Strasbourg, UMR 7550, 11 rue de l'Université, F-67000 Strasbourg, France
[7] Raytheon, 1151 E. Hermans Road, Tucson, AZ 85756, USA
[8] University of Arizona, Steward Observatory, 933 North Cherry Avenue, Tucson, AZ 85721, USA
[9] Department of Astronomy & Astrophysics, University of California San Diego, 9500 Gilman Drive, La Jolla, CA 92093, USA
[10] Department of Astrophysical Sciences, Princeton University, 4 Ivy Lane, Princeton, NJ 08544, USA
[11] The Observatories of the Carnegie Institution for Science, 813 Santa Barbara Street, Pasadena, CA 91101, USA
Received 2024 April 23; revised 2024 August 29; accepted 2024 August 30; published 2024 October 24

Abstract

The proximity of the Large and Small Magellanic Clouds (LMC and SMC) provides the opportunity to study the impact of dwarf–dwarf interactions on their mass assembly with a unique level of detail. To this end, we analyze two-filter broadband imaging of 83 Hubble Space Telescope (HST) pointings covering 0.203 deg^2 toward the SMC, extending out to ∼3.5 kpc in projection from its optical center. Lifetime star formation histories (SFHs) fit to each pointing independently reveal an outside-in age gradient such that fields in the SMC outskirts are older on average. We measure radial gradients of the look-back time to form 90%, 75%, and 50% of the cumulative stellar mass for the first time, finding $\delta(\tau_{90}, \tau_{75}, \tau_{50})/\delta R = (0.61^{+0.08}_{-0.07}, 0.65^{+0.09}_{-0.08}, 0.82^{+0.12}_{-0.16})$ Gyr kpc^{-1} assuming PARSEC evolutionary models and a commonly used elliptical geometry of the SMC, although our results are robust to these assumptions. The wing of the SMC deviates from this trend, forming 25% of its cumulative mass over the most recent 3 Gyr owing to a best-fit star formation rate that remains approximately constant. Our results are consistent with chemodynamical evidence of a tidally stripped SMC component in the foreground and imply contributions to the observed SFH from multiple previous LMC–SMC interactions. We also compare our SMC SFH with results from a companion study of the LMC, finding that while the two galaxies present different internal, spatially resolved SFH trends, both the LMC and SMC have similar near-constant lifetime SFHs when viewed globally.

Unified Astronomy Thesaurus concepts: Magellanic Clouds (990); Small Magellanic Cloud (1468); Galaxy evolution (594); Local Group (929)

1. Introduction

The evolution of dwarf galaxies is inextricably tied to their environment. The timeline of their mass assembly is fundamentally affected by their interactions, both with each other and with more massive hosts in a complex, multifaceted way (e.g., D. R. Weisz et al. 2015; M. Geha et al. 2017; C. Engler et al. 2023). A particularly prominent role, over cosmic time, is played by dwarf–dwarf interactions. Dwarfs contributed to galaxy growth via mergers in a hierarchical accretion scenario (e.g., A. R. Wetzel et al. 2015), including "satellites of satellites" (e.g., D. Martínez-Delgado et al. 2012; A. J. Deason et al. 2015; F. Annibali et al. 2016) and the coalescence of isolated groups of dwarfs that were more common in the past (S. Stierwalt et al. 2017). Through the present day, both observations and simulations suggest that interactions between gas-rich dwarfs trigger star formation. Observationally, paired dwarfs ($7 \leqslant \log_{10}M_\star/M_\odot \leqslant 9.7$) show enhanced star formation rates compared to their single counterparts regardless of environment (S. Stierwalt et al. 2015 and references therein; see also E. Kado-Fong et al. 2024). From a theoretical standpoint, cosmological simulations suggest that increased star formation in dwarfs ($7 \leqslant \log_{10}M_\star/M_\odot \leqslant 9.5$) can be caused by flybys without requiring a merger (G. Martin et al. 2021).

The Large and Small Magellanic Clouds (LMC and SMC), because of their proximity (≈50 and ≈62 kpc, respectively; R. de Grijs et al. 2014; R. de Grijs & G. Bono 2015), provide us with a uniquely detailed view of an ongoing dwarf–dwarf interaction. The LMC–SMC interaction has likely been a prolonged one, lasting as long as ∼6−7 Gyr based on simulations (G. Besla et al. 2012; J. D. Diaz & K. Bekki 2012). Importantly, this interaction substantially predates their infall into the Milky Way, entering its virial radius only

[12] Carnegie-Princeton Fellow.

$\sim$1−2 Gyr ago (N. Kallivayalil et al. 2006; G. Besla et al. 2007, 2012; E. Patel et al. 2017; but see E. Vasiliev 2024). Accordingly, many of the features we observe in the vicinity of the LMC and SMC are likely due to their interaction with each other rather than with the Milky Way, including a recent ($\sim$140 −160 Myr ago), near-direct (impact parameter $\sim$5 kpc) collision (P. Zivick et al. 2018; Y. Choi et al. 2022).

Among the plethora of interaction signatures imprinted in the morphology and chemodynamics of the LMC and SMC, some have been traced to particular past interactions. The Magellanic Bridge (J. V. Hindman et al. 1963) is thought to result from the most recent LMC–SMC collision $\sim$150 Myr ago based on its morphology, chemistry, and kinematics (G. Besla et al. 2012; J. D. Diaz & K. Bekki 2012; P. Zivick et al. 2018, 2019), although the presence of metal-poor massive O stars has been used to argue for some role of earlier interactions (V. Ramachandran et al. 2021). In contrast to the Bridge, the Magellanic Stream is thought to have been formed $\sim$1.5−2.5 Gyr ago, through some combination of tidal stripping from the LMC and SMC (D. L. Nidever et al. 2008; G. Besla et al. 2012; J. D. Diaz & K. Bekki 2012) and/or ram pressure stripping from the LMC and Milky Way (e.g., G. R. Meurer et al. 1985; S. Lucchini et al. 2020). In addition to the Bridge and the Stream, initially characterized based on the large-scale structure of their gaseous components, multiple LMC–SMC interactions have left many additional signatures in the morphology, chemistry, and kinematics of the Magellanic Clouds (e.g., K. A. G. Olsen & C. Salyk 2002; K. A. G. Olsen et al. 2011; P. D. Dobbie et al. 2014a; D. Mackey et al. 2018; M. De Leo et al. 2020; J. Grady et al. 2021; P. Massana et al. 2024). The LMC, as the more massive of the two, has survived repeated perturbations by the SMC with its disklike morphology and kinematics relatively intact (Y. Choi et al. 2018b, 2022). However, the structure of the less massive SMC is much more complex, with tidal stripping by the LMC likely playing an important role (e.g., N. E. D. Noël et al. 2013; P. Zivick et al. 2018, 2021; A. O. Omkumar et al. 2021; D. James et al. 2021; F. Niederhofer et al. 2021; C. E. Murray et al. 2024).

The highly disturbed nature of the SMC is underscored by its gas and dust properties: neutral hydrogen has a complex, position-dependent distance and velocity distribution (e.g., M. De Leo et al. 2020; N. M. Pingel et al. 2022; C. E. Murray et al. 2024), while the dust distribution is separate from the stellar distribution along the line of sight (P. Yanchulova Merica-Jones et al. 2021). The stellar distribution of the SMC shows plentiful evidence of past disturbances as well. Various stellar substructures have been discovered in the periphery of the SMC (D. Mackey et al. 2018; V. A. Belokurov & D. Erkal 2019; D. El Youssoufi et al. 2021; Gaia Collaboration et al. 2021; J. Grady et al. 2021), some of which show bimodalities in their abundances and/or kinematics (M. C. Parisi et al. 2015, 2016, 2022; A. Pieres et al. 2017; L. R. Cullinane et al. 2023; P. Massana et al. 2024), in addition to the shell-like structure $\sim$2° to the northeast (D. Martínez-Delgado et al. 2019; J. D. Sakowska et al. 2024).

Perhaps the most prominent stellar substructure of the SMC is its wing to the east in the direction of the Bridge (H. Shapley 1940). The wing hosts composite stellar populations (N. E. D. Noël et al. 2013) and is spatially and kinematically distinct from both the Bridge (e.g., T. Muraveva et al. 2018; A. O. Omkumar et al. 2021) and the inner SMC, showing residual motions toward the LMC beyond the tidal expansion seen also on the opposite (western) side of the SMC (M. S. Oey et al. 2018; M. De Leo et al. 2020; F. Niederhofer et al. 2021; Gaia Collaboration et al. 2021; P. Zivick et al. 2021; D. El Youssoufi et al. 2023). The structure of the wing is complex along the line of sight as well: although a substantial ($\gtrsim$5 kpc) and position-dependent line-of-sight depth is seen throughout the SMC (S. Subramanian & A. Subramaniam 2009, 2012; A. M. Jacyszyn-Dobrzeniecka et al. 2016, 2017; B. L. Tatton et al. 2021; D. El Youssoufi et al. 2021; P. Yanchulova Merica-Jones et al. 2021), the distance distribution toward the wing is bimodal. In particular, the magnitude distribution of red clump stars reveals a feature $\sim$10−12 kpc in front of the main body of the SMC along the line of sight (D. Hatzidimitriou & M. R. S. Hawkins 1989; D. L. Nidever et al. 2013; S. Subramanian et al. 2017; B. L. Tatton et al. 2021; D. El Youssoufi et al. 2021), and a bimodality is also seen in kinematics of red clump and red giant stars toward the wing (A. O. Omkumar et al. 2021; D. James et al. 2021; D. El Youssoufi et al. 2023). The most recent LMC–SMC collision, thought to have created the Bridge, is also likely responsible for the bimodalities in stellar distances and kinematics toward the wing. In particular, A. Almeida et al. (2024) claim that the foreground component originated in the inner SMC and was tidally stripped during the most recent LMC–SMC collision. Their claim is supported by trends in radial velocities and distances for the foreground component. The foreground component examined by A. Almeida et al. (2024) may extend from the innermost regions of the LMC, suggesting an approach toward the LMC at increasingly larger distances from the SMC center.

None of the bimodalities seen in stellar distances and chemodynamics toward the wing are present in the distribution of ancient RR Lyrae variables, although their distances are skewed toward the LMC in the vicinity of the wing (A. M. Jacyszyn-Dobrzeniecka et al. 2017; T. Muraveva et al. 2018). Viewed together with the cylindrical rotation seen in red giants in the inner SMC ($\lesssim$2 kpc; P. Zivick et al. 2018), the oldest stellar populations of the SMC appear to have been the least affected by LMC–SMC interactions. Accordingly, the stellar morphology of the SMC, viewed in projection, is highly age dependent. While old stars (red giants and RR Lyrae) have a shallow, negative radial metallicity gradient (e.g., S. Choudhury et al. 2020; P. Massana et al. 2024) and a relatively smooth, extended, symmetric projected spatial distribution, at younger ages the stellar distribution appears increasingly asymmetric, tracing the irregular H I distribution (J. Harris & D. Zaritsky 2004; M. Cignoni et al. 2013; S. Rubele et al. 2018; D. El Youssoufi et al. 2019; P. Massana et al. 2020).

It is clear from the above evidence that the distribution of stellar populations toward the SMC is complex, since it is both age dependent in a gross sense while also impacted, selectively, by LMC–SMC interactions. In this context, a powerful additional avenue for disentangling the history of the SMC and its interaction with the LMC is presented by star formation histories (SFHs) ascertained from photometry of resolved stars. With this in mind, the SMC has been the target of various imaging campaigns that have already yielded crucial insights on its past assembly and interaction history, including the Magellanic Clouds Photometric Survey (MCPS; J. Harris & D. Zaritsky 2004), the VISTA Survey of the Magellanic Clouds system (VMC; M.-R. L. Cioni et al. 2011), and the Survey of the MAgellanic Stellar History (SMASH; D. L. Nidever et al. 2017). Because such imaging campaigns can become crowding

limited in the innermost region of the SMC (e.g., P. Massana et al. 2022), additional insight has come from targeted Hubble Space Telescope (HST) imaging (M. P. McCumber et al. 2005; E. Chiosi & A. Vallenari 2007; E. Sabbi et al. 2009; M. Cignoni et al. 2012, 2013; D. R. Weisz et al. 2013), as well as deep ground-based observations of selected fields in the outer SMC (A. E. Dolphin et al. 2001; N. E. D. Noël et al. 2009). By trading spatial coverage for photometric depth, such observations, reaching faintward of the ancient ($\sim$13 Gyr) main-sequence turnoff (MSTO),[13] help break age–metallicity degeneracies in fitting resolved SFHs to simultaneously measure both stellar mass assembly history and chemical evolution over cosmic timescales (e.g., F. Annibali & M. Tosi 2022).

To date, both contiguous ground-based surveys and deep, targeted imaging toward the SMC have produced valuable constraints on the history of the LMC–SMC interaction. An interaction between the LMC and SMC $\sim$3−4 Gyr ago is evidenced by a global enhancement in star formation in the SMC (D. R. Weisz et al. 2013; P. Massana et al. 2022), with recent star formation concentrated near the center and the east toward the wing (M. Cignoni et al. 2013; S. Rubele et al. 2018; P. Massana et al. 2022), while at $\gtrsim$2 kpc from the SMC center, star formation has dramatically decreased over the past few gigayears (A. E. Dolphin et al. 2001; N. E. D. Noël et al. 2009). Based on SFH fits to six fields with deep HST imaging, M. Cignoni et al. (2013) suggest an outside-in gradient in mean age in the SMC, such that the outskirts (except for the wing) are older on average (see also R. Carrera et al. 2008; P. D. Dobbie et al. 2014b). In contrast to these results, A. E. Piatti (2012, 2015) claims a null radial age gradient among the SMC field population, although he does not attempt to quantify this result. In fact, despite various investigations of the spatially resolved SFH in the SMC field (J. Harris & D. Zaritsky 2004; R. Carrera et al. 2008; N. E. D. Noël et al. 2009; A. E. Piatti 2012; D. R. Weisz et al. 2013; M. Cignoni et al. 2013; A. E. Piatti 2015; S. Rubele et al. 2015, 2018; P. Massana et al. 2022), a radial age gradient in the SMC has yet to be quantified.

Given the extended and turbulent interaction history of the SMC, spatially resolved lifetime SFH measurements can provide important insights into the role of dwarf–dwarf interactions on the mass assembly of dwarf galaxies. Although current models of the LMC–SMC–Milky Way interaction lack realistic star formation prescriptions (G. Besla et al. 2012; J. D. Diaz & K. Bekki 2012), measurements of spatial trends in stellar age in the SMC (and LMC) provide quantitative constraints that must be met by future models. In addition, the latest zoom-in cosmological hydrodynamical simulations make predictions for radial age gradients in dwarf galaxies (A. S. Graus et al. 2019), but these predictions remain untested. While these simulations currently lack direct LMC–SMC–Milky Way analogs, empirical measurements of radial stellar age gradients in the SMC and LMC again provide important tests of such models for the limiting case of extended dwarf–dwarf interactions moving forward. Lastly, a comparison between SFH trends in the wing of the SMC versus other fields in the outer SMC, as well as the main body, can help discern which previous LMC–SMC interactions contributed to which present-day structures observed in the SMC (i.e., wing, main body).

This paper is the third in a series presenting results from Scylla, a multicycle pure-parallel HST campaign imaging 96 fields toward the LMC and SMC. In addition to an initial paper presenting an overview of the Scylla program (C. E. Murray et al. 2024), in a companion paper we present the spatially resolved SFH of the LMC (Cohen et al. 2024), combining our Scylla imaging with a plethora of archival HST imaging to detect and characterize spatial trends in the SFH of the LMC over its entire lifetime. Here we take a similar approach with the SMC, fitting SFHs individually to an ensemble of HST pointings and using the results to characterize spatial trends in the SFH of the SMC. This paper is organized as follows: We describe our observations and data reduction in Section 2, and we describe our methodology for SFH fitting in Section 3. In Section 4, we present our results, broken down both into subsets based on location in the SMC and for individual fields. In Section 5 we discuss constraints on the LMC–SMC interaction and place our SMC results in the context of other Local Group dwarfs, and our main conclusions are summarized in the final section. Throughout our analysis, we assume an SMC distance of 62 kpc (e.g., R. de Grijs & G. Bono 2015) and an elliptical geometry with an axis ratio of 2:1 and a position angle of 45° east of north (e.g., A. E. Piatti et al. 2005; A. E. Piatti 2012; B. Dias et al. 2014; M. C. Parisi et al. 2022) to assign a projected semimajor-axis equivalent distance $R_{\rm ell}^{\rm SMC}$ to each of our observed fields.

2. Data

2.1. Observations

To analyze spatial trends in the lifetime SFH of the SMC, we leverage new and archival imaging from 83 individual HST pointings consisting of deep imaging in at least two broadband filters. The spatial distribution of our fields is shown in Figure 1, centered on the SMC optical center of (R.A., decl.)$_{\rm J2000,optical}$ = (00:52:45, −72:49:43) (H. H. Crowl et al. 2001; S. Subramanian & A. Subramaniam 2012). In the top panel of Figure 1, our field locations are color coded by observational source (i.e., new or archival imaging, described below), overplotted on a density map built from Gaia DR3 (Gaia Collaboration et al. 2023).[14] We also indicate the locations of fields analyzed in previous targeted studies of spatial variations in the SFH of the SMC, including HST pointings from D. R. Weisz et al. (2013) and M. Cignoni et al. (2013) (which we reanalyze), and the ground-based fields analyzed by N. E. D. Noël et al. (2007, 2009). An ellipse corresponding to $R_{\rm ell}^{\rm SMC}$ = 2 kpc is shown as a dotted gray line to indicate the main body of the SMC.

The morphology of the SMC varies strongly as a function of stellar age. While old (red giants, red clump, and RR Lyrae) stellar populations show a smooth elliptical spatial distribution (D. Zaritsky et al. 2000; A. M. Jacyszyn-Dobrzeniecka et al. 2017), the spatial distribution of younger stars is much more clumpy and asymmetric, with young stars concentrated in both

[13] The MSTO occurs at absolute magnitudes of ($M_{\rm F475W}$, $M_{\rm F814W}$) = (4.15, 3.28) in the WFC3/UVIS filters used in our Scylla program and M_V = 3.90 assuming 13 Gyr PARSEC evolutionary models (A. Bressan et al. 2012) with [M/H] = −1.2.

[14] For the purposes of constructing an illustrative background density map, we used only very loose parallax and color–magnitude criteria to select Gaia sources: `parallax<0.1 AND parallax_over_error< 5 AND ruwe<1.4 AND (phot_bp_mean_mag−phot_rp_mean_mag) > −1.0 AND phot_g_mean_mag>10.6 AND phot_g_mean_mag<19.0`.

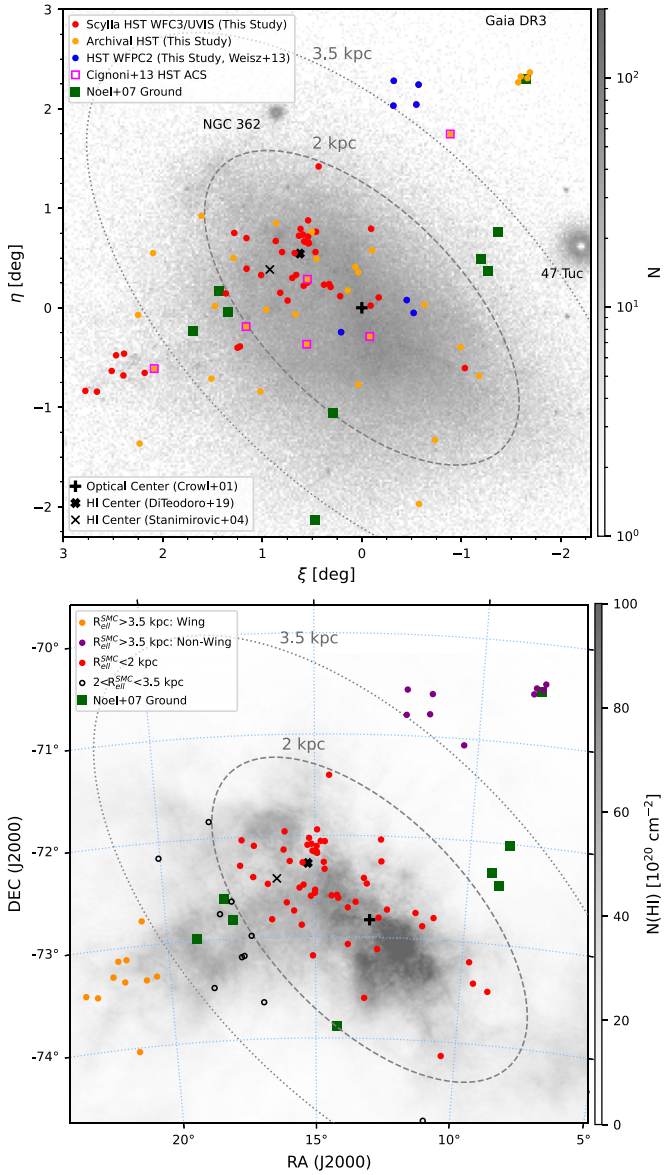

Figure 1. Top: map of the fields analyzed here, overplotted on a stellar density map from Gaia DR3 (see text for details). Our fields are shown as filled circles, color coded by the source of the imaging, including new WFC3/UVIS imaging from Scylla (red), archival ACS/WFC and WFC3/UVIS imaging (orange), and archival WFPC2 LGSPA photometry from J. A. Holtzman et al. (2006) (blue; also analyzed by D. R. Weisz et al. 2013). The subset of archival ACS/WFC fields also analyzed by M. Cignoni et al. (2013) are marked by magenta squares, and ground-based fields from N. E. D. Noël et al. (2007) are shown as green squares. Black symbols indicate different locations of the SMC center, including the optical center we adopt (H. H. Crowl et al. 2001; S. Subramanian & A. Subramaniam 2012) and the H I centers from E. M. Di Teodoro et al. (2019) and S. Stanimirović et al. (2004). Bottom: our fields are overplotted on the GASKAP H I column density map (N. M. Pingel et al. 2022), now color coded by location within the SMC, including the main body (red), wing (orange), and outer nonwing fields (purple; see text for details). Open circles indicate fields not falling into any of these three subsets, with 2 kpc $< R_{\rm ell}^{\rm SMC} <$ 3.5 kpc.

the central region and the wing to the southeast (e.g., A. M. Jacyszyn-Dobrzeniecka et al. 2016; V. Ripepi et al. 2017; D. El Youssoufi et al. 2019), tracing the irregular structure of neutral hydrogen (N. M. Pingel et al. 2022) shown in the bottom panel of Figure 1. Given this age-dependent spatial distribution, we group our fields into subsets based on location in the SMC, overplotted on the H I column density map in the bottom panel of Figure 1, including those located in the main body (red), wing (orange), and, for comparison to fields in the wing, the nonwing fields located at similarly large distances from the SMC center (purple), with projected distances $R_{\rm ell}^{\rm SMC} > 3.5$ kpc.

2.1.1. Scylla Imaging

The new imaging we analyze was obtained as part of the Scylla multicycle pure-parallel program (GO-15891, GO-16235, GO-16786; PI: C. E. Murray). This program accompanied the HST Ultraviolet Legacy Library of Young Stars as Essential Standards (ULLYSES; J. Roman-Duval et al. 2020) spectroscopic campaign, a Directors' Discretionary Time program designed to perform ultraviolet spectroscopy of massive O and B stars toward the Magellanic Clouds. During the ULLYSES spectroscopic primary observations, Scylla obtained parallel imaging with Wide Field Camera 3 (WFC3; R. A. Kimble et al. 2008) in as many as seven broadband filters ranging from the ultraviolet (F225W) to the near-infrared (F160W). However, in the majority of cases, the dithering and exposure time requirements of the ULLYSES primary observations only allowed parallel exposures in a subset of filters. Therefore, the WFC3/UVIS F475W and F814W filters were assigned top priority as a compromise between high throughput and a broad color baseline. As a result, Scylla has obtained two-filter broadband imaging in the WFC3/UVIS F475W and F814W filters across all of the observed fields. An overview of the Scylla pure-parallel imaging program, including science goals and detailed exposure-level information, is provided in C. E. Murray et al. (2024). Basic observational information for the fields we use is given in Table 1.

2.1.2. Archival Imaging

To improve our spatial coverage of the SMC, we searched the HST archive for additional archival imaging of sufficient depth ($\gtrsim$1 mag faintward of the ancient MSTO) in at least two broadband optical filters, listed in Table 1. We rejected fields contaminated by known clusters (see Section 3 and Appendix A), including the Galactic globular clusters 47 Tuc and NGC 362 (and their tidal tails; J. A. Carballo-Bello 2019), as well as fields with severe internal differential extinction hampering SFH fits. Specifically, we rejected fields with $\sigma_1 + \sigma_2 > 0.45$ from D. M. Skowron et al. (2021), where σ_1 and σ_2 represent Gaussian half-widths of the red clump distribution along the reddening vector (see the discussion in Cohen et al. 2024). After applying these cuts (which were also applied to the aforementioned Scylla fields, causing the rejection of only one field, SMC_50), we retained 33 archival fields, listed in Table 1 with their field numbers preceded by the letter A. In addition, we also reanalyze photometry from seven deep Wide Field Planetary Camera 2 (WFPC2) fields provided in the Local Group Stellar Photometry Archive (LGSPA; J. A. Holtzman et al. 2006), all of which were imaged in the F555W and F814W filters, listed in Table 1 with field numbers beginning with the letter W.

In total, our sample of 83 HST pointings consists of 45 fields observed with WFC3/UVIS (43 Scylla fields and two archival fields observed in WFC3/UVIS F606W and F814W filters), with an undithered field of view of 162″ per side (R. A. Kimble et al. 2008); 31 archival Advanced Camera for Surveys (ACS)/

Table 1
Observed Fields

Field	Archive Name/PID	R.A. (J2000) (deg)	Decl. (J2000) (deg)	Blue Filter	C80 (blue) (mag)	C80 (F814W) (mag)	*N* (obs)	*N* (used)
SMC_1	15891_SMC-3192ne-8290	14.946985	−72.104922	WFC3/UVIS F475W	27.12	24.92	23,661	17,559
SMC_2	15891_SMC-2750ne-8567	15.514903	−72.514790	WFC3/UVIS F475W	27.66	25.37	21,629	15,800
SMC_7	15891_SMC-5278ne-9802	14.551469	−71.403310	WFC3/UVIS F475W	27.77	25.40	7229	5761
SMC_8	15891_SMC-3955ne-9818	16.011691	−72.137054	WFC3/UVIS F475W	27.01	24.84	15,527	11,867
SMC_9	15891_SMC-3587ne-10112	15.186138	−72.025194	WFC3/UVIS F475W	27.27	25.06	19,954	15,152
SMC_10	15891_SMC-3149ne-12269	15.080012	−72.151312	WFC3/UVIS F475W	26.48	24.34	8355	5960
SMC_11	15891_SMC-8743se-11371	21.442971	−73.124046	WFC3/UVIS F475W	27.51	25.24	2322	1759
SMC_13	15891_SMC-2983ne-12972	14.931875	−72.174660	WFC3/UVIS F475W	26.43	24.32	8563	5949
SMC_14	15891_SMC-3669ne-13972	14.930241	−71.942178	WFC3/UVIS F475W	27.41	25.15	17,598	13,940
SMC_15	15891_SMC-4292sw-13841	9.5604038	−73.403032	WFC3/UVIS F475W	26.80	24.66	18,525	13,894
SMC_16	15891_SMC-3435ne-13258	15.241572	−72.093556	WFC3/UVIS F475W	26.82	24.81	16,438	13,197
SMC_17	15891_SMC-1588ne-12105	14.458894	−72.592704	WFC3/UVIS F475W	26.74	24.63	31,824	22,077
SMC_18	15891_SMC-3029ne-13288	15.942742	−72.658791	WFC3/UVIS F475W	26.60	24.50	16,688	12,500
SMC_19	15891_SMC-3032ne-13306	14.944591	−72.160401	WFC3/UVIS F475W	26.98	24.80	24,343	17,780
SMC_20	15891_SMC-3370ne-13459	15.113533	−72.083431	WFC3/UVIS F475W	26.81	25.00	15,413	12,678
SMC_21	15891_SMC-3104ne-13781	15.027090	−72.159001	WFC3/UVIS F475W	26.48	24.40	12,900	9334
SMC_22	15891_SMC-9034se-13316	21.724082	−73.129718	WFC3/UVIS F475W	27.75	25.39	2197	1717
SMC_23	15891_SMC-2584ne-14274	14.717750	−72.262425	WFC3/UVIS F475W	26.33	24.23	21,414	15,213
SMC_25	16235_SMC-879ne-11082	13.921283	−72.710449	WFC3/UVIS F475W	26.50	24.44	30,370	19,583
SMC_27	16235_SMC-2668ne-11415	15.381839	−72.485760	WFC3/UVIS F475W	26.55	24.65	21,913	15,319
SMC_28	16235_SMC-10336se-14099	22.971270	−73.435217	WFC3/UVIS F475W	27.00	24.88	1072	713
SMC_29	16235_SMC-3870ne-14647	16.551180	−72.471367	WFC3/UVIS F475W	27.32	25.09	16,339	11,870
SMC_30	16235_SMC-2259ne-15609	15.141961	−72.597028	WFC3/UVIS F475W	26.63	24.50	23,868	16,060
SMC_33	16235_SMC-2167ne-18821	15.010723	−72.568012	WFC3/UVIS F475W	26.20	24.06	21,132	12,376
SMC_34	16235_SMC-2728ne-28918	15.705088	−72.739956	WFC3/UVIS F475W	26.57	24.53	20,946	13,972
SMC_35	16235_SMC-2773nw-32334	12.884764	−72.034680	WFC3/UVIS F475W	27.66	25.32	14,696	11,099
SMC_36	16235_SMC-3127ne-32138	15.405336	−72.265979	WFC3/UVIS F475W	26.58	24.54	19,671	13,507
SMC_37	16235_SMC-3154ne-32442	14.684047	−72.058285	WFC3/UVIS F475W	26.85	24.69	19,023	13,440
SMC_38	16235_SMC-8151se-32530	20.821645	−73.342871	WFC3/UVIS F475W	26.79	24.64	2270	1512
SMC_40	16235_SMC-1339ne-33009	14.239291	−72.616411	WFC3/UVIS F475W	26.53	24.35	21,651	13,676
SMC_41	16235_SMC-286sw-34349	12.890781	−72.806140	WFC3/UVIS F475W	26.21	24.27	39,745	23,347
SMC_42	16235_SMC-1443ne-34945	14.283263	−72.587845	WFC3/UVIS F475W	26.61	24.47	27,018	16,972
SMC_43	16235_SMC-4996ne-34726	17.769602	−72.631797	WFC3/UVIS F475W	26.49	24.38	10,184	6571
SMC_44	16786_SMC-4646se-5833	17.422733	−73.173429	WFC3/UVIS F475W	26.84	24.71	10,071	6938
SMC_45	15891_SMC-641nw-12753	12.617762	−72.723821	WFC3/UVIS F475W	26.51	24.58	40,480	24,937
SMC_46	16235_SMC-4450ne-32733	17.022081	−72.399457	WFC3/UVIS F475W	27.15	24.88	13,578	9611
SMC_47	16786_SMC-9277se-14900	21.952307	−73.279210	WFC3/UVIS F475W	27.72	25.36	2000	1490
SMC_48	16786_SMC-8904se-15007	21.570770	−73.340365	WFC3/UVIS F475W	27.13	24.95	2173	1614
SMC_49	16786_SMC-4926ne-15573	16.962114	−72.091641	WFC3/UVIS F475W	27.44	25.19	12,510	9426
SMC_52	16786_SMC-9946se-16175	22.573365	−73.462673	WFC3/UVIS F475W	27.89	25.52	1956	1407
SMC_53	16786_SMC-4745se-7610	17.512373	−73.184838	WFC3/UVIS F475W	26.85	24.75	9589	6739
SMC_54	16786_SMC-3529ne-15172	15.819982	−72.251044	WFC3/UVIS F475W	27.38	25.09	19,942	14,463
SMC_55	16786_SMC-5409ne-15524	17.349532	−72.032015	WFC3/UVIS F475W	27.55	25.27	9651	7248
SMC_A1	10248	12.852292	−72.249989	ACS/WFC F555W	25.35	23.97	27,790	14,246
SMC_A2	10248	14.690785	−72.330909	ACS/WFC F555W	24.45	23.29	33,320	13,881
SMC_A3	10248	15.456643	−72.881284	ACS/WFC F555W	24.74	23.53	33,871	14,614
SMC_A4	10396	12.905319	−73.115748	ACS/WFC F555W	23.62	22.49	60,252	19,033
SMC_A5	10396	17.152412	−72.977772	ACS/WFC F555W	25.84	24.31	25,255	14,914
SMC_A6	10396	15.002221	−72.536831	ACS/WFC F555W	25.21	23.88	28,627	14,654
SMC_A7	10396	15.087749	−73.184928	ACS/WFC F555W	24.93	23.79	42,149	20,397
SMC_A8	10396	10.440540	−71.064289	ACS/WFC F555W	26.67	25.00	3791	2624
SMC_A9	10396	20.458067	−73.315727	ACS/WFC F555W	26.69	25.02	5477	3963
SMC_A10	10766	13.405039	−72.417642	ACS/WFC F606W	24.24	23.29	47,559	17,299
SMC_A11	10766	13.308628	−72.472014	ACS/WFC F606W	24.34	23.32	50,649	18,751
SMC_A12	12581	18.175243	−72.749376	ACS/WFC F475W	26.73	24.84	17,648	12,367
SMC_A13	13476	11.056933	−72.785819	ACS/WFC F606W	24.88	23.73	39,584	17,927
SMC_A14	13476	13.308959	−73.601034	ACS/WFC F606W	24.66	23.54	41,789	17,704
SMC_A15	13476	14.818366	−72.055697	ACS/WFC F606W	25.12	24.06	28,813	15,101
SMC_A16	13476	16.444570	−72.821259	ACS/WFC F606W	25.09	23.96	31,695	16,068
SMC_A17	13476	9.7530223	−73.195754	ACS/WFC F606W	25.14	24.00	33,400	16,773

Table 1
(Continued)

Field	Archive Name/PID	R.A. (J2000) (deg)	Decl. (J2000) (deg)	Blue Filter	C80 (blue) (mag)	C80 (F814W) (mag)	*N* (obs)	*N* (used)
SMC_A18	13476	15.968124	−71.957872	ACS/WFC F606W	25.48	24.40	24,543	14,410
SMC_A19	13476	16.808531	−73.637940	ACS/WFC F606W	25.86	24.70	17,670	11,413
SMC_A20	13476	9.0387893	−73.470949	ACS/WFC F606W	25.52	24.44	25,650	15,243
SMC_A21	13476	17.432008	−72.282757	ACS/WFC F606W	25.79	24.61	19,931	12,667
SMC_A22	13476	10.495970	−74.139501	ACS/WFC F606W	25.84	24.66	20,911	13,169
SMC_A23	13476	18.510265	−73.473449	ACS/WFC F606W	26.12	24.94	10,831	7500
SMC_A24	13476	18.364156	−71.835039	ACS/WFC F606W	26.14	24.92	9402	6478
SMC_A25	13476	10.998826	−74.789124	ACS/WFC F606W	26.27	25.05	8107	5769
SMC_A26	13476	13.665924	−72.653847	ACS/WFC F606W	23.98	22.97	46,906	15,980
SMC_A27	13476	20.051261	−72.158678	ACS/WFC F606W	26.37	25.12	5881	4130
SMC_A28	13476	20.793737	−72.758007	ACS/WFC F606W	26.30	25.08	5251	3729
SMC_A29	13476	21.331453	−74.040008	ACS/WFC F606W	26.39	25.11	3298	2332
SMC_A30	13673	8.4159276	−70.441980	ACS/WFC F606W	27.34	25.93	2542	1710
SMC_A31	13673	8.4780615	−70.502721	ACS/WFC F606W	27.34	25.95	2744	1820
SMC_A32	13673	8.2115501	−70.453423	WFC3/UVIS F606W	27.30	25.91	1256	897
SMC_A33	13673	8.1553090	−70.393972	WFC3/UVIS F606W	27.33	25.92	1174	842
SMC_W1	smc_u2o903	13.904166	−73.072219	WFPC2 F555W	24.63	23.73	18,262	9585
SMC_W2	smc_u37704	11.475	−70.578613	WFPC2 F555W	26.14	24.21	1075	540
SMC_W3	smc_u377a4	11.524999	−70.778892	WFPC2 F555W	26.08	24.18	1204	618
SMC_W4	smc_u377a6	12.225	−70.545555	WFPC2 F555W	26.15	24.24	1078	521
SMC_W5	smc_u37706	12.225	−70.795280	WFPC2 F555W	26.12	24.21	1327	679
SMC_W6	smc_u46c01	11.666666	−72.745277	WFPC2 F555W	24.96	24.01	7380	4210
SMC_W7	smc_u65c06	11.420833	−72.872222	WFPC2 F555W	24.46	23.19	12,244	7061

Note. Column: (1) field name adopted here. Column (2): field name corresponding to data products available in the MAST archive. For the LGSPA WFPC2 fields we give the corresponding field name on the LGSPA website, and for the remainder of the archival imaging we simply give the program ID. Columns (3)–(4): J2000 coordinates of the center of each field. Column (5): the bluer of the two filters used in our photometry. In all cases, the redder of the two filters was the F814W filter of the same instrument. Columns (6)–(7): the 80% completeness limit in each filter, used as the faint limit of the stellar sample included in SFH fitting. Column (8): the total number of stars in each field passing our photometric quality cuts. Column (9): the number of stars used for SFH fitting, brightward of the 80% completeness limit in both filters.

WFC fields, with an undithered field of view of 200″ per side (H. C. Ford et al. 1998); and the seven WFPC2 LGSPA fields, each covering an area slightly (21%) smaller than WFC3/UVIS (J. T. Trauger et al. 1994). Therefore, our resulting spatial resolution is, in a literal sense, better than any of the ground-based studies of the SMC using contiguous imaging, but this comes at the cost of nonuniform spatial coverage. For example, each of our pointings covers an area substantially smaller than either the Voronoi bins used to analyze SMASH data toward the SMC (P. Massana et al. 2022) or the VMC tile subregions analyzed by S. Rubele et al. (2015, 2018). Our field sizes are, however, fairly well matched to the extinction maps of D. M. Skowron et al. (2021), built from contiguous, wide-field imaging of both the LMC and SMC using a self-consistent analysis technique, providing spatial resolution from 1.′7 to 6.′9 over the area sampled by our observations.

2.2. Photometry

The details of performing point-spread function (PSF) fitting photometry on individual science images in each field to generate clean photometric catalogs are discussed in C. E. Murray et al. (2024). We use the `Dolphot` software package to perform additional image preprocessing and PSF photometry identically to the techniques described in B. F. Williams et al. (2014, 2021). Therefore, we briefly summarize our photometry procedure here for convenience, noting that some previous HST studies of the SMC used earlier versions of `Dolphot` to perform PSF photometry (A. E. Dolphin et al. 2001; D. R. Weisz et al. 2013), while some used other PSF photometry programs (e.g., M. P. McCumber et al. 2005; E. Sabbi et al. 2009; M. Cignoni et al. 2012, 2013).

For each target field, individual `flc` images (corrected for charge transfer inefficiency) were combined into a deep, distortion-corrected master reference image in each filter using the `astrodrizzle` task within `drizzlepac` (R. J. Avila et al. 2015). Next, for each image, `Dolphot` masks bad pixels, applies a pixel area map, splits the image into individual chips, and calculates the sky background. `Dolphot` includes modules specific to each imager on board HST, including customized spatially varying PSFs for each filter. There are many parameters used by `Dolphot` to govern the details of the PSF photometry procedure, and we adopt the per-instrument parameters thoroughly tested and recommended by B. F. Williams et al. (2014, 2021). The resulting photometric catalogs are calibrated to the Vegamag photometric system and contain several diagnostic parameters that can be used to reject poorly measured, spurious, and nonstellar sources. These parameters are described generally in the `Dolphot` manual,[15] as well as in the context of the present application in Cohen et al. (2024), and we make cuts on the per-filter values of crowding parameter `crowd`, the absolute value of the sharpness `sharp`, and the photometric quality flag to retain only well-measured stellar sources. Given the difference in spatial resolution across

[15] http://americano.dolphinsim.com/dolphot/

Table 2
Photometric Quality Cuts

Camera	crowd	|sharp|	Flag
WFC3/UVIS	$\leqslant$0.25	$\leqslant$0.25	0, 2
ACS/WFC	$\leqslant$0.1	$\leqslant$0.1	0, 2
WFPC2	$\leqslant$0.25	$\leqslant$0.25	N/A

Note. The crowd and sharp cuts are applied to per-filter values, with stars required to pass these cuts in both filters. Values of 0 or 2 for the photometric quality flag given in the last column reject sources with too many bad and/or saturated pixels for reliable flux measurements.

the different cameras used, the values used for our photometric quality cuts are chosen on a per-camera basis, listed in Table 2. In the case of the WFPC2 fields, we note that while high-level merged photometry catalogs are available, we opted to perform cuts on the per-filter quality diagnostics provided in the raw catalogs[16] identically to the remainder of our imaging to keep our analysis as self-consistent as possible.

Color–magnitude diagrams (CMDs) are shown in Figure 2 for the various filter combinations present across our imaging. We have overlaid solar-scaled PARSEC isochrones (A. Bressan et al. 2012) for a representative range of masses and ages, demonstrating that our imaging typically reaches down to a mass of $\sim$0.5 $M_{\odot}$ on the unevolved main sequence, as deep as or deeper than previous studies of the SFH in the SMC (e.g., J. Harris & D. Zaritsky 2004; N. E. D. Noël et al. 2009; M. Cignoni et al. 2012; D. R. Weisz et al. 2013; S. Rubele et al. 2018; P. Massana et al. 2022). Our SFH fitting procedure (Section 3) requires a model of observational noise and incompleteness in each field, so we perform artificial star tests by inserting $>10^5$ artificial stars per field and attempt to recover them identically to our observations. The artificial stars are assigned a flat input spatial distribution, and the Bayesian Extinction and Stellar Tool (K. D. Gordon et al. 2016) was used to assign input magnitudes drawn from a library built with PARSEC models over a broad range of input ages ($6.0 \leqslant \log \mathrm{age/yr} \leqslant 10.13$), metallicities ($-2.1 \leqslant \mathrm{[M/H]} \leqslant -0.3$), distances ($47 \leqslant (d_{\odot}/\mathrm{kpc}) \leqslant 77$), and extinctions ($0 \leqslant A_V \leqslant 1$). The per-field photometric completeness as a function of magnitude is shown in Figure 3 for all of the filter combinations across our sample, with the bluer filter shown in purple and the redder filter shown in orange in each panel, demonstrating that completeness generally drops off fairly quickly as a function of magnitude close to our detection limit. Therefore, we adopt the 80% completeness limit, denoted C80, as the faint magnitude limit of the stellar sample used for SFH fitting, as in our companion study of the spatially resolved SFH in the LMC. The rightmost column of Figure 3 illustrates the magnitude difference between C80 and the ancient MSTO magnitude, calculated assuming a 13 Gyr metal-poor ($\mathrm{[M/H]} = -1.2$) PARSEC isochrone (based on our best-fit age–metallicity relations (AMRs); see Section 4.3) and per-field extinction values from the D. M. Skowron et al. (2021) map, demonstrating that the vast majority of our fields (>90%), including *all* of our Scylla imaging (shown in blue in the right column of Figure 3), are 80% complete to at least 1 mag faintward of the ancient MSTO in both filters that we use for SFH fitting.

[16] http://astronomy.nmsu.edu/holtz/archival/html/lg.html

3. Star Formation History Fitting

Before performing SFH fits to each field, we make two modifications to our photometric catalogs. First, in cases of spatial overlap between fields, we retained the overlapping region in whichever of the two fields had deeper photometry (i.e., fainter values of C80), excising it from the shallower of the two fields. This treatment ensures that each field can be treated as a statistically independent sample, without any sources contributing to SFH fits for multiple fields. Second, we remove known star clusters (E. Bica et al. 2020) that could bias our characterization of the SMC field population. For each cluster we conservatively remove from our catalogs all sources lying within the cluster semimajor-axis length from the cluster center listed by E. Bica et al. (2020), which were generally estimated visually by the authors of the original source catalog, and the excised clusters and the affected fields are listed in Appendix A. The impact on our overall sample is quite small: across all of the affected fields, the excised fraction of the field of view has a median of only 10%, and our total sampled area in the SMC is reduced by only 5%.

We use the software code MATCH (A. E. Dolphin 2002) to calculate the best-fitting SFH and AMR from the CMD of each field using the well-known CMD synthesis technique (see E. Tolstoy et al. 2009 for a review). MATCH has been used to measure the SFHs of scores of galaxies throughout the Local Volume over their entire lifetimes (e.g., B. F. Williams et al. 2009, 2011, 2017; D. R. Weisz et al. 2011, 2014; D. J. Radburn-Smith et al. 2012; M. Geha et al. 2015; K. B. W. McQuinn et al. 2018, 2023; A. Savino et al. 2023) and produces results comparable to other CMD synthesis codes (M. Monelli et al. 2010a, 2010b; S. L. Hidalgo et al. 2011; E. D. Skillman et al. 2014, 2017).

To calculate the best-fitting SFH and AMR and uncertainties, MATCH compares an observed photometric catalog against synthetic photometry of a linear combination of simple stellar populations (SSPs) from a chosen stellar evolutionary library. To test the sensitivity of our results to the assumed evolutionary library, we perform three fits for each field, using the PARSEC (A. Bressan et al. 2012), MIST (A. Dotter 2016; J. Choi et al. 2016), and updated BaSTI (S. L. Hidalgo et al. 2018, which we denote "BaSTI18") stellar evolutionary libraries. All of these stellar evolutionary libraries provide synthetic photometry in the native filter systems of each of the HST cameras included in our sample (ACS/WFC, WFC3/UVIS, WFPC2), rendering field-to-field photometric calibration unnecessary.

To compare observed and synthetic CMDs, the artificial star tests are used to apply observational noise to the synthetic SSPs, and MATCH varies the star formation rate and mean metallicity in each user-selected time bin, seeking the best-fit SFH and AMR using a Poisson likelihood statistic. For SFH fitting, we use the same basic input assumptions as in Cohen et al. (2024), providing a consistent methodology across our analyses of spatially resolved SFHs in both the LMC and SMC. Specifically, we use time bins of width $\Delta \log \mathrm{age/yr} = 0.05$ dex from $\log \mathrm{age/yr} = 7.2$ (the youngest age available across all three sets of evolutionary models we employ) to $\log \mathrm{age/yr} = 10.15$, a metallicity spread in each time bin of $\Delta\mathrm{[M/H]} = 0.15$ dex over an allowed metallicity range of $-2.0 \leqslant \mathrm{[M/H]} \leqslant +0.2$, a P. Kroupa (2001) initial mass function, and an assumed binary fraction of 0.35 with a flat mass ratio distribution as a function of primary mass. While various SFH studies of dwarf galaxies assume binary fractions

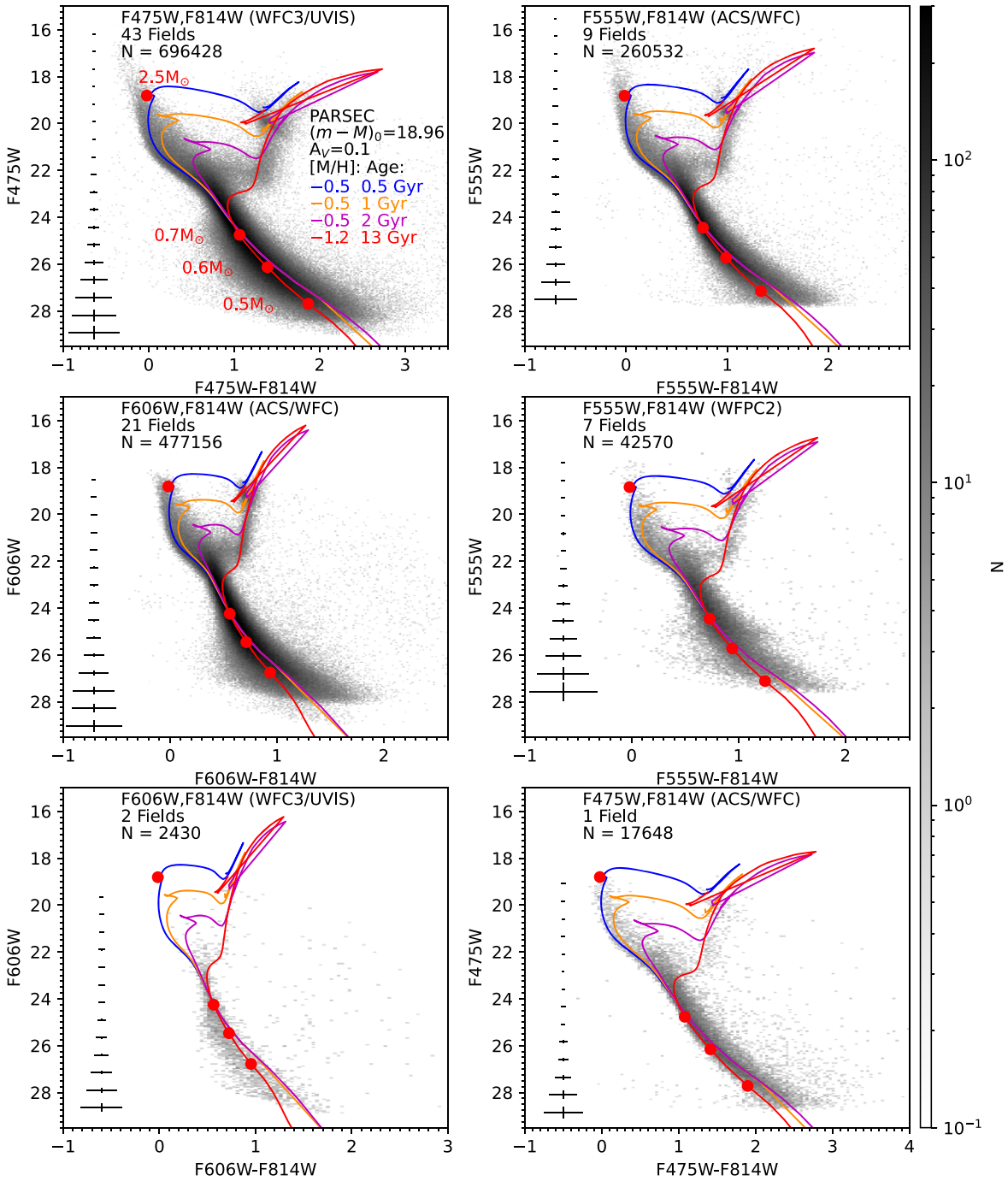

Figure 2. Stacked Hess diagrams for the various filter combinations present in our imaging. The total number of fields we analyze in a particular filter combination is given in the top left of each panel, along with the total number of stars passing our photometric quality cuts. Median photometric errors are shown along the left side of each CMD. PARSEC isochrones are overplotted to illustrate the range of stellar ages accessible in our photometry in different evolutionary phases, with representative stellar masses indicated along the main sequence. Due to observational restrictions imposed by the ULLYSES primary imaging, the brightest SMC sources (corresponding to main-sequence stellar masses $\gtrsim 2.5 M_{\odot}$) are saturated in many cases.

ranging from 0.3 to 0.5 (e.g., M. Monelli et al. 2010a, 2010b; E. Sacchi et al. 2018; P. Massana et al. 2022), a binary fraction of 0.35 was originally implemented for SFH fitting with MATCH based on multiplicity statistics for solar neighborhood dwarfs (A. Duquennoy & M. Mayor 1991). We retain this value for consistency with the aforementioned vast database of lifetime SFHs derived for Local Volume dwarfs using MATCH (e.g., B. F. Williams et al. 2011; D. R. Weisz et al. 2011, 2014), including our companion study of the LMC (Cohen et al. 2024). In any case, the shape of the SFH is quite insensitive to variations in the assumed binary fraction (or initial mass function slope) given deep imaging extending faintward of the ancient MSTO (M. Monelli et al. 2010a; S. L. Hidalgo et al. 2011; M. Cignoni et al. 2012; A. A. Cole et al. 2014), as we have in hand for our SMC fields. The uncertainties on the resultant SFHs include both random (statistical) and systematic contributions, detailed in A. E. Dolphin (2013) and A. E. Dolphin (2012), respectively.

When searching for the best-fit SFH, MATCH also has the capability to float distance modulus $(m - M)_0$, foreground

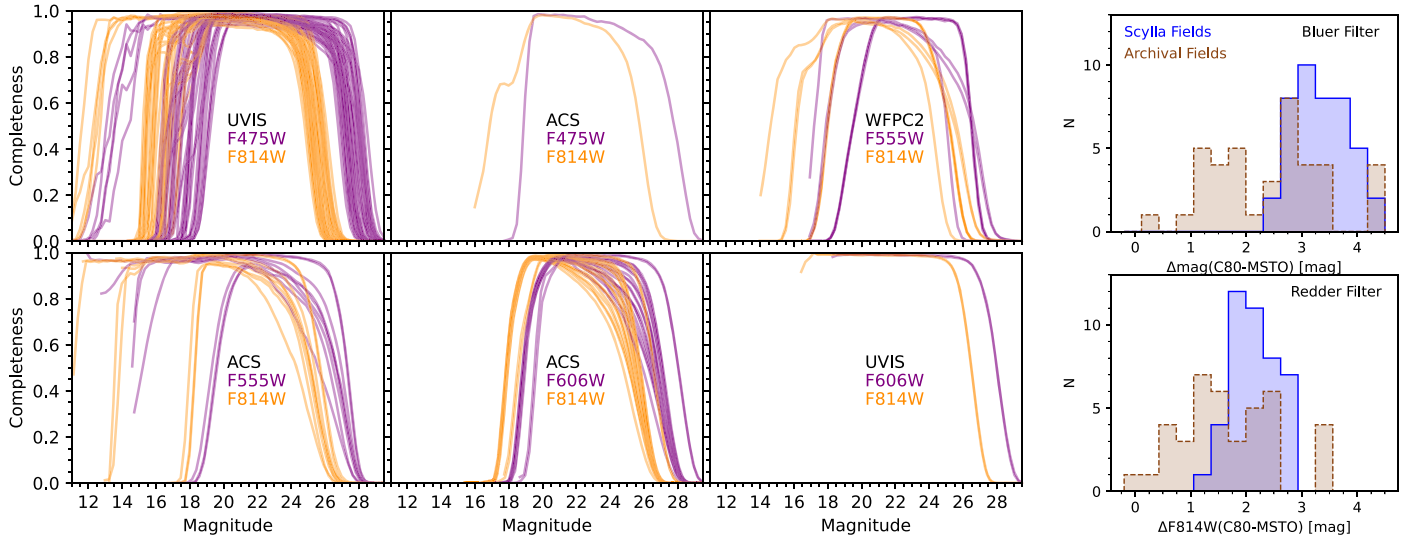

Figure 3. Left columns: completeness vs. magnitude for each individual field, with separate panels for each filter combination present in our imaging sample. In each panel, completeness as a function of magnitude (in the Vegamag photometric system) is shown in purple for the bluer of the two filters and orange for the redder of the two filters. Rightmost column: magnitude difference between the 80% completeness limit, used as the faint limit for SFH fitting, and the MSTO magnitude in each field, assessed using a 13 Gyr PARSEC isochrone with [M/H] = −1.2, $(m-M)_{0,\mathrm{SMC}} = 18.96$, and extinction from D. M. Skowron et al. (2021). The top right and bottom right panels correspond to the bluer and redder filter available in each field, respectively, illustrating that the vast majority (>90%) of our fields (and all of the Scylla fields) are 80% complete to at least 1 mag below the ancient MSTO in both filters.

Galactic extinction $A_{V,\mathrm{fg}}$, and additional internal differential extinction δA_V as free parameters. We allow MATCH to search over a grid with a grid spacing of 0.05 mag in all three of these parameters. A similar grid search technique has been implemented using MATCH in the past, but searching over two parameters ($A_{V,\mathrm{fg}}$ and δA_V) rather than three, using an identical grid spacing (A. R. Lewis et al. 2015; M. Lazzarini et al. 2022). Our strategy is a direct extension of this approach, simply adding $(m-M)_0$ as a third parameter in the grid search, and has been applied identically to the LMC (Cohen et al. 2024). In our companion study of the LMC, we exploited the wealth of independent line-of-sight distance and extinction measurements (e.g., Y. Choi et al. 2018a; D. M. Skowron et al. 2021) to assess the ability of MATCH to recover the three parameters using our grid search strategy, finding that it performed quite well, recovering per-field distances with a median precision of $\lesssim$3% (see Figure 5 of Cohen et al. 2024). The LMC is an optimal test bed for such a comparison, since the three-dimensional distribution of its red clump stars is well fit by a disk with a thickness of only ∼1 kpc (Y. Choi et al. 2018a, 2018b). For the SMC, the situation is more complicated, since MATCH assumes a single fixed distance for SFH fitting while the SMC is known to have a line-of-sight depth that is both significant and position dependent (D. L. Nidever et al. 2013; A. M. Jacyszyn-Dobrzeniecka et al. 2017; S. Subramanian et al. 2017; T. Muraveva et al. 2018; B. L. Tatton et al. 2021; D. El Youssoufi et al. 2021; P. Yanchulova Merica-Jones et al. 2021). Therefore, we performed a set of simulations in which we used SMC-like SFHs to generate input synthetic stellar populations, and then we assigned them various line-of-sight distance distributions based on extant analyses of the SMC before attempting to recover their SFHs with MATCH identically to our observations. Further details are given in Appendix B, where we demonstrate that our results are unaffected by line-of-sight depth effects to within their uncertainties.

Examples of our per-field SFH fitting results are shown in Figure 4, where each row presents SFH fits for a single field. We have intentionally chosen two fields spanning the range of fit quality seen across our sample to illustrate the precision of our best-fit SFHs and AMRs on a per-field basis. The top row is an example of a field with a high-quality SFH fit, where the SFH fitting residuals (third panel from left) show little to no structure across the CMD. The results shown in the bottom row correspond to a field with more apparent structure in the CMD fit residuals. Discrepancies are seen at the faint blue corner of the stellar sample, as well as in the vicinity of the red clump and horizontal branch, and likely result from a combination of small-scale differential reddening, line-of-sight distance spread, and the known difficulty of evolutionary models to reproduce in detail the CMD morphology corresponding to late stages of stellar evolution (see C. Gallart et al. 2005 for a review). In the middle panel of Figure 4, we show the best-fit AMR, which increases monotonically with age to within uncertainties. This is an important validation of our SFH fitting procedure given that we placed no restriction on the allowed metallicity in each time bin. The right panel in each row illustrates the cumulative SFH (CSFH) output by MATCH, which is the fraction of total stellar mass ever formed that had formed by a given look-back time. We use the CSFH to quantify our per-field SFH fitting results, where τ_{50}, τ_{75}, and τ_{90} correspond to the look-back times by which 50%, 75%, and 90% of the cumulative mass had formed, respectively. The values of τ_{50}, τ_{75}, and τ_{90} and their 1σ uncertainties are calculated via interpolation in the CSFH and its 1σ uncertainties, illustrated for the two example cases in the right panels of Figure 4. All of the individual per-field values of τ_{50}, τ_{75}, and τ_{90} and their uncertainties for each of the three stellar evolutionary models we assume are provided in Table 5 in Appendix C.

4. Results

Studies of the spatial variation in the SFH of the SMC have already revealed several trends that have ramifications for the interaction history of the SMC–LMC–Milky Way system. Star formation in the SMC has generally been centrally concentrated, resulting in an outside-in age gradient such that the inner

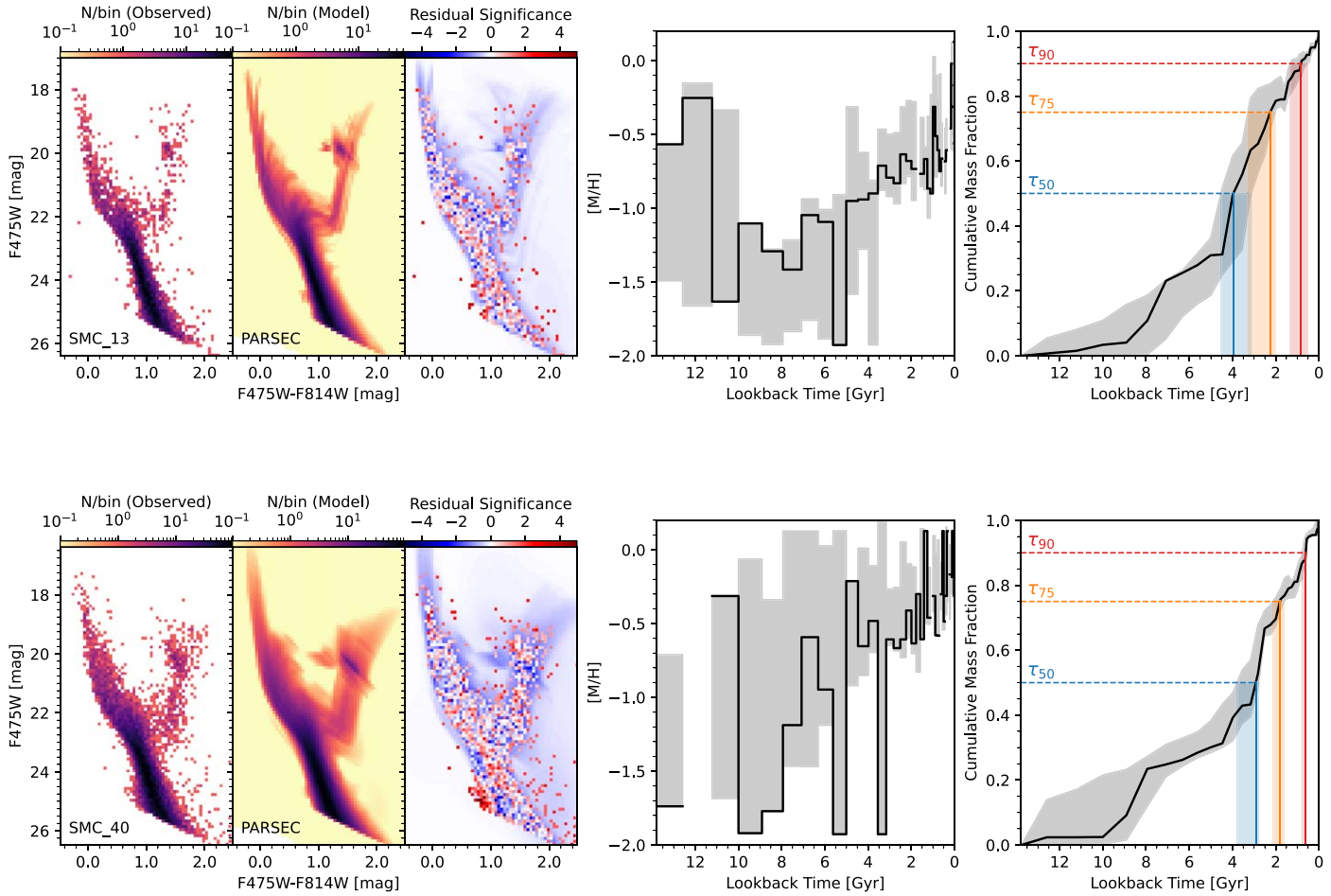

Figure 4. Example SFH fits for two fields (top row: SMC_13; bottom row: SMC_40) spanning the range of fit quality seen across our sample to illustrate our typical SFH and AMR precision on a per-field basis. Left: Hess diagrams showing the observed CMD, the best-fit model, and the residuals in the sense (data − model). Middle: best-fit AMR, with uncertainties indicated by gray shading. Despite large per-field uncertainties, both fields are consistent with an AMR that increases monotonically with time. Right: best-fit CSFH, showing the fraction of total mass ever formed as a function of look-back time. We quantify the CSFH using the metrics τ_{50}, τ_{75}, and τ_{90} to indicate the look-back times by which 50%, 75%, and 90% of the cumulative stellar mass had formed, respectively. These values are overplotted on the CSFHs using blue, orange, and red vertical lines, respectively, with shading corresponding to 1σ uncertainties.

SMC is younger on average (R. Carrera et al. 2008; M. Cignoni et al. 2013; S. Rubele et al. 2018), due at least in part to a lack of recent star formation far from the SMC center (A. E. Dolphin et al. 2001). However, in the direction of the SMC wing to the east, this trend does not hold, and star formation has continued over the most recent few gigayears (M. P. McCumber et al. 2005; N. E. D. Noël et al. 2009). To place quantitative constraints on these trends, we first combine SFH results for individual fields into subsets based on location (see the bottom panel of Figure 1), allowing us to compare trends in the wing to those in both nonwing fields at similar distances from the SMC center and the inner SMC (Section 4.1). Subsequently, we use our field-by-field SFHs to examine radial SFH trends in detail, measuring their slopes and assessing their linearity (Section 4.2).

4.1. Global Trends

The CSFHs of the three positionally selected subsets of fields (main body, wing, outer nonwing) are shown in the left panel of Figure 5, color coded as in the bottom panel of Figure 1. These CSFHs were calculated by statistically combining the best-fitting SFHs and their uncertainties for each individual field. Because systematic uncertainties cannot be assumed to be uncorrelated (unlike random uncertainties), the calculation of uncertainties when combining SFH results across multiple fields is nontrivial, and further details can be found in D. R. Weisz et al. (2011, see their Appendix C) and A. E. Dolphin (2012). Rather than simply fitting a single SFH to a combined CMD, statistically combining the best-fit SFHs and uncertainties from individual fields is necessary to account for per-field differences in photometric depth and incompleteness (and different observing setups).

Two features are immediately apparent from the CSFH comparison in the left panel of Figure 5: The first is an outside-in age gradient, such that the outer fields are older on average than the inner SMC (we quantify this gradient as a function of $R_{\rm SMC}^{\rm ell}$ below in Section 4.2). For example, the outer wing and nonwing fields (orange and purple in Figure 5) formed 50% of their cumulative mass by $5.5^{+0.3}_{-0.6}$ and $6.8^{+0.3}_{-0.8}$ Gyr ago, compared to $3.9^{+0.2}_{-0.1}$ Gyr ago for the main body of the SMC (red in Figure 5). Second, in the outer SMC, the wing and nonwing fields had formed similar cumulative mass fractions only until ∼6 Gyr ago. This may be when the LMC and SMC began interacting (e.g., G. Besla et al. 2012), possibly driving continued star formation in the wing (and main body) but not the outer nonwing fields, as observed over the past few gigayears (see below).

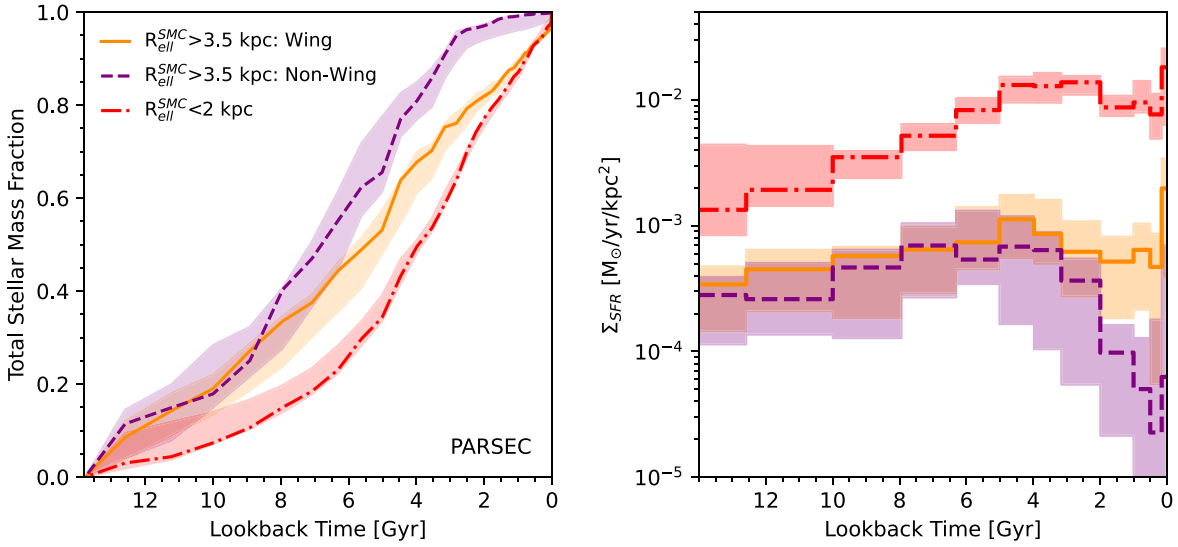

Figure 5. Left: cumulative SFHs of fields in the wing (orange solid line), nonwing fields at similarly large radii of $R^{\rm ell}_{\rm SMC,opt} > 3.5$ kpc (purple dashed line), and fields in the main body with $R^{\rm ell}_{\rm SMC,opt} < 2$ kpc (red dashed–dotted line). The wing and nonwing fields assembled a similar fraction of their total mass at early times (look-back time $\geqslant$6 Gyr), but in the most recent $\sim$2 Gyr, the wing fields assembled a much larger fraction of their mass, similar to fields in the main body. Conversely, the outer nonwing fields formed only $\sim$1% of their mass within the past 1 Gyr. Right: average star formation rate per unit area in several illustrative time intervals. Colors are as in the left panel. Although the wing fields formed a similar mass fraction in the past $\sim$1−2 Gyr to the main body, their star formation rate per projected unit area $\Sigma_{\rm SFR}$ has remained an order of magnitude lower. Meanwhile, the wing and nonwing fields, at similarly large distances from the SMC center, have similar star formation rates until $\sim$2 Gyr ago, when $\Sigma_{\rm SFR}$ in the nonwing outer fields decreased by an order of magnitude until the most recent LMC–SMC collision.

The nature and timing of the divergence in CSFH trends between the wing and outer nonwing fields are illustrated in the right panel of Figure 5, where we plot the average star formation rate per unit area[17] $\Sigma_{\rm SFR}$ in several selected time intervals for the three subsets of fields. For the wing fields, continued star formation resulted in $10.8\%^{+1.5}_{-0.7}$ of their cumulative mass being formed in the past gigayear, calculated directly from interpolation in the CSFH and its uncertainties. This cumulative mass fraction is in excellent agreement with the value of $\sim$7%−12% reported by N. E. D. Noël et al. (2009) for fields near the wing. The outer nonwing fields, on the other hand, are nearly devoid of stars formed within the past several gigayears, reflected by a marked drop-off in star formation beginning $\sim$3−4 Gyr ago (also observed for a nearby field in the northwestern SMC by A. E. Dolphin et al. 2001). In fact, the drop-off in star formation in the outer nonwing fields several gigayears ago was sufficiently dramatic that they formed only $\leqslant$1% of their mass within the past gigayear, forming 90% of their mass by $3.2^{+0.1}_{-0.5}$ Gyr ago. The wing and inner SMC fields, lacking such a drop-off and instead continuing to form stars, did not form 90% of their mass until $0.90^{+0.08}_{-0.13}$ and $0.77^{+0.02}_{-0.07}$ Gyr ago, respectively. However, while the wing fields and the main body formed similar *fractions* of their cumulative mass over the past 1−2 Gyr (left panel of Figure 5), the *values* of $\Sigma_{\rm SFR}$ in the main body are consistently higher (by about an order of magnitude; right panel of Figure 5), in agreement with CMD-based SFH fits by M. Cignoni et al. (2013) and an SFH analysis of long-period variables (S. Rezaei kh et al. 2014). However, the distribution of our fields is particularly concentrated, even within the main body of the SMC; our fields with $R^{\rm SMC}_{\rm ell} < 2$ kpc have a median value of $R^{\rm SMC}_{\rm ell} = 1.0$ kpc, compared to a value of 1.4 kpc that would result from a flat spatial distribution.

We also find evidence for an enhancement in star formation following the most recent LMC–SMC collision $\sim$150 Myr ago (Y. Choi et al. 2022), reported by S. Rubele et al. (2015, 2018). Such a recent enhancement could be at least partially due to star formation from gas that was already tidally stripped (D. El Youssoufi et al. 2023) and may be coeval with the formation of extended high-velocity cold gas outflows (N. M. McClure-Griffiths et al. 2018). Although the saturation limit of our imaging prohibits robust constraints on star formation rates at such recent times (due to the higher luminosities of younger, more massive, and short-lived stellar populations), the best-fit $\Sigma_{\rm SFR}$ values we find in the inner SMC following the most recent LMC–SMC collision are $\Sigma_{\rm SFR} = 0.04^{+0.03}_{-0.01}\,M_\odot\,{\rm yr}^{-1}\,{\rm kpc}^{-2}$ when restricted to the most recent 25 Myr, nearly as high as Hα-based values seen in the SMC's most prominent star-forming region N66 (NGC 346) over the past 5 Myr (S. Hony et al. 2015; see also L. M. Z. Hagen et al. 2017).[18] Our results also allow for the possibility that this most recent star formation enhancement is global in nature, seen also in the outer nonwing fields (see the right panel of Figure 5). While S. Rubele et al. (2018) and P. Massana et al. (2022) find that recent star formation in the SMC is instead centrally concentrated, at least in the former case uncertainties cannot rule out the global nature of an enhancement in $\Sigma_{\rm SFR}$ by a factor of a few. Based on observations of an isolated pair of interacting dwarfs, G. C. Privon et al. (2017) suggested that such a global star formation enhancement could be caused by large-scale interaction-driven ISM compression, in this case triggered by the LMC–SMC collision. While our focus here is on spatial trends in the lifetime assembly history of the SMC, a more detailed analysis of the timing, duration, and location of star

[17] To calculate $\Sigma_{\rm SFR}$, we use the nonoverlapping spatial coverage of each field and assume a fixed SMC distance of 62 kpc.

[18] When averaged over *all* of our fields rather than just the main body of the SMC, we find $\Sigma_{\rm SFR} = 0.007^{+0.004}_{-0.002}\,M_\odot\,{\rm yr}^{-1}\,{\rm kpc}^{-2}$, in reasonable agreement with K. E. Jameson et al. (2016, see their Figure 5) given the centrally concentrated spatial distribution of our fields.

formation bursts in the LMC and SMC will be presented separately (C. Burhenne et al. 2024, in preparation).

The central concentration of star formation seen in the right panel of Figure 5 was noted in previous ground-based surveys (J. Harris & D. Zaritsky 2004; S. Rubele et al. 2018; P. Massana et al. 2022), as well as studies using multiple HST pointings (D. R. Weisz et al. 2013; M. Cignoni et al. 2013). In cases where star formation rates were provided, these values are in good agreement with our results. For example, prior to 5 Gyr ago, before the star formation enhancements attributed to LMC–SMC interaction (J. Harris & D. Zaritsky 2004; S. Rubele et al. 2018; P. Massana et al. 2022), the VMC survey (S. Rubele et al. 2018) gives an average star formation rate $\langle \Sigma_{\rm SFR} \rangle_{t > 5\ {\rm Gyr}} = 1.3^{+0.2}_{-0.1} \times 10^{-3}\, M_\odot\, {\rm yr}^{-1}\, {\rm kpc}^{-2}$ and SMASH (P. Massana et al. 2022) finds $\langle \Sigma_{\rm SFR} \rangle_{t > 5\ {\rm Gyr}} = 0.7^{+0.3}_{-0.3} \times 10^{-3}\, M_\odot\, {\rm yr}^{-1}\, {\rm kpc}^{-2}$. Over the most recent 3 Gyr, VMC results give $\langle \Sigma_{\rm SFR} \rangle_{t < 3\ {\rm Gyr}} = 2.3^{+0.5}_{-0.4} \times 10^{-3}\, M_\odot\, {\rm yr}^{-1}\, {\rm kpc}^{-2}$ and SMASH finds $1.2^{+0.4}_{-0.4} \times 10^{-3}\, M_\odot\, {\rm yr}^{-1}\, {\rm kpc}^{-2}$. All of these values sit comfortably in between the values of $\Sigma_{\rm SFR}$ we find for the main body and the outer regions of the SMC (right panel of Figure 5). Survey-to-survey differences can be attributed at least in part to differences in spatial coverage, especially in light of the apparently strong radial gradient in $\langle \Sigma_{\rm SFR} \rangle$ apparent from the right panel of Figure 5. In particular, SMASH excluded the central region of the the SMC owing to crowding, while VMC provided contiguous spatial coverage that included this central region but with differing coverage of the outer SMC. Predating these studies, MCPS also provided spatially resolved SFH fits (J. Harris & D. Zaritsky 2004), although their best-fit star formation rates were a factor of a few larger than those of VMC, SMASH, or the present work. Furthermore, J. Harris & D. Zaritsky (2004) report an enhancement in star formation prior to 8.4 Gyr ago that is unconfirmed by any of these more recent studies (see Figure 11 of S. Rubele et al. 2018 and Figure 2 of P. Massana et al. 2022). As discussed by S. Rubele et al. (2018, see their Sections 5.2−5.3), such discrepancies with J. Harris & D. Zaritsky (2004) likely result from a combination of several factors, including their use of fixed discrete metallicity values, a different assumed stellar initial mass function, a fixed SMC distance of 60 kpc, and shallower imaging providing less leverage on the oldest stellar populations.

4.2. Quantifying the Outside-in Radial Age Gradient

A comparison of the lifetime SFHs in the inner ($R_{\rm ell}^{\rm SMC} < 2$ kpc) versus outer ($R_{\rm ell}^{\rm SMC} > 3.5$ kpc) SMC in Figure 5 reveals an outside-in present-day age gradient, so we turn to our per-field SFH results to quantify the age gradient and its statistical significance. We plot the CSFH metrics τ_{90}, τ_{75}, and τ_{50} versus semimajor-axis equivalent distance $R_{\rm ell}^{\rm SMC}$ in the top row of Figure 6. The individual fields are color coded by position angle east of north, and the wing fields are indicated with orange diamonds. The tendency for fields at large $R_{\rm ell}^{\rm SMC}$ to show larger uncertainties reflects the smaller number of stars available per field to constrain SFH fits far from the center of the SMC (see Table 1). Overall, the CSFH metrics (i.e., look-back time to form a given cumulative mass fraction) show a linear trend with $R_{\rm ell}^{\rm SMC}$. However, the wing fields deviate from this linear trend, increasingly so at more recent look-back times, with the wing fields assembling similar mass fractions to the inner SMC in the most recent few gigayears (as seen in Figure 5). We therefore exclude the wing fields before performing linear fits to measure the slope of the radial age gradient, as well as the Pearson linear correlation coefficient ρ and the Spearman rank correlation coefficient r_s, with uncertainties calculated using Monte Carlo draws from the asymmetric error distributions of the per-field CSFH metrics. For all three of the CSFH metrics we examine, we find a moderate to high degree of linearity at very high statistical significance, with Pearson linear correlation coefficients $\rho > 0.68$ and p-values $< 10^{-3}$.

In the bottom row of Figure 6, we reframe our results, choosing fixed look-back times of 1, 3, and 6 Gyr (left, middle, and right panels, respectively) and plotting the cumulative mass fraction formed in each field by that look-back time (as a function of $R_{\rm ell}^{\rm SMC}$). These look-back times were chosen to age-date the look-back time when the wing fields last formed a similar mass fraction to the rest of the outer SMC (i.e., the outer nonwing fields), ∼6 Gyr ago. More recently, the bottom left panel of Figure 6 illustrates on a per-field basis that *all* of the outer nonwing fields ($0° < {\rm PA} < 90°$, $R_{\rm ell}^{\rm SMC} > 3.5$ kpc) formed $\lesssim$1% of their mass within the most recent 1 Gyr, while the bottom right panel of Figure 6 illustrates the earliest look-back time at which our data quality allows the detection of a linear radial age gradient, 6 Gyr ago, for which we find that the relationship between cumulative mass fraction formed and $R_{\rm ell}^{\rm SMC}$ has a Pearson $\rho = 0.58^{+0.08}_{-0.08}$ (p-value $< 10^{-3}$). At even earlier look-back times, observational uncertainties hamper the detection of the linear correlations between look-back time and $R_{\rm ell}^{\rm SMC}$ (p-values $\gtrsim 0.01$).

The fits shown in Figure 6 parameterize distance from the SMC assuming an elliptical geometry frequently used in the literature (e.g., A. E. Piatti et al. 2005; B. Dias et al. 2014; M. C. Parisi et al. 2022), shown using gray ellipses in Figure 1. To test whether our results depend on this parameterization, we have reperformed our fits versus simple geometric on-sky distance rather than elliptical (semimajor-axis equivalent) distance from the SMC center. Because old stellar populations in the SMC show a nearly spherical geometry (J. Harris & D. Zaritsky 2004; S. Rubele et al. 2018), some previous literature studies do use projected on-sky distance without any correction for geometric effects (e.g., D. L. Nidever et al. 2011; P. Massana et al. 2020; J. T. Povick et al. 2023). We found that while the slopes (and zero-points) of the best-fit lines necessarily change, the linear correlation coefficients are unaffected to within their uncertainties ($\rho \geqslant 0.61$) and retain their high statistical significance (p-values $< 10^{-3}$). We have also verified that our results are robust to the choice of stellar evolutionary model library used for our SFH fits, and the best-fit parameters for all combinations of evolutionary model and parameterization of radius are listed in Table 3.

Our spatial sampling of the SMC is not unbiased, and the spatial distribution of our fields is highly centrally concentrated, with a median $R_{\rm ell}^{\rm SMC} = 1.4$ (1.2) kpc including (excluding) the wing fields. To test the extent to which our finding of a linear age gradient hangs on the results for our nine outer nonwing fields with $R_{\rm ell}^{\rm SMC} > 3.5$ kpc, we have reperformed our fits excluding these fields (i.e., including only fields with $R_{\rm ell}^{\rm SMC} < 3.5$ kpc), finding moderate values of the linear correlation coefficient ($\rho \geqslant 0.49$) for the more recent CSFH metrics τ_{90} and τ_{75} (still at high significance, p-value $< 10^{-3}$) and less evidence of linearity for τ_{50} ($\rho = 0.30$, p-value $= 0.013$). This is at least partially reflective of real field-to-field SFH variations, some of which are apparent in Figure 6. While our pointings do not coincide with any of the known substructure in the SMC other than the wing (e.g.,

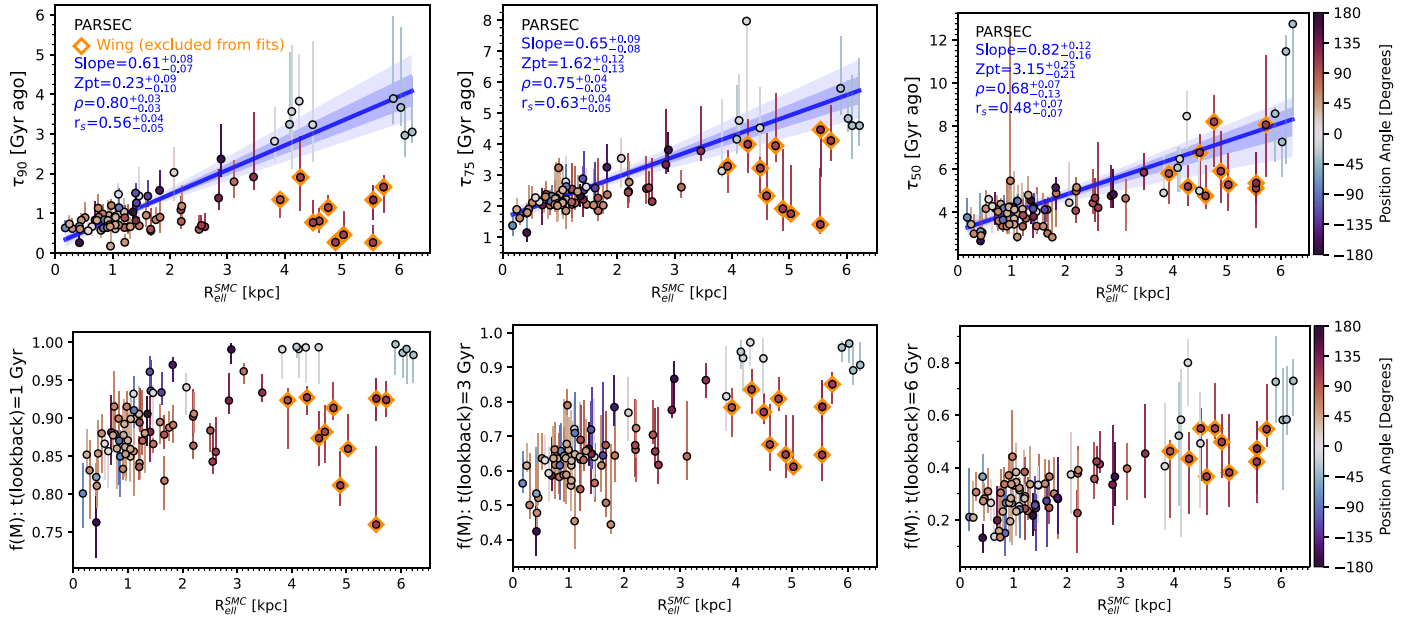

Figure 6. Lifetime SFH metrics vs. semimajor-axis equivalent distance from the optical center of the SMC $R_{\rm ell}^{\rm SMC}$. Top row: look-back time to form (from left to right) 90%, 75%, and 50% of the cumulative stellar mass as a function of $R_{\rm ell}^{\rm SMC}$. Fields are color coded by their position angle east of north, and fields in the wing of the SMC are shown in orange, highlighting their increasing discrepancy with the remainder of fields at similarly large $R_{\rm ell}^{\rm SMC}$ at recent look-back times. Linear fits excluding the wing fields are shown in blue, with dark (light) shading representing 1σ (2σ) uncertainties. The linear fit coefficients, Pearson linear correlation coefficient ρ, and Spearman rank correlation coefficient r_s are given in each panel. Bottom row: fraction of cumulative stellar mass formed by look-back times of (from left to right) 1, 3, and 6 Gyr, again vs. $R_{\rm ell}^{\rm SMC}$, with symbols as in the top row. Compared to other fields at similarly large distances from the center of the SMC ($R_{\rm ell}^{\rm SMC} > 3.5$ kpc), fields in the wing assembled a larger fraction of their mass more recently than ∼6 Gyr ago. Results shown assume PARSEC evolutionary models, and in Table 3 we give linear fit coefficients assuming other stellar evolutionary models for SFH fitting and a simple on-sky tangent plane (rather than elliptical) radius to characterize distance from the SMC center.

Table 3
Linear Fit and Correlation Coefficients of CSFH Metrics versus Radius

Metric	Model	Slope (Gyr kpc^{-1})	Zero-point (Gyr)	Pearson ρ	Spearman r_s
		Versus Elliptical Distance $R_{\rm ell}^{\rm SMC}$			
τ_{90}	PARSEC	$0.61^{+0.08}_{-0.07}$	$0.23^{+0.09}_{-0.10}$	$0.80^{+0.03}_{-0.03}$	$0.56^{+0.04}_{-0.05}$
τ_{90}	MIST	$0.68^{+0.11}_{-0.10}$	$0.13^{+0.11}_{-0.14}$	$0.77^{+0.04}_{-0.05}$	$0.56^{+0.04}_{-0.05}$
τ_{90}	BaSTI18	$0.62^{+0.09}_{-0.08}$	$0.24^{+0.10}_{-0.11}$	$0.76^{+0.04}_{-0.05}$	$0.53^{+0.04}_{-0.05}$
τ_{75}	PARSEC	$0.65^{+0.09}_{-0.08}$	$1.62^{+0.12}_{-0.13}$	$0.75^{+0.04}_{-0.05}$	$0.63^{+0.04}_{-0.05}$
τ_{75}	MIST	$0.71^{+0.12}_{-0.10}$	$1.69^{+0.16}_{-0.17}$	$0.69^{+0.05}_{-0.05}$	$0.55^{+0.06}_{-0.06}$
τ_{75}	BaSTI18	$0.66^{+0.11}_{-0.10}$	$1.64^{+0.15}_{-0.16}$	$0.70^{+0.05}_{-0.06}$	$0.58^{+0.05}_{-0.06}$
τ_{50}	PARSEC	$0.82^{+0.12}_{-0.16}$	$3.15^{+0.25}_{-0.21}$	$0.68^{+0.07}_{-0.13}$	$0.48^{+0.07}_{-0.07}$
τ_{50}	MIST	$0.89^{+0.13}_{-0.18}$	$3.68^{+0.28}_{-0.25}$	$0.65^{+0.07}_{-0.11}$	$0.45^{+0.07}_{-0.08}$
τ_{50}	BaSTI18	$0.96^{+0.13}_{-0.16}$	$3.21^{+0.26}_{-0.22}$	$0.69^{+0.06}_{-0.10}$	$0.49^{+0.07}_{-0.07}$
		Versus Projected On-sky Distance			
τ_{90}	PARSEC	$1.14^{+0.15}_{-0.13}$	$-0.05^{+0.11}_{-0.13}$	$0.74^{+0.03}_{-0.03}$	$0.52^{+0.04}_{-0.04}$
τ_{90}	MIST	$1.27^{+0.21}_{-0.17}$	$-0.18^{+0.15}_{-0.18}$	$0.72^{+0.04}_{-0.05}$	$0.54^{+0.04}_{-0.04}$
τ_{90}	BaSTI18	$1.16^{+0.18}_{-0.15}$	$-0.05^{+0.13}_{-0.16}$	$0.71^{+0.04}_{-0.04}$	$0.51^{+0.04}_{-0.05}$
τ_{75}	PARSEC	$1.24^{+0.16}_{-0.16}$	$1.29^{+0.16}_{-0.16}$	$0.71^{+0.04}_{-0.04}$	$0.60^{+0.05}_{-0.05}$
τ_{75}	MIST	$1.34^{+0.22}_{-0.19}$	$1.33^{+0.20}_{-0.21}$	$0.65^{+0.05}_{-0.05}$	$0.52^{+0.06}_{-0.06}$
τ_{75}	BaSTI18	$1.26^{+0.21}_{-0.19}$	$1.29^{+0.19}_{-0.20}$	$0.67^{+0.05}_{-0.06}$	$0.56^{+0.05}_{-0.06}$
τ_{50}	PARSEC	$1.52^{+0.21}_{-0.28}$	$2.78^{+0.30}_{-0.25}$	$0.62^{+0.07}_{-0.12}$	$0.48^{+0.07}_{-0.07}$
τ_{50}	MIST	$1.67^{+0.25}_{-0.32}$	$3.24^{+0.34}_{-0.30}$	$0.61^{+0.07}_{-0.10}$	$0.45^{+0.07}_{-0.08}$
τ_{50}	BaSTI18	$1.81^{+0.24}_{-0.31}$	$2.74^{+0.32}_{-0.28}$	$0.65^{+0.06}_{-0.09}$	$0.48^{+0.06}_{-0.07}$

A. Pieres et al. 2017; D. Mackey et al. 2018; D. Martínez-Delgado et al. 2019; D. El Youssoufi et al. 2021; L. R. Cullinane et al. 2023; P. Massana et al. 2024), the fields on the eastern side of the SMC (in the direction of the LMC) with $2 \lesssim R_{\rm ell}^{\rm SMC} \lesssim 3$ kpc tend to show indications of late-time star formation similar to the wing fields located even farther to the east. The preferentially higher mass fraction formed in the eastern fields over the past couple of gigayears was also detected by P. Massana et al. (2022) and may explain the eastward offset found in the spatial distribution of intermediate-

age stellar populations by D. Mackey et al. (2018). Furthermore, N. E. D. Noël et al. (2009) noted that among their fields located throughout the outer SMC in various directions, only their eastern fields showed ongoing star formation over the past ∼2 Gyr. Specifically, with the exception of their wing fields, all of the N. E. D. Noël et al. (2009) fields show similar SFH trends to our outer nonwing fields, supporting the idea that our outer nonwing fields are typical for their $R_{\rm ell}^{\rm SMC}$. Additional support comes from our lone field to the south of the SMC main body (SMC_A25), which has a mass assembly history essentially identical to the outer nonwing fields, completing nearly all of its star formation ($99.1\%^{+0.8}_{-1.8}$ of its cumulative stellar mass formed) by 1 Gyr ago (seen at $R_{\rm ell}^{\rm SMC} \sim 2.9$ kpc and position angle $\approx -170°$ in Figure 6).

We have provided the first quantitative measurements of the radial stellar age gradient in the SMC and its statistical significance. However, two previous studies have provided spatially resolved stellar age information over a large number of sight lines ($N > 100$), allowing us to calculate radial age gradients in the SMC for comparison with our results. First, stellar ages were provided for 10 noncontiguous ground-based imaging fields by A. E. Piatti (2012, see their Figure 1), who spatially divided each of their fields into a grid of 16 subregions for a total of 160 measurements. Calculating $R_{\rm ell}^{\rm SMC}$ for each of their fields identically to ours, assuming the same SMC center location, axis ratio, and position angle, their measurements yield a radial age gradient of $\delta(\text{age})/\delta(R_{\rm ell}^{\rm SMC}) = 1.56^{+0.39}_{-0.36}$ Gyr kpc^{-1} over $0.2 \gtrsim R_{\rm ell}^{\rm SMC} \gtrsim 5.5$ kpc, substantially steeper than any of the values we find in Figure 6. This difference is likely due at least in part to their methodology. In contrast to the CMD synthesis technique used here and in previous studies of the spatially resolved SFH in the SMC (J. Harris & D. Zaritsky 2004; N. E. D. Noël et al. 2009; S. Rubele et al. 2015, 2018; P. Massana et al. 2022), the age measurement technique used by A. E. Piatti (2012) was designed and calibrated using star clusters and measures the age of the dominant stellar population without any regard for the age *distribution*. Furthermore, the age calibration used by A. E. Piatti (2012), detailed in D. Geisler et al. (1997), is based on a third-order polynomial fit to ages for only six clusters, each with assumed ages nearly three decades old or more. A. E. Piatti (2012) also points out that his method for measuring cluster ages would in fact fail in the case of a constant SFH since his technique assumes the detection of a peak in the stellar age distribution. While he finds that this is not the case for the fields he analyzes, a constant SFH seems to be a nonnegligible possibility in the case of fields toward the SMC based on Figure 5.

The other study providing the necessary information to calculate age gradients is S. Rubele et al. (2018), based on contiguous near-infrared imaging from the VMC survey. A methodological issue with the A. E. Piatti (2012) ages is supported by results based on S. Rubele et al. (2018), yielding radial age gradients statistically consistent with our results in Figure 6. Using SFH results for individual VMC tile subregions from S. Rubele et al. (2018) and again performing linear fits versus $R_{\rm ell}^{\rm SMC}$ (excluding fields toward the wing[19] as in our analysis), we find radial gradient slopes of ($\delta\ \tau_{90}$, $\delta\ \tau_{75}$, $\delta\ \tau_{50}$)$/\delta(R_{\rm ell}^{\rm SMC}) = (0.64^{+0.02}_{-0.02}, 0.59^{+0.03}_{-0.03}, 0.65^{+0.04}_{-0.04})$ Gyr kpc^{-1}, in agreement with our results to within 1σ uncertainties. The agreement is particularly good at more recent look-back times (τ_{90}, τ_{75}), likely because of the shallower photometric depth of the VMC imaging (see Table 1 of S. Rubele et al. 2018). Furthermore, the agreement we find between our radial gradient slopes and those from S. Rubele et al. (2018), which are based on contiguous ground-based imaging, argues against spatially biased sampling affecting our radial age gradient measurements at a statistically significant level.

[19] We have excluded VMC tile 3_5 and subregions 1−3, 5−7, and 9 of tile 4_5.

4.3. Comparison to Previous Studies

While only A. E. Piatti (2012) and S. Rubele et al. (2018) provide sufficient spatial sampling of the SMC to quantify radial stellar age gradients for comparison with our results, more general comparisons with recent literature studies provide further validation of the SFH fits on which our radial age gradient measurements are based. In Figure 7, we compare our CSFHs from three spatially selected regions of the SMC, as in Figure 5, to CSFHs available in the literature. Each row of Figure 7 corresponds to a different assumed stellar evolutionary model in our SFH fitting, and each column corresponds to a different literature study for comparison, including (from left to right) SMASH (P. Massana et al. 2022), VMC (S. Rubele et al. 2018), and the WFPC2 fields analyzed by D. R. Weisz et al. (2013). Previous surveys tend to find CSFHs intermediate between our results for the inner and outer SMC, which is to be expected based on differences in spatial sampling. In particular, our fields are biased toward the inner SMC, with a median projected $R_{\rm ell}^{\rm SMC} = 1.3$ kpc, whereas SMASH excluded the innermost SMC owing to crowding, and VMC coverage was contiguous. Slight discrepancies are seen at early ($\gtrsim$7 Gyr) look-back times compared to the VMC results and at intermediate look-back times (∼2−4 Gyr) compared to the D. R. Weisz et al. (2013) results, although additional causes include differences in assumed stellar evolutionary model, SMC distance, and details of the SFH fitting methodology used in each study. The minor ($<2\sigma$) differences seen between our CSFHs and those from the VMC survey at early look-back times are not present in the comparison to SMASH, implying that the shallower imaging and/or near-infrared wavelength regime used by VMC may be contributing factors. Furthermore, unlike our approach, each of the literature studies assumed a single set of evolutionary models for SFH fitting, rendering it impossible to assess the impact of this choice on their results.

Regarding the comparison to D. R. Weisz et al. (2013) in the right column of Figure 7, discrepancies in the CSFH at intermediate ages (2−6 Gyr) can also be traced to differences in spatial coverage. The combined CSFH from D. R. Weisz et al. (2013), based on only seven WFPC2 fields, is dominated by the innermost three of these fields at $R_{\rm ell}^{\rm SMC} < 1$ kpc, which are much more well populated. Accordingly, viewed on a per-field basis, the D. R. Weisz et al. (2013) results are in reasonable agreement with our measurements since their three innermost fields have $\tau_{50} \sim 3$ Gyr, while the outer four fields, with $R_{\rm ell}^{\rm SMC} \sim 4$ kpc, have $\tau_{50} \sim 7$ Gyr (see Figure 4 of D. R. Weisz et al. 2013), quite similar to our results in the top left panel of Figure 6 given different assumptions on distance, extinction, and input stellar evolutionary models between our study and D. R. Weisz et al. (2013). In addition, detailed per-field CSFH comparisons can function as checks of both internal and external consistency, so we provide further comparisons along with our results for all individual fields in Appendix C.

In Figure 8, we show the AMR obtained by statistically combining all of our SMC fields as a black line, with

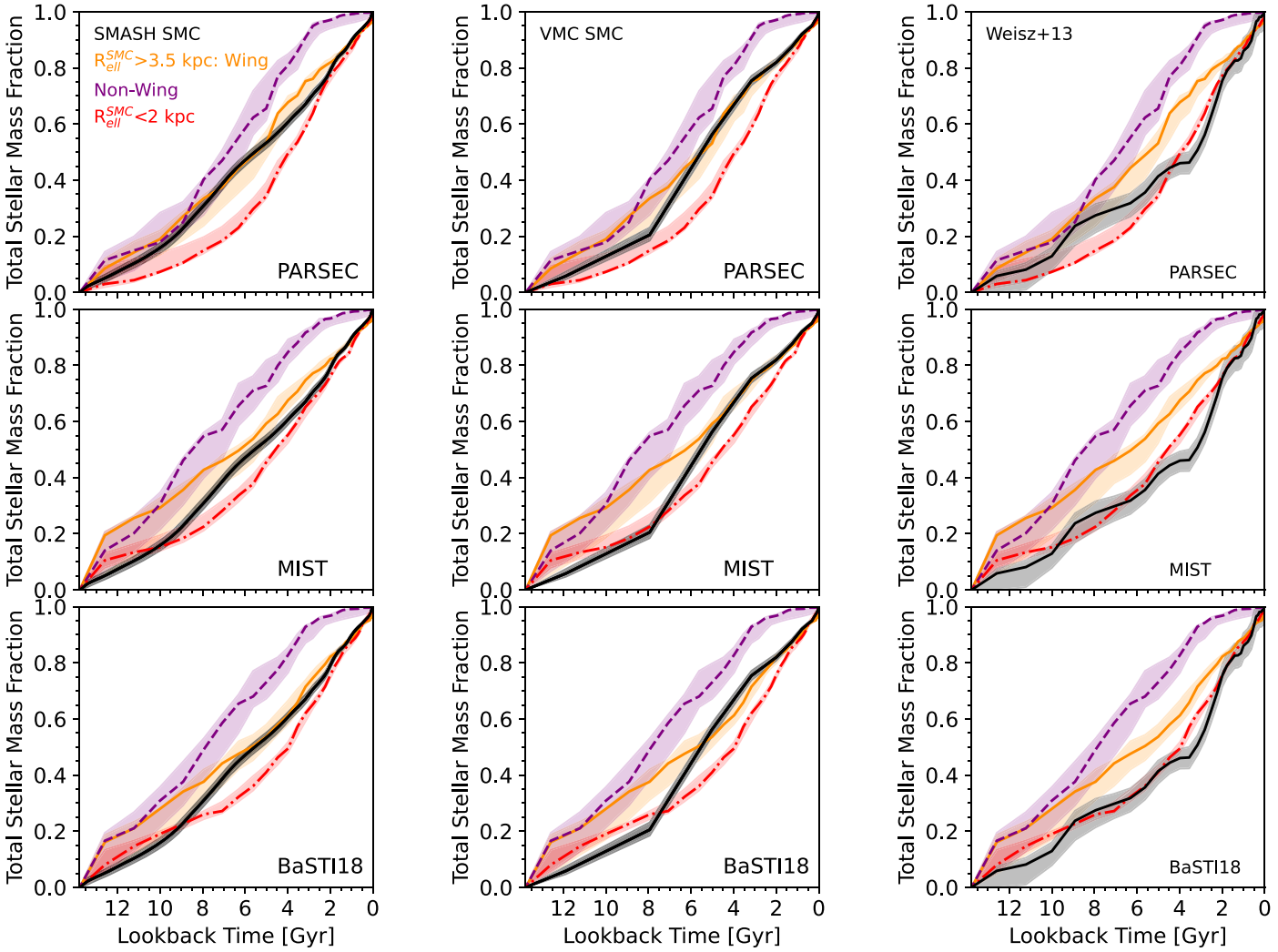

Figure 7. Comparison between our combined CSFHs for different spatial regions in the SMC (shown as in Figure 5) and SMC CSFHs from P. Massana et al. (2022; left column), S. Rubele et al. (2018; middle column), and D. R. Weisz et al. (2013; right column). Each row corresponds to a different stellar evolutionary model that we assumed when calculating our SFH results, while each of the literature SFH studies shown used a single, different evolutionary model. Agreement is generally good, especially given differences in spatial sampling of the SMC.

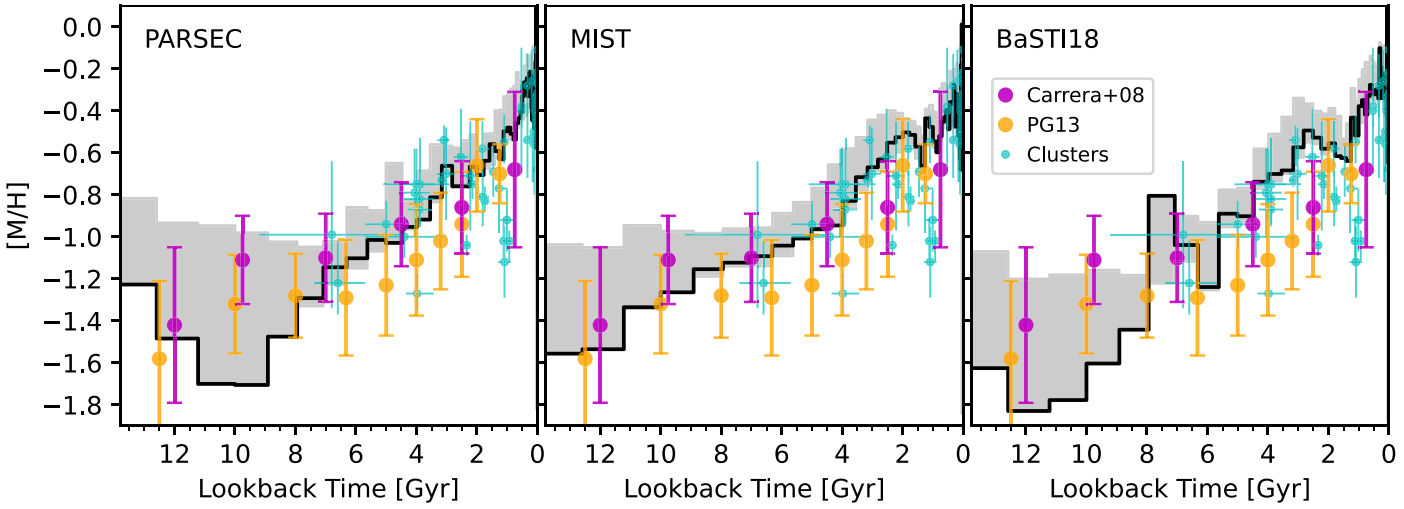

Figure 8. Combined SMC AMR for each of our three assumed evolutionary models. The SMC field AMRs from R. Carrera et al. (2008) and A. E. Piatti & D. Geisler (2013) are overplotted in magenta and orange, respectively, and SMC clusters are overplotted in cyan, with ages and metallicities from F. F. S. Maia et al. (2019), B. Dias et al. (2021, 2022), and R. A. P. Oliveira et al. (2023).

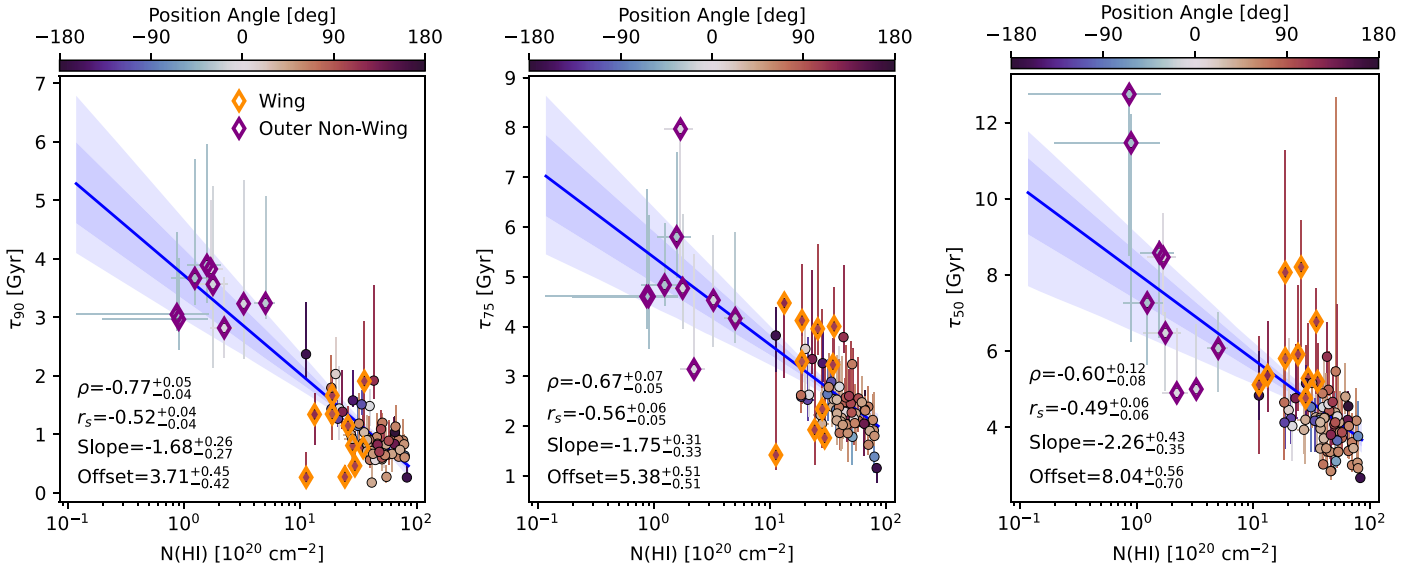

Figure 9. Relationship between look-back time to form a given mass fraction (from Figure 6) vs. H I column density (N. M. Pingel et al. 2022). The Pearson linear correlation coefficient ρ and the Spearman rank correlation coefficient r_s are given in the lower left corner of each panel vs. $\log_{10}N$(H I), along with the coefficients of the best-fit line (shown in blue). The mass assembly histories of our fields correlate loosely with present-day N(H I) over a broad range of look-back times, although this may simply reflect the fairly concentrated present-day H I morphology of the SMC.

uncertainties indicated by gray shading. This AMR is compared to results for SMC field stars from Ca II triplet spectroscopy by R. Carrera et al. (2008) and isochrone-based field star ages and metallicities from A. E. Piatti & D. Geisler (2013), as well as isochrone-fitting values for clusters from F. F. S. Maia et al. (2019), B. Dias et al. (2021, 2022), and R. A. P. Oliveira et al. (2023). Given that we imposed no restrictions whatsoever on the allowed AMR in any of our fields, agreement is very good (generally within uncertainties), providing an important validation of our SFH fitting procedure. Again, minor discrepancies are due to differences in spatial sampling of the SMC, with lower literature metallicities resulting from more radially distributed targeting of the SMC field in literature studies (R. Carrera et al. 2008; A. E. Piatti & D. Geisler 2013) given its negative radial metallicity gradient (e.g., S. Choudhury et al. 2020; J. Grady et al. 2021; P. Massana et al. 2024).

5. Discussion

Overall, our SFH results imply that in the SMC the spatial distribution of its stellar populations is characterized globally by an outside-in present-day age gradient but modified by the LMC–SMC interaction in a location-dependent way. The global, long-term nature of the outside-in age gradient suggests that it is driven primarily by in situ (rather than external) processes, which consist of at least two nonexclusive possibilities. One potential explanation for the lack of recent star formation in the outer SMC could be outside-in quenching due to a shrinking gas reservoir (e.g., G. S. Stinson et al. 2009). This idea is supported by an outside-in cessation of star cluster formation over the past gigayear (T. Bitsakis et al. 2018; E. Bica et al. 2020), as well as a correlation between the H I column density N(H I) and our CSFH metrics (τ_{90}, τ_{75}, τ_{50}) over a broad range of look-back times, shown in Figure 9. However, given the turbulent interaction history of the SMC and its complex present-day H I position and velocity structure, such a correlation may simply reflect the fact that N(H I), in a gross sense, tends to decrease moving away from the SMC center. Indeed, at sufficiently recent look-back times, the correlation breaks down—the correlation between τ_{99} (sampling the most recent 0.5 Gyr to within uncertainties) and N (H I) has Spearman $r_s = -0.14^{+0.10}_{-0.08}$ at low statistical significance (p-value > 0.1).

Another potential explanation for the present-day outside-in age gradient is that older stellar populations have been driven to preferentially larger radii over time by star formation feedback (see A. S. Graus et al. 2019 and references therein). Observationally, this idea is supported by the ubiquity of an extended, round stellar component seen for SMC-mass dwarfs regardless of environment or color (E. Kado-Fong et al. 2020), while simulations predict that feedback-driven stellar radial migration is most efficient at SMC-like masses (K. El-Badry et al. 2016). However, in addition to these two internally driven processes, the extended LMC–SMC interaction may have also contributed to the present-day observed radial age gradient. Simulations predict that galaxy–galaxy interactions can dynamically heat stars in the outer regions of disks, temporarily inducing large radial excursions on timescales of a few hundred megayears (C. Carr et al. 2022). Such interaction-driven dynamical heating is directly observed in the LMC (Y. Choi et al. 2022), and further modeling work is needed to address whether this phenomenon is relevant to the SMC.

Our results also suggest that infall into the Milky Way may not have played an important role in regulating star formation in the SMC. The discrepancy in the star formation rates between the wing and outer nonwing fields begins $\sim$3−6 Gyr ago (see Figure 6 and the right panel of Figure 5). This timing argues against ram pressure stripping as the cause of a lack of younger ($\lesssim$3−4 Gyr) stars in the outer SMC since the LMC and SMC likely did not enter the Milky Way's virial radius until $\sim$1−2 Gyr ago (N. Kallivayalil et al. 2006; G. Besla et al. 2012; E. Patel et al. 2017). More generally, our results highlight the idea that the constraining power of our spatially resolved lifetime SFHs is maximized when leveraged together with the wealth of additional information available for sight lines toward the SMC, so, with this in mind, we now examine

our SFH fits in the context of available stellar kinematics and abundances. We then place our SFH results in context with our companion study of the LMC, compare them with other nearby dwarf galaxies, and finally describe some plans for future studies enabled by this work.

5.1. Constraints from Stellar Kinematics and Abundances

In the wing, in contrast to the rest of the outer SMC, we find a best-fit SFH consisting of nearly constant star formation over the past ∼3−4 Gyr (in fact, over its entire lifetime; see Figure 5), implying that multiple previous LMC–SMC interactions played a role in sustaining star formation there. On one hand, the most recent LMC–SMC collision ∼150 Myr ago (P. Zivick et al. 2018; Y. Choi et al. 2022) has been put forth as a contender for generating foreground tidal debris along sight lines toward the wing, in addition to the Magellanic Bridge, based largely on a comparison to simulations (e.g., J. D. Diaz & K. Bekki 2012; P. Zivick et al. 2019). Accordingly, the constant SFH we observe is at least partially a consequence of composite stellar populations viewed along the line of sight, evidenced by bimodalities in stellar kinematics and distances (e.g., P. D. Dobbie et al. 2014b; D. El Youssoufi et al. 2021, 2023; D. James et al. 2021; A. Mucciarelli et al. 2023). In addition, star clusters toward the wing show a broad range of star cluster distances, ages, and metallicities, including both a young ($\lesssim$200 Myr) metal-rich in situ component and a metal-poor component with a broad range of ages (0.5−7 Gyr; R. A. P. Oliveira et al. 2023).

Stellar kinematics and chemical abundances (A. O. Omkumar et al. 2021; A. Almeida et al. 2024) have both been used to argue that the recent LMC–SMC collision was responsible for transporting stars outward from the inner SMC (and, in one case, toward a field as far as $\gtrsim$9 kpc from the optical center of the SMC; L. R. Cullinane et al. 2023). Proper-motion measurements in the eastern SMC and the wing are reasonably consistent with this hypothesis, given residual mean motions toward the Magellanic Bridge of ∼0.25 mas yr^{-1} (∼75 km s^{-1}) for red giant branch (RGB) stars (P. Zivick et al. 2018, 2021; M. De Leo et al. 2020), naively translating to a travel time of ∼13 Myr kpc^{-1}. The link between the recent LMC–SMC collision and the bimodal stellar distance distribution is also consistent with the locations of the peaks in the bimodal radial velocity distribution of red giants toward the eastern SMC (D. James et al. 2021).

However, additional LMC–SMC interactions previous to the most recent collision must have also contributed to star formation in the wing given its near-constant star formation rate. A previous interaction ∼1.7−2 Gyr ago (which likely created the Magellanic Stream; e.g., D. L. Nidever et al. 2008; G. Besla et al. 2012; J. D. Diaz & K. Bekki 2012) could have played at least two roles: First, this interaction may also have been responsible for sourcing stars from the inner SMC, explaining the quite mild ($\lesssim$0.2 dex) metal-rich offset in the metallicity distribution of the less distant of the two line-of-sight components reported by A. Almeida et al. (2024). Second, this interaction almost certainly triggered some in situ star formation in the wing as well, evidenced by the spike in stellar cluster production in the outer SMC ∼2 Gyr ago, possibly due to interaction-enhanced massive giant molecular cloud formation (T. Bitsakis et al. 2018; M. L. Williams et al. 2022). An even earlier LMC–SMC interaction also played an important role of course, since the peak of star formation in the wing was ∼4 Gyr ago. This is roughly contemporaneous with the increase in star formation rate in the LMC and SMC more generally (D. R. Weisz et al. 2013; P. Massana et al. 2022), as well as a change in chemical abundance trends in the SMC (J. T. Povick et al. 2023). This earlier interaction ∼3−4 Gyr ago could also be responsible for the lack of stellar clusters older than ∼3 Gyr in the northeastern SMC (M. C. Parisi et al. 2024), corroborated by a drop-off in the star cluster age distribution in the outer LMC as well (M. Gatto et al. 2024). Furthermore, a correspondence between SFH features and LMC–SMC interactions extending to at least ∼2−3.5 Gyr ago was reported by J. D. Sakowska et al. (2024) for the shell-like feature ∼2 deg to the northeast of the SMC optical center (they report star formation rates quite similar to our wing fields, $\Sigma_{\rm SFR} \sim (0.5-1) \times 10^{-3}\,M_{\odot}\,{\rm yr}^{-1}\,{\rm kpc}^{-2}$, peaking ∼200 Myr ago at $\sim 3 \times 10^{-3}\,M_{\odot}\,{\rm yr}^{-1}\,{\rm kpc}^{-2}$).

5.2. Comparison to the LMC

The multitude of previous LMC–SMC interactions has left detectable imprints on the lifetime SFH of each Magellanic Cloud when viewed in a spatially resolved way. In the SMC, this is exemplified by the recent star formation toward the wing, atypical compared to other fields at similar $R_{\rm ell}^{\rm SMC}$ (Figures 5 and 6). In the LMC, interactions have likely played a similarly important but somewhat indirect role, boosting radial migration to create a "V-shaped" radial age gradient as seen in some other similarly massive ($M_{\star} \gtrsim 10^{9}\,M_{\odot}$) late-type galaxies (discussed in Cohen et al. 2024 and references therein). In addition, while the gaseous content of both Magellanic Clouds is clearly indicative of previous disturbances, repeated LMC–SMC interactions have wreaked havoc on the H I morphology and kinematics of the less massive SMC. For this reason, unlike in our analysis of the LMC (Cohen et al. 2024), we have not presented radial age gradients under the assumption of an SMC center location based on H I kinematics; given the finding of two (or possibly more) components with a complex interplay discussed by C. E. Murray et al. (2024), the utility of attempting to define such a center seems somewhat unclear.

While the LMC and SMC have clearly distinct *intra*galaxy stellar age trends, trends in their *global* (i.e., galaxy-wide) mass assembly histories over cosmic time (i.e., CSFHs) are quite similar, with both Magellanic Clouds having lifetime SFHs approximating constant star formation. This is illustrated in Figure 10, showing that our combined LMC CSFH from Cohen et al. (2024) falls intermediate between the CSFHs of the different SMC regions we analyze. Simulations predict that such constant SFHs, as well as some detectable galaxy-to-galaxy scatter, are fairly generic features of SMC-to-LMC-mass galaxies in the vicinity of massive hosts (C. Engler et al. 2023). These simulations further predict that at LMC/SMC-like galaxy masses these constant SFHs are quite insensitive to time of infall, reinforcing independent predictions that quenching times are maximized at LMC/SMC-like satellite masses (A. R. Wetzel et al. 2015). These predictions are generally supported by observed SFHs for Local Group dwarfs, especially given the near-constant SFHs observed for some relatively more isolated, massive, gas-rich Local Group dwarf irregulars (e.g., D. R. Weisz et al. 2014, 2015; E. D. Skillman et al. 2014). Hence, current evidence, although sparse, seems to suggest that prolonged dwarf–dwarf interactions are not a prerequisite for constant lifetime SFHs in the Local Group,

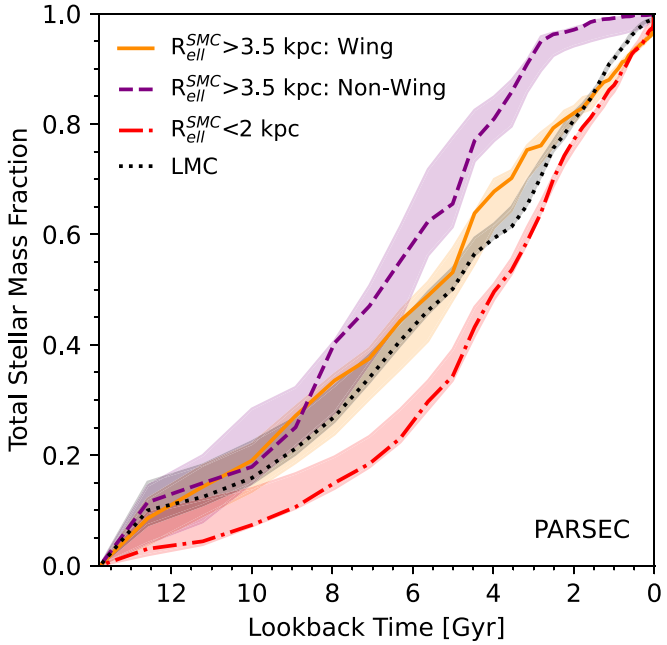

Figure 10. CSFHs for different SMC regions as in the left panel of Figure 5, but now with our combined CSFH for the LMC (Cohen et al. 2024) overplotted as a black dotted line.

although stringent comparisons to simulations will require larger samples in more diverse (i.e., isolated) environments.

5.3. The Outside-in Present-day Age Gradient in Context

Our results reveal a dichotomy where the LMC and SMC have nearly identical trends in their CSFHs when viewed globally but have schematically different *internal* radial age trends when viewed in a spatially resolved way. In fact, the SMC effectively sets an upper limit on the stellar mass of dwarf galaxies observed to have outside-in age gradients. An increase in average age with radius has been observed (or inferred from stellar metallicity gradients) in numerous Local Group dwarfs (D. Faria et al. 2007; S. L. Hidalgo et al. 2013; G. Beccari et al. 2014; C. E. Martinez-Vazquez et al. 2015; F. A. Santana et al. 2016; A. del Pino et al. 2017; M. Bettinelli et al. 2019; S. M. Albers et al. 2019; A. B. Pace et al. 2020; T. Ruiz-Lara et al. 2021; V. Rusakov et al. 2021; H. Abdollahi et al. 2023), but all of these dwarfs are at least an order of magnitude less massive than the SMC, with the next most massive being the gas-rich dwarf irregular Wolf–Lundmark–Melotte galaxy ($M_\star \approx 4.7 \times 10^7 M_\odot$; A. W. McConnachie 2012). For comparison, estimates of the stellar mass of the SMC range from $\sim 3.0 \times 10^8\ M_\odot$ to $4.8 \times 10^8\ M_\odot$ within the inner $\sim 3-4$ kpc (J. Harris & D. Zaritsky 2004; R. A. Skibba et al. 2012; S. Rubele et al. 2018; E. M. Di Teodoro et al. 2019; M. De Leo et al. 2023). Furthermore, these values are likely lower limits, since the old (red giant and red clump) stellar population of the SMC extends to $\gtrsim$8 kpc (P. Massana et al. 2020), and the SMC hosts a variety of additional stellar substructure in its periphery (e.g., A. Pieres et al. 2017; D. Mackey et al. 2018; D. El Youssoufi et al. 2021; L. R. Cullinane et al. 2023; V. Chandra et al. 2023). It bears mention that outside-in age gradients have been reported for a few galaxies much more massive than the SMC ($\log_{10} M_\star/M_\odot \gtrsim 10$; S. M. Staudaher et al. 2019) based on fits to spectral energy distributions (SEDs) from broadband imaging (D. A. Dale et al. 2020), but these age measurements assume a parametric (delayed-τ) SFH (discussed by, e.g., A. C. Carnall et al. 2019), inconsistent with observed SFHs for dwarfs showing outside-in age gradients in at least some cases (e.g., T. Ruiz-Lara et al. 2021; V. Rusakov et al. 2021; see the discussion of "fast" vs. "slow" dwarfs by C. Gallart et al. 2015).

While all of the Local Group dwarfs with outside-in age gradients are less massive than the SMC, the converse is not true—not all dwarfs less massive than the SMC have outside-in age gradients. For example, NGC 6822 has a flat age gradient out to $\sim$2.5 disk scale lengths, although it may have undergone previous interactions based on the flattened, twisted stellar morphology in its outskirts (J. M. Cannon et al. 2012; F. Fusco et al. 2014; S. Zhang et al. 2021). More generally, a variety of age gradients are implied in late-type Local Volume dwarfs based on radial distributions of both blue helium-burning stars and asymptotic giant branch stars relative to red giants (K. B. W. McQuinn et al. 2012, 2017). Similarly, radial age gradients ranging from outside-in to flat are predicted in dwarfs by at least one set of zoom-in hydrodynamical cosmological simulations (A. S. Graus et al. 2019). In these simulations, feedback-driven stellar radial migration creates the outside-in gradient, which can be counteracted by late-time star formation at large radii, flattening the outside-in gradient. The A. S. Graus et al. (2019) simulations predict, as a result of these competing processes, a correlation between global mass assembly history (quantified by galaxy-wide τ_{50} and τ_{90}) and radial age gradient slope, such that globally older galaxies show steeper outside-in age gradients (normalized to their half-mass radius). Observationally, such a trend has yet to be confirmed or refuted, as the sample of dwarfs with directly measured radial age gradients is both minuscule and severely biased, limited to the Local Group by observational capabilities. Fortunately, radial age gradient measurements of more distant targets are now within the reach of modern observational facilities, and radial age gradient measurements of a larger sample will be presented elsewhere (R. E. Cohen 2024).

5.4. Caveats and Future Work

It is evident (e.g., from the discussion in Section 5.1) that high-dimensional information, combining ages, distances, kinematics, and chemical abundances of resolved stars (and/or stellar clusters), provides additional leverage toward disentangling the history of the LMC–SMC–Milky Way system; it is equally evident that this task is far from complete. Our SFH fitting technique assumes a single line-of-sight distance, and in Appendix B we demonstrate that this assumption does not impact our SFH results beyond their uncertainties. However, the ability to simultaneously solve for the ages and distances of individual resolved stars could provide the diagnostic power needed to map the contributions of particular LMC–SMC interactions to the present-day stellar content of the SMC and its substructures, posing strong constraints for models of the LMC–SMC interaction. Indeed, SFH fitting methodologies that incorporate nonnegligible stellar distance distributions have already been applied to substructure in the SMC in at least one instance (J. D. Sakowska et al. 2024). As another example, A. Almeida et al. (2024) used Gaia-based distances and kinematics together with abundances of resolved stars to characterize the two line-of-sight components toward the SMC's wing. However, their stellar sample was composed exclusively of red giants with

available spectroscopic abundances, preventing precise individual stellar age and distance measurements.

In forthcoming studies of this series, we will apply a technique that fits the SED of each star to simultaneously solve for stellar and dust properties on a star-by-star basis (K. D. Gordon et al. 2016). In contrast to our approach, which uses the well-established CMD synthesis technique for each field, the star-by-star SED-fitting approach can provide, among other things, individual stellar ages and distances and their uncertainty distributions (C. E. Murray 2024). This approach has already been used to characterize differences in the three-dimensional structure of stars and dust toward the southwestern bar of the SMC (P. Yanchulova Merica-Jones et al. 2021) and will be applied to new imaging toward the wing (C. Lindberg 2024, in preparation), offering tantalizing possibilities for understanding the evolution of the SMC. As one example of these possibilities, A. Almeida et al. (2024) point out that disentangling the stellar age, distance, and chemical abundance distributions of the two line-of-sight components toward the wing can confirm the hypothesis that the nearby component was stripped from the inner SMC by the most recent LMC–SMC interaction. Another intriguing possibility is to definitively refute (or confirm) a scenario where the LMC and SMC are not on first infall and have instead made multiple previous pericentric passages of the Milky Way, suggested by E. Vasiliev (2024). Our SFHs are not incompatible with such a scenario and include subtle hints of a star formation enhancement $\sim$7$-$8 Gyr ago in both the SMC (right panel of Figure 5) and LMC (Figure 14 of Cohen et al. 2024). E. Vasiliev (2024) details that current data cannot completely rule out the multiple-passage scenario, and high-dimensional, high-fidelity information for large stellar samples along many sight lines may provide critical clues. Fortunately, in addition to deep multiwavelength imaging, steps in this direction are already being taken with massively multiplexed spectroscopic campaigns targeting the LMC and SMC (e.g., M.-R. L. Cioni et al. 2019; A. Almeida et al. 2023).

6. Conclusions

We have harnessed together 83 individual HST imaging fields toward the SMC and fit lifetime SFHs to each individually. We have combined fields by location within the SMC to quantify differences in their assembly histories (Section 4.1) and used per-field results to measure radial stellar age gradients in the SMC (Section 4.2), using simulations to verify that our SFH fits are robust to various line-of-sight distance distributions (Appendix B). Our main results are as follows:

1. We observe an outside-in age gradient in the SMC. Assuming PARSEC evolutionary models and an elliptical geometry for the SMC, we find radial age gradient slopes of $\delta(\tau_{90},\ \tau_{75},\ \tau_{50})/\delta R = (0.61^{+0.08}_{-0.07},\ 0.65^{+0.09}_{-0.08},\ 0.82^{+0.12}_{-0.16})$ Gyr kpc^{-1}. The correlation between look-back time to form a given cumulative mass fraction (i.e., τ_{90}, τ_{75}, τ_{50}) and distance from the optical center of the SMC remains linear (Pearson $\rho > 0.6$) at high statistical significance (p-values $< 10^{-3}$) regardless of choice of stellar evolutionary model for SFH fits or the parameterization of distance from the SMC center as linear or elliptical (semimajor-axis equivalent). We argue that the observed age gradient is driven primarily by in situ processes, supported by timing arguments, including a similar trend seen in star cluster ages.
2. Fields in the inner SMC ($R_{\rm ell}^{\rm SMC} < 2$ kpc) have been forming stars throughout its lifetime at a rate that is approximately constant and an order of magnitude higher than stars farther from the SMC center ($R_{\rm ell}^{\rm SMC} > 3.5$ kpc). In accord with previous studies, we also find evidence for a further enhancement in star formation $<$150 Myr ago, following the most recent LMC–SMC collision (right panel of Figure 5). However, our data are insufficient to more precisely age-date this star formation enhancement or assess whether it is global in nature.
3. In contrast to the remainder of the outer SMC (3.5 kpc $< R_{\rm ell}^{\rm SMC} <$ 6.5 kpc), fields in the vicinity of the wing show near-constant best-fit SFHs even over the most recent $\sim$3$-$4 Gyr. This is likely due to a superposition of multiple stellar components along the line of sight, including tidal debris. Kinematics of RGB stars are consistent with the hypothesis of such tidal debris being stripped from the inner SMC during the most recent LMC–SMC collision, but earlier interactions likely also played a role, supported by both the field star metallicity distribution and the age distribution of star clusters in the outer SMC.

Acknowledgments

It is a pleasure to thank Michele Cignoni, Pol Massana, and Dan Weisz for sharing SFH results for comparison and the anonymous referee for their detailed and constructive comments. Some of the data presented in this article were obtained from the Mikulski Archive for Space Telescopes (MAST) at the Space Telescope Science Institute. The specific observations analyzed can be accessed via doi:10.17909/8ads-wn75. Based on observations with the NASA/ESA Hubble Space Telescope obtained at the Space Telescope Science Institute, which is operated by the Association of Universities for Research in Astronomy, Incorporated, under NASA contract NAS 5-26555. Support for programs HST GO-15891, GO-16235, and GO-16786 was provided by NASA through a grant from the Space Telescope Science Institute, which is operated by the Association of Universities for Research in Astronomy, Inc., under NASA contract NAS 5-26555. R.E.C. acknowledges support from Rutgers, The State University of New Jersey.

Facility: HST (ACS/WFC, WFC3/UVIS, WFPC2).

Software: astropy (Astropy Collaboration 2022), matplotlib (J. D. Hunter 2007), numpy (C. R. Harris et al. 2020), emcee (D. Foreman-Mackey et al. 2013), Dolphot (A. E. Dolphin 2000), MATCH (A. E. Dolphin 2002).

Appendix A
Clusters Removed from Fields

Using the E. Bica et al. (2020) star cluster catalog, we have removed from our photometric catalogs all sources within their listed semimajor-axis distance $R_{\rm SMA}$ from their cluster centers before fitting SFHs. The relevant clusters and affected fields are listed along with the cluster centers and semimajor axes from E. Bica et al. (2020) in Table 4. The cluster name given in the first column corresponds to the name used in the SIMBAD database, with any alternate names given in the following

column. To gauge how much of the cluster population is removed by our spatial cut using R_{SMA} from E. Bica et al. (2020), in Figure 11 we compare R_{SMA} against R_{90} from A. Hill & D. Zaritsky (2006), the radius enclosing 90% of the cluster light based on surface brightness profile fits. Among the 15 clusters matched to the sample analyzed by A. Hill & D. Zaritsky (2006), the E. Bica et al. (2020) semimajor-axis values we use are equal to or greater than the radius enclosing 90% of the cluster light to within uncertainties in all cases except one cluster (OGLE-CL SMC 35) for which uncertainties on the surface brightness profile fits were not given by A. Hill & D. Zaritsky (2006).

As an additional check, we intentionally select the field with the worst cluster contamination by projected area, which is SMC_20, with the cluster Bruck 100 occupying 1.54 arcmin^2, or 21% of the field of view based on its $R_{SMA} = 0.'7$ (E. Bica et al. 2020). This is shown in the top left panel of Figure 12, where stars within R_{SMA} are color coded by their distance from the center of the cluster and stars outside R_{SMA}, retained in our catalog, are shown in gray. The remaining three left panels of Figure 12 compare the CMD loci of stars using this spatial selection. To assess the impact of the cluster on the CSFH in the limiting case where no cluster stars were removed, we have recalculated the CSFH of the entire field of view without removing any stars. The results are shown in the three panels in the right column of Figure 12, with each panel corresponding to a different assumed stellar evolutionary model. Comparing the CSFHs obtained removing all stars within R_{SMA} (orange) to the CSFHs obtained without removing any stars (blue), we find that the values of τ_{50}, τ_{75}, and τ_{90} are not impacted beyond their uncertainties.

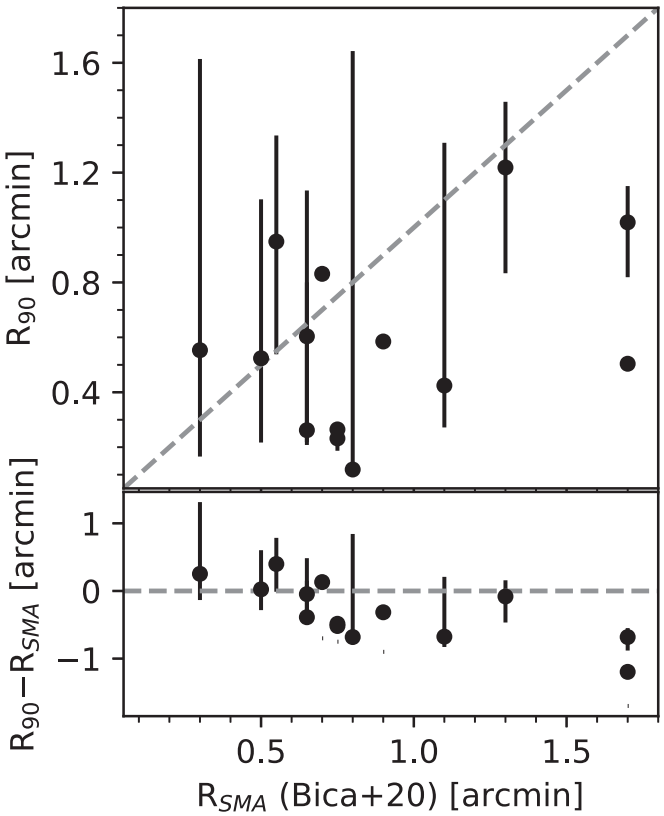

Figure 11. Comparison of R_{90}, the radius enclosing 90% of the cluster light from A. Hill & D. Zaritsky (2006), against R_{SMA}, the cluster semimajor axis from the E. Bica et al. (2020) catalog inside which we remove all stars from our catalogs before fitting SFHs. Among the 15 clusters in common, all but one have $R_{SMA} \geqslant R_{90}$ to within uncertainties.

Table 4
Known Clusters Excluded from Photometric Catalogs

Cluster	Other Names	R.A. (J2000) (deg)	Decl. (J2000) (deg)	Radius (arcmin)	Field
OGLE-CL SMC 131		15.515833	−72.521111	0.70	SMC_2
OGLE-CL SMC 144	OGLE-CL SMC 236	16.021667	−72.120556	0.60	SMC_8
BS95 11	SBica7	9.580000	−73.378611	0.30	SMC_15
OGLE-CL SMC 137	B115, RZ144	15.846667	−72.650833	0.90	SMC_18
OGLE-CL SMC 140	BS118	16.057083	−72.646111	1.30	SMC_18
HGH2008 Cluster 1	SSN16	14.879167	−72.153056	0.20	SMC_19
Bruck 100		15.099583	−72.089167	0.70	SMC_20
OGLE-CL SMC 221	H86-164	13.937917	−72.704444	0.45	SMC_25
Cl Kron 28	L43,RZ69	12.923750	−71.998333	1.70	SMC_35
OGLE-CL SMC 73	B59, RZ70	12.932083	−72.840833	0.80	SMC_41
H86 173		14.338333	−72.576111	0.50	SMC_42
Bruck 135		17.341250	−73.188611	0.70	SMC_44
OGLE-CL SMC 67	L41, RZ67, BMS231	12.732500	−72.726389	0.65	SMC_45
NGC 416	K59, L83, ESO29-SC32, OGLE-CL SMC 158	16.996250	−72.355000	1.70	SMC_46
BS95 138	RZ164	16.816250	−72.102500	1.30	SMC_49
OGLE-CL SMC 248		22.455000	−73.430278	1.50	SMC_52
OGLE-CL SMC 286		22.639167	−73.422500	1.50	SMC_52
OGLE-CL SMC 134	RZ143,K47,L70	15.797500	−72.272222	0.75	SMC_54
HW 63	RZ182	17.551250	−73.208889	0.75	SMC_53
OGLE-CL SMC 204	H86-121	12.840000	−73.138333	0.55	SMC_A4
OGLE-CL SMC 75	H86-126	12.973333	−73.098333	0.50	SMC_A4
H86 146		13.413333	−72.392778	0.90	SMC_A10
H86 142		13.394583	−72.490278	0.90	SMC_A11
Bruck 143	RZ192	18.183333	−72.750000	0.50	SMC_A12
RZ2005 38		11.121250	−72.815833	0.80	SMC_A13
OGLE-CL SMC 151		16.554583	−72.794167	1.20	SMC_A16

Table 4
(Continued)

Cluster	Other Names	R.A. (J2000) (deg)	Decl. (J2000) (deg)	Radius (arcmin)	Field
OGLE-CL SMC 152		16.587500	−72.830000	0.65	SMC_A16
OGLE-CL SMC 6		9.889167	−73.176944	0.80	SMC_A17
RZ2005 180	HW61	17.426250	−72.295278	0.65	SMC_A21
OGLE-CL SMC 103	RZ95,B83	13.876667	−73.072222	0.55	SMC_W1
OGLE-CL SMC 185	H86-84	11.641667	−72.765556	0.40	SMC_W6
OGLE-CL SMC 35	RZ48,H86-83	11.641667	−72.773889	0.70	SMC_W6
OGLE-CL SMC 36	RZ47,L31	11.648750	−72.741111	1.10	SMC_W6
OGLE-CL SMC 181		11.366667	−72.885833	0.70	SMC_W7
RZ2005 43		11.414583	−72.861944	0.30	SMC_W7
Bruck 36		11.424583	−72.841389	0.70	SMC_W7

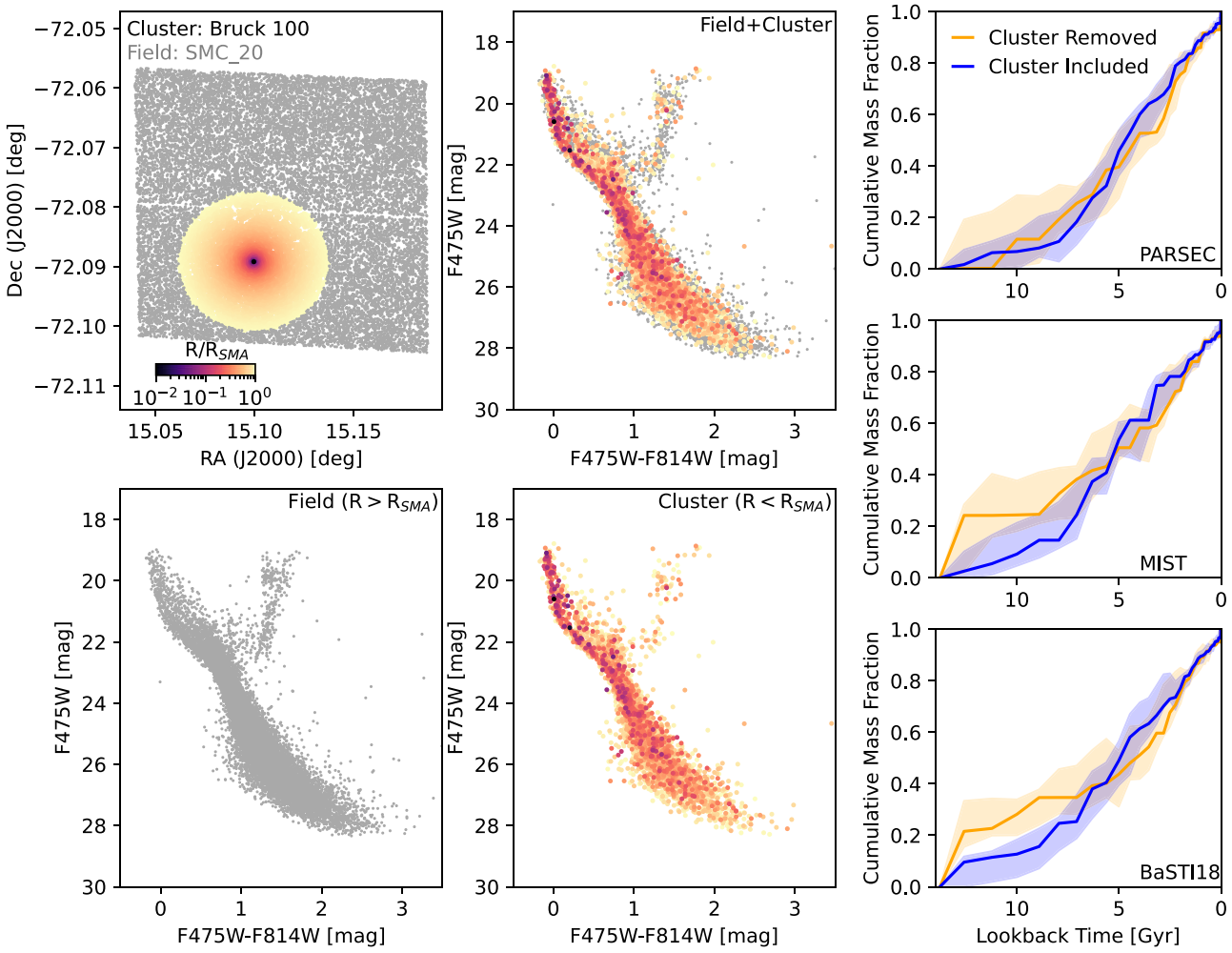

Figure 12. An example of our removal of known clusters from our fields and its impact on the resulting CSFH. This example corresponds to the most pessimistic case, in which the cluster (Bruck 100) occupies the largest projected area (1.54 arcmin^2, or 21% of the field of view) in any of our target fields. In the left four panels, stars removed from our catalog are color coded by distance from the center of the cluster $R_{\rm SMA}$ listed by E. Bica et al. (2020), and stars beyond $R_{\rm SMA}$, retained in our catalog, are shown in gray. In the right column, we compare the CSFH obtained after removing sources with $R < R_{\rm SMA}$ (orange) to the CSFH obtained without removing any sources over the entire field of view (blue). The values of τ_{50}, τ_{75}, and τ_{90} are not impacted beyond their uncertainties even if no effort is made to remove the cluster from our photometric catalog.

Appendix B
Simulations

We used a series of simulations to assess the impact of various line-of-sight stellar distance distributions on our recovered CSFHs. Several previous SMC SFH studies have tested the impact of line-of-sight depth on SFH recovery, finding that their results were generally unaffected beyond their uncertainties. However, each of these earlier studies tested only a single analytical form for the stellar distance distribution. P. Massana et al. (2022) tested "Gaussian-like" depths with

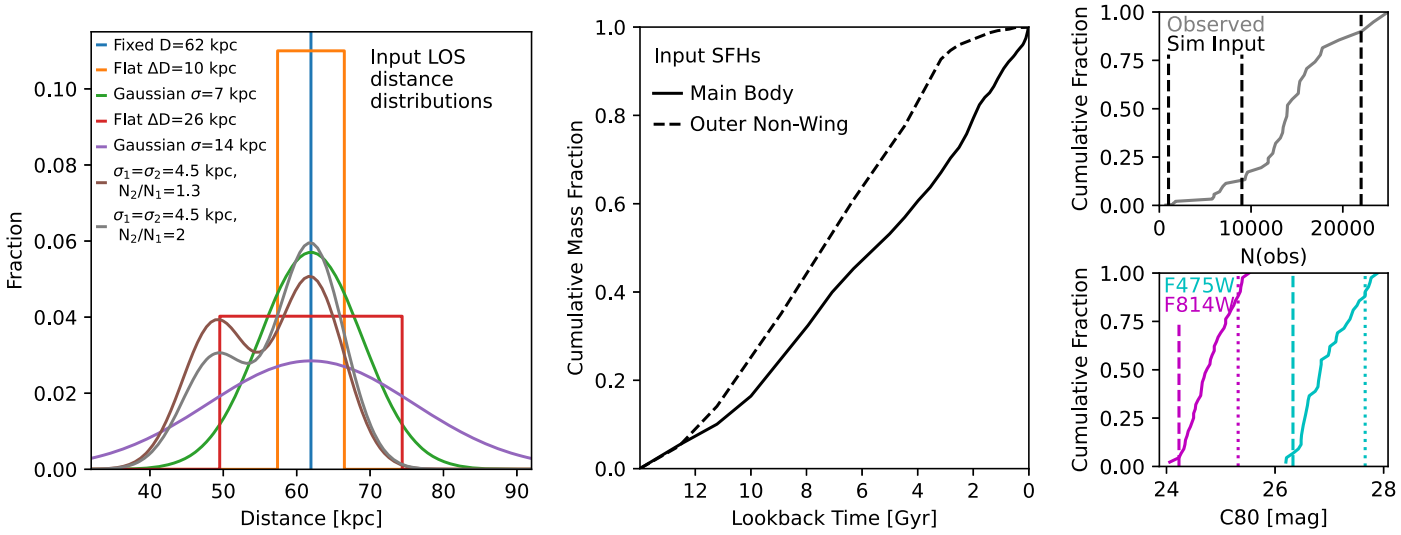

Figure 13. Left: the seven input line-of-sight distance distributions applied to our synthetic CMDs before SFH recovery. Middle: the two input SFHs we used in our simulations, one based on the results of P. Massana et al. (2022) representing the main body of the SMC and another representing our outer SMC fields, which show a drop-off in star formation in the past ∼3 Gyr (Section 4.1). Top right: the three values used in our simulations for the number of observed stars per field, overplotted on the cumulative distribution of the number of stars per field across our sample. Bottom right: cumulative distributions of the 80% completeness limit across our Scylla fields, shown for the F475W filter in cyan and the F814W filter in magenta. Using vertical lines, we overplot the 80% completeness limits in the "deep" (SMC_23; dotted lines) and "shallow" (SMC_35; dashed lines) fields from which we draw our observational noise model based on artificial star tests. The input values we use in our simulations essentially bracket the range of values across our sample of observed fields.

standard deviations up to 5.5 kpc when fitting SMASH photometry, while S. Rubele et al. (2018) tested a Cauchy distribution based on RR Lyrae distances from T. Muraveva et al. (2018) for fitting VMC photometry, and J. Harris & D. Zaritsky (2004) tested a "characteristic depth" of 12 kpc in their fits to MCPS photometry.

There is now a substantial body of observational evidence revealing that the line-of-sight distribution of the SMC's stellar populations is position dependent, in terms of not only its *extent* but also its *shape*. For example, D. L. Nidever et al. (2013, see their Figure 13), using the red clump as a tracer, find distance distributions varying from flat to single-peaked to double-peaked with changing relative amplitudes of the two peaks. Exploiting the contiguous coverage of the VMC survey, S. Subramanian et al. (2017) and D. El Youssoufi et al. (2021) expanded these results by fitting single- and double Gaussians to the red clump distribution along numerous sight lines, finding standard deviations of 3 kpc $\lesssim \sigma \lesssim$ 11 kpc in the inner ∼5° of the SMC, with values as large as $\sigma \sim 16$ kpc in the outer regions. The amplitude ratios of the double-peaked distance distributions are also positionally dependent, with the fainter component being equally or more well populated than the brighter component in the inner ∼3° of the SMC, where our fields lie (S. Subramanian et al. 2017, their Figure 13). In addition to results based on Gaussian fits, B. L. Tatton et al. (2021) use the red clump magnitude distribution from VMC photometry to map the full and interquartile ranges of the line-of-sight depth across the SMC, finding full depths from ∼10 to 26 kpc over the area covered by our fields. Using VMC RR Lyrae stars as a tracer, T. Muraveva et al. (2018) find a line-of-sight depth of ∼9 kpc, in good agreement with results from optical imaging (A. M. Jacyszyn-Dobrzeniecka et al. 2017).

In light of the variety of line-of-sight distance distributions seen across the SMC, we simulate (for the first time as far as we are aware) the impact of multiple analytical forms for the distance distribution of individual stars. These include a single fixed distance as a control sample, as well as flat and Gaussian distance distributions, each with two different widths, based on the above observational evidence. Based on fits by S. Subramanian et al. (2017) and D. El Youssoufi et al. (2021), we also simulate double Gaussians where we have varied the relative amplitude of the two components. We test seven input distance distributions in total, shown using color coding in the left panel of Figure 13:

1. A single, fixed distance.
2. A flat distance distribution of width 10 kpc.
3. A Gaussian distance distribution with a standard deviation $\sigma = 7$ kpc.
4. A broader flat distance distribution of width 26 kpc.
5. A broader Gaussian distance distribution with $\sigma = 14$ kpc.
6. A distance distribution composed of two Gaussians (each with $\sigma = 4.5$ kpc), where the more nearby Gaussian has a mean distance 13 kpc in front of the SMC and has an amplitude 1.3 times smaller than the more distant Gaussian.
7. A double-Gaussian distribution as above, but with the nearer (i.e., foreground) distribution having an amplitude 2 times (rather than 1.3 times) smaller than the farther distribution.

An example of simulated CMDs corresponding to each assumed distance distribution is shown in Figure 14, with color coding corresponding to the distance distributions in the left panel of Figure 13. To isolate the impact of the different distance distributions on the CMD for illustrative purposes, all other input parameters (assumed stellar evolutionary model library, input SFH, observational noise model, and number of stars; see below) were held fixed in Figure 14. The morphology of the red clump, at (F475W–F814W) ∼ 1.4 and F475W ∼ 20.1, is most visibly affected by the various distance distributions, although changes in the widths of other stellar evolutionary sequences, including the subgiant branch and main sequence, are also apparent in some cases.

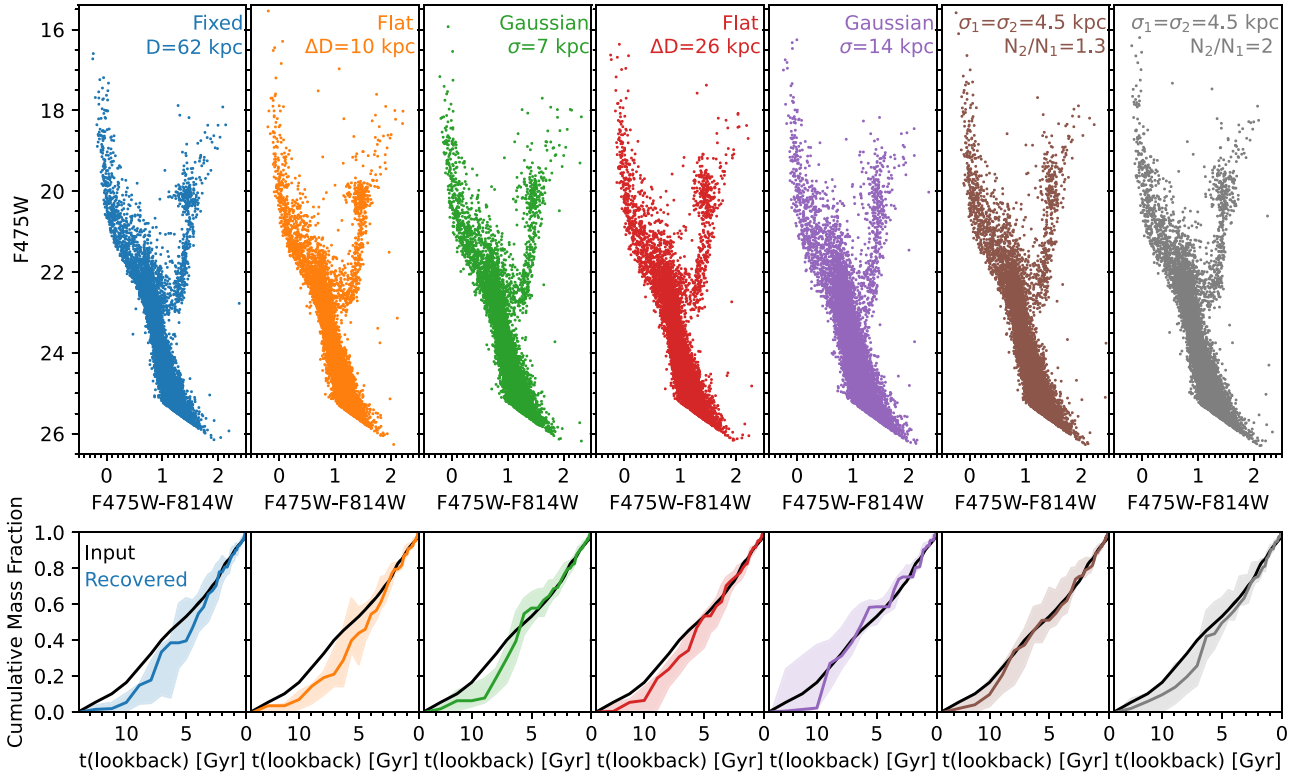

Figure 14. Top row: example synthetic CMDs generated assuming the different line-of-sight stellar distance distributions we sample, color coded and labeled as in the left panel of Figure 13. To allow a direct visual comparison, all synthetic CMDs were generated assuming the same PARSEC evolutionary models, input SFH, observational noise model, and number of observed stars. Bottom row: the recovered SFH for each CMD (assuming PARSEC evolutionary models also for SFH fitting) is overplotted on the input SFH, which is the same "main body" SFH (middle panel of Figure 13) in all cases. While results vary slightly beyond 1σ uncertainties in some cases at early look-back times $\gtrsim$6 Gyr, input values of τ_{50}, τ_{75}, and τ_{90} (sampling more recent look-back times) are recovered to within 1σ uncertainties for all stellar distance distributions.

For each assumed distance distribution, we also varied several additional input parameters, which did not ultimately correlate with the results. These include the following:

Assumed SFH. We tested two input SFHs, shown in the middle panel of Figure 13, one based on the results of P. Massana et al. (2022) corresponding to the main body of the SMC, and another based on our results for the outer fields of the SMC, with a sharp drop-off in star formation in the most recent few gigayears (see Figure 5).

Number of observed stars. To test the impact of sample size on our results, we chose three sample sizes (22K, 9K, and 1K stars, with the last being representative of the fields in the SMC wing). In the top right panel of Figure 13, we overplot these three values on the cumulative distribution of stars per field across our Scylla fields, showing that they reasonably bracket the range of observational sample sizes.

Observational noise model. To simulate an observed field, `MATCH` applies observational noise (photometric error, bias, incompleteness) by drawing from a user-supplied ensemble of artificial star tests. Field-to-field differences in photometric precision and completeness limits can be caused by not only differences in total exposure time but also other effects, including stellar crowding that may vary from field to field. We explored the impact of such differences in photometric precision by supplying artificial stars from each of two fields ("deep" and "shallow") encompassing the range of completeness limits seen across our fields. This is illustrated in the bottom right panel of Figure 13, where we show cumulative distributions of the 80% completeness limits across our fields in each filter and overplot the 80% completeness limits for the "deep" and "shallow" fields using dashed (dotted) lines corresponding to the deep (shallow) field.

Assumed stellar evolutionary model. For each simulation run (i.e., given an assumed input SFH, number of stars, and observational noise model), we use PARSEC evolutionary models to generate synthetic CMDs. We then recover the SFH three times separately, each time assuming a different evolutionary model for SFH fitting (PARSEC, MIST, BaSTI18) identically to our observed fields (see Section 3).

Lastly, we assume fixed input values for both foreground Galactic extinction and differential extinction internal to the SMC when generating synthetic CMDs. Our assumed foreground extinction $A_{V,\mathrm{fg}} = 0.1$ mag is in good agreement with dust emission maps in the outer SMC, where they remain reliable (E. F. Schlafly & D. P. Finkbeiner 2011; see also Figure 14 of D. M. Skowron et al. 2021). Similarly, we assume additional internal differential extinction $\delta A_V = 0.1$ mag, in good agreement with the values from D. M. Skowron et al. (2021). Specifically, they quantified internal differential extinction by fitting half-Gaussians to the CMD distribution of the red clump along the reddening vector, measuring standard deviations σ_1 and σ_2 corresponding to extinction in the near and far sides of the SMC. Averaging their reported σ_1 and σ_2 values across our observed sight lines and converting to V-band extinction using the coefficients of E. F. Schlafly & D. P. Finkbeiner (2011), we find a mean and standard deviation of 0.12 ± 0.04 mag.

The results of our simulations are summarized in Figure 15. The left two panels illustrate our ability to recover τ_{75}, and the

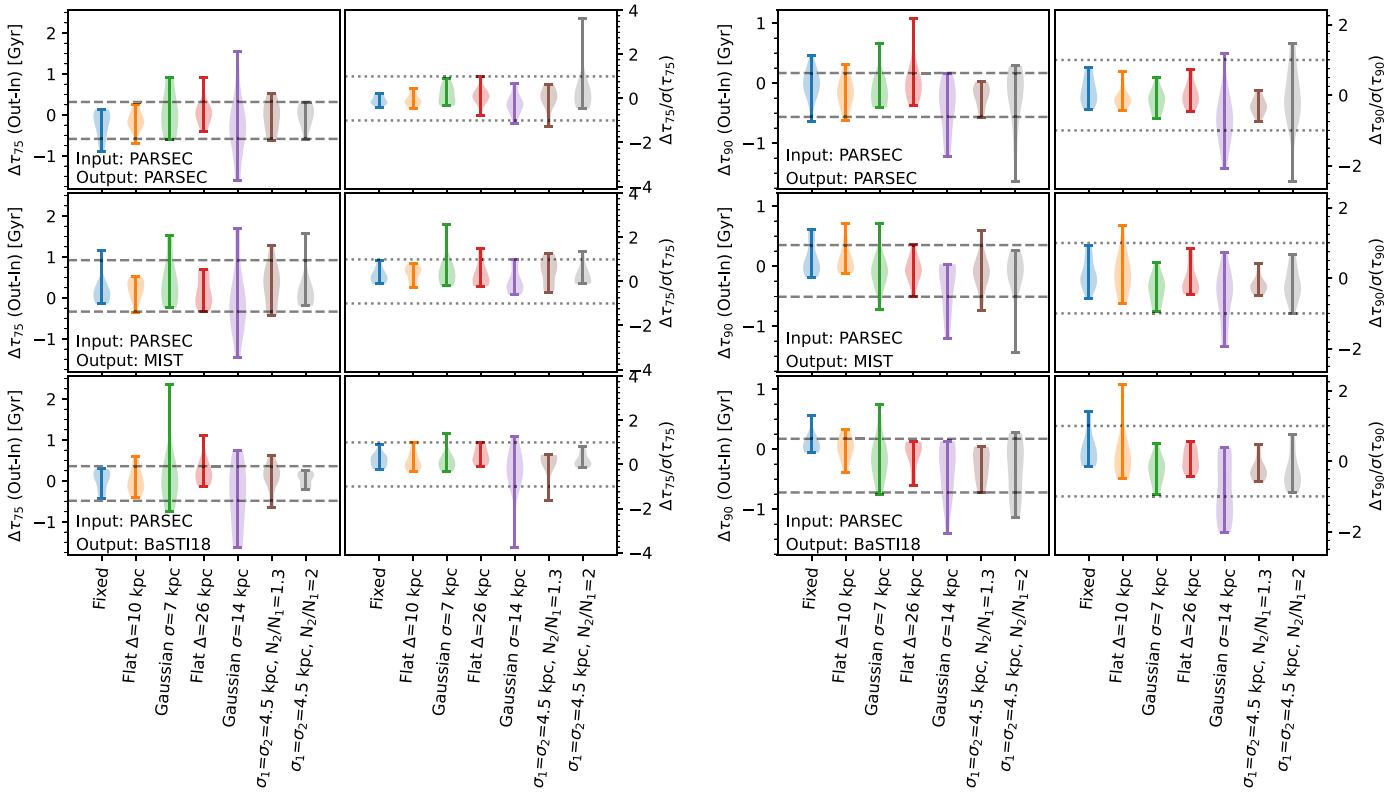

Figure 15. Left: difference between recovered and input values of τ_{75} for input stellar populations with different line-of-sight distance distributions, labeled along the horizontal axis and color coded as in Figures 13 and 14. Synthetic CMDs were generated using PARSEC stellar evolutionary models and then recovered assuming three different assumed stellar evolutionary libraries (one per row), identically to our observational sample. The leftmost column shows the difference between recovered and input values of τ_{75} in Gyr (with the 10th and 90th percentiles over all simulation runs indicated by dashed gray lines), and the second column from the left shows these differences normalized by their 1σ uncertainties (with $\pm1\sigma$ deviations indicated by dotted gray lines). Right columns: same as the left columns, but for τ_{90}.

right two panels illustrate our ability to recover τ_{90}. For each of these two CSFH metrics, the left column illustrates the difference in look-back times in Gyr in the sense (recovered − input). The right column in each panel illustrates the (recovered − input) difference normalized to its 1σ uncertainty, illustrating that the CSFH metrics are nearly always recovered to within their uncertainties, exceeding them in <5% of cases for τ_{90} and τ_{75} (and, although not shown, <10% of cases for τ_{50}). The input CMDs were generated assuming PARSEC evolutionary models, and in each row we assume a different set of assumed stellar evolutionary models for SFH recovery, further illustrating that our results are robust to the choice of stellar evolutionary model used for SFH fitting. Our simulations also demonstrate that the discrepancy between the values of τ_{75} and τ_{90} observed in the wing compared to the radial trend seen for the rest of our fields (see Figure 6) is real, since differences between recovered and input values of τ_{75} and τ_{90} are insufficient to reconcile this discrepancy, even in the presence of a distance spread of as much as 26 kpc or a bimodal distance distribution in the wing (e.g., D. L. Nidever et al. 2013; S. Subramanian et al. 2017; B. L. Tatton et al. 2021).

Appendix C
Results and Comparisons for Individual Fields

In Table 5 we list the best-fit values of τ_{50}, τ_{75}, and τ_{90} and uncertainties for each field assuming three different stellar evolutionary models for SFH fitting. Using these values, we have performed several per-field checks of internal and external consistency in addition to the sample-wide comparisons with literature results in Section 4.3:

1. In Figure 16, we compare our per-field values of τ_{50}, τ_{75}, and τ_{90} across the three different sets of evolutionary models we assumed for SFH fitting, finding that they agree to within 1σ in 97% of cases.
2. We exploit serendipitous imaging of two fields with near-complete (>90%) spatial overlap that were observed with different observing setups. A Scylla field (SMC_5) was observed with WFC3/UVIS F475W and F814W filters, and an archival ACS/WFC field (SMC_A16) was observed with ACS/WFC F606W and F814W filters. The two CSFHs, shown in Figure 17, are in excellent agreement, arguing strongly against any systematic impact of differences in observing setup across our fields. The shallower of the two fields (SMC_5) was excluded from our analysis in order to keep our stellar samples statistically independent.
3. Our results include a reanalysis of the six fields studied by M. Cignoni et al. (2012, 2013), who used two different SFH fitting codes. In Figure 18, we perform a direct comparison between our CSFHs and those obtained by M. Cignoni et al. (2012, 2013) for each field individually, again showing excellent agreement.

Table 5
Look-back Times to Form 50%, 75%, and 90% of Cumulative Stellar Mass for Three Evolutionary Models

Field	PARSEC			MIST			BaSTI18		
	τ_{50} (Gyr)	τ_{75} (Gyr)	τ_{90} (Gyr)	τ_{50} (Gyr)	τ_{75} (Gyr)	τ_{90} (Gyr)	τ_{50} (Gyr)	τ_{75} (Gyr)	τ_{90} (Gyr)
SMC_1	$4.25^{+1.25}_{-0.56}$	$2.38^{+0.84}_{-0.40}$	$0.84^{+0.19}_{-0.26}$	$4.74^{+1.67}_{-0.72}$	$2.25^{+0.99}_{-0.40}$	$0.79^{+0.13}_{-0.13}$	$4.12^{+0.67}_{-0.51}$	$2.12^{+1.43}_{-0.27}$	$0.86^{+0.36}_{-0.26}$
SMC_2	$5.46^{+7.18}_{-0.72}$	$3.24^{+0.31}_{-0.14}$	$1.19^{+0.15}_{-0.25}$	$8.17^{+4.48}_{-2.79}$	$3.00^{+0.89}_{-0.02}$	$1.04^{+0.21}_{-0.08}$	$5.36^{+5.59}_{-0.33}$	$3.24^{+0.56}_{-0.39}$	$1.18^{+0.19}_{-0.30}$
SMC_7	$4.44^{+1.87}_{-0.11}$	$3.54^{+0.65}_{-0.95}$	$2.03^{+0.62}_{-0.72}$	$5.44^{+1.32}_{-1.35}$	$3.61^{+1.56}_{-1.22}$	$1.86^{+0.56}_{-0.27}$	$5.33^{+1.45}_{-0.71}$	$3.32^{+1.40}_{-0.86}$	$1.92^{+0.36}_{-0.21}$
SMC_8	$3.86^{+1.07}_{-0.62}$	$2.06^{+0.51}_{-0.55}$	$0.27^{+0.20}_{-0.09}$	$5.04^{+1.37}_{-0.85}$	$2.28^{+0.82}_{-0.55}$	$0.32^{+0.05}_{-0.11}$	$4.02^{+1.39}_{-0.36}$	$2.15^{+1.24}_{-0.38}$	$0.44^{+0.14}_{-0.14}$
SMC_9	$3.93^{+1.31}_{-0.63}$	$2.21^{+0.46}_{-0.48}$	$0.99^{+0.27}_{-0.17}$	$4.76^{+1.11}_{-1.03}$	$2.18^{+1.42}_{-0.42}$	$0.96^{+0.07}_{-0.06}$	$4.22^{+1.59}_{-0.50}$	$2.29^{+1.38}_{-0.43}$	$1.09^{+0.41}_{-0.23}$
SMC_10	$4.24^{+0.82}_{-0.67}$	$2.16^{+1.23}_{-0.62}$	$0.17^{+0.36}_{-0.00}$	$4.79^{+1.40}_{-0.32}$	$1.92^{+1.83}_{-0.20}$	$0.29^{+0.26}_{-0.07}$	$4.43^{+0.88}_{-0.57}$	$1.98^{+1.66}_{-0.38}$	$0.51^{+0.49}_{-0.24}$
SMC_11	$4.76^{+1.39}_{-0.61}$	$2.34^{+1.99}_{-0.77}$	$0.80^{+0.32}_{-0.29}$	$5.03^{+1.42}_{-0.88}$	$2.81^{+1.47}_{-0.88}$	$0.71^{+0.26}_{-0.26}$	$4.83^{+1.58}_{-0.62}$	$2.35^{+2.24}_{-0.35}$	$0.69^{+0.48}_{-0.18}$
SMC_13	$3.96^{+0.57}_{-0.83}$	$2.25^{+1.03}_{-0.22}$	$0.82^{+0.49}_{-0.29}$	$3.94^{+1.68}_{-0.05}$	$2.48^{+1.39}_{-0.19}$	$0.82^{+0.12}_{-0.08}$	$3.83^{+1.26}_{-0.30}$	$2.26^{+1.03}_{-0.39}$	$0.86^{+0.30}_{-0.24}$
SMC_14	$4.14^{+1.18}_{-0.67}$	$2.53^{+0.74}_{-0.25}$	$1.03^{+0.33}_{-0.17}$	$4.89^{+2.01}_{-1.06}$	$2.25^{+1.83}_{-0.22}$	$0.98^{+0.10}_{-0.11}$	$4.40^{+1.22}_{-0.62}$	$2.61^{+1.13}_{-0.40}$	$1.16^{+0.93}_{-0.39}$
SMC_15	$4.22^{+0.64}_{-0.65}$	$2.52^{+1.25}_{-0.42}$	$1.26^{+0.31}_{-0.14}$	$4.75^{+0.32}_{-1.04}$	$2.48^{+1.82}_{-0.39}$	$1.11^{+0.96}_{-0.06}$	$4.53^{+1.46}_{-0.43}$	$2.47^{+1.74}_{-0.18}$	$1.40^{+0.23}_{-0.08}$
SMC_16	$3.43^{+1.14}_{-0.50}$	$2.11^{+0.70}_{-0.49}$	$0.70^{+0.14}_{-0.08}$	$4.26^{+1.56}_{-0.67}$	$1.94^{+1.50}_{-0.09}$	$0.75^{+0.16}_{-0.05}$	$3.89^{+1.03}_{-0.69}$	$2.18^{+0.53}_{-0.34}$	$0.81^{+0.09}_{-0.20}$
SMC_17	$4.16^{+0.85}_{-0.55}$	$2.12^{+0.51}_{-0.52}$	$0.89^{+0.37}_{-0.08}$	$4.22^{+0.68}_{-0.41}$	$1.90^{+0.99}_{-0.27}$	$0.91^{+0.04}_{-0.20}$	$3.84^{+1.12}_{-0.72}$	$2.09^{+0.45}_{-0.45}$	$0.88^{+0.38}_{-0.23}$
SMC_18	$3.71^{+1.06}_{-0.37}$	$2.10^{+1.16}_{-0.22}$	$0.65^{+0.58}_{-0.17}$	$3.97^{+1.33}_{-1.13}$	$2.30^{+0.44}_{-0.61}$	$0.61^{+0.28}_{-0.20}$	$3.92^{+0.95}_{-1.00}$	$2.22^{+0.63}_{-0.45}$	$0.67^{+0.28}_{-0.18}$
SMC_19	$4.24^{+0.34}_{-1.16}$	$2.27^{+1.14}_{-0.26}$	$0.94^{+0.33}_{-0.38}$	$4.61^{+1.82}_{-0.96}$	$2.59^{+0.93}_{-0.60}$	$0.89^{+0.07}_{-0.24}$	$4.50^{+0.73}_{-0.99}$	$2.14^{+1.46}_{-0.27}$	$1.02^{+0.24}_{-0.38}$
SMC_20	$4.19^{+1.19}_{-1.14}$	$2.04^{+0.71}_{-0.31}$	$0.92^{+0.30}_{-0.35}$	$5.06^{+1.61}_{-1.68}$	$1.92^{+1.16}_{-0.04}$	$0.90^{+0.05}_{-0.24}$	$4.16^{+2.53}_{-0.85}$	$2.01^{+0.99}_{-0.16}$	$0.81^{+0.45}_{-0.27}$
SMC_21	$4.23^{+0.64}_{-1.03}$	$2.09^{+0.80}_{-0.59}$	$0.71^{+0.33}_{-0.14}$	$3.85^{+1.27}_{-0.90}$	$1.82^{+1.03}_{-0.12}$	$0.74^{+0.25}_{-0.24}$	$4.44^{+1.46}_{-0.91}$	$2.12^{+0.96}_{-0.41}$	$0.69^{+0.57}_{-0.15}$
SMC_22	$8.20^{+1.22}_{-2.10}$	$3.95^{+1.69}_{-0.53}$	$1.14^{+0.32}_{-0.17}$	$8.29^{+0.42}_{-2.56}$	$3.69^{+1.28}_{-1.08}$	$1.03^{+0.44}_{-0.19}$	$6.33^{+2.56}_{-1.60}$	$3.53^{+0.85}_{-1.18}$	$1.29^{+0.25}_{-0.53}$
SMC_23	$4.38^{+0.26}_{-0.94}$	$2.17^{+0.17}_{-0.57}$	$0.57^{+0.11}_{-0.18}$	$5.14^{+0.33}_{-1.52}$	$2.06^{+0.75}_{-0.53}$	$0.50^{+0.45}_{-0.16}$	$4.35^{+0.90}_{-0.60}$	$1.91^{+0.26}_{-0.24}$	$0.54^{+0.45}_{-0.05}$
SMC_25	$3.00^{+0.92}_{-0.16}$	$1.62^{+0.35}_{-0.20}$	$0.61^{+0.25}_{-0.01}$	$4.47^{+0.62}_{-1.60}$	$1.82^{+0.37}_{-0.16}$	$0.67^{+0.14}_{-0.05}$	$3.47^{+0.89}_{-0.20}$	$1.82^{+0.35}_{-0.23}$	$0.66^{+0.22}_{-0.06}$
SMC_27	$3.35^{+2.19}_{-0.33}$	$2.05^{+0.79}_{-0.22}$	$0.64^{+0.19}_{-0.03}$	$3.50^{+2.50}_{-0.39}$	$1.97^{+0.86}_{-0.06}$	$0.67^{+0.23}_{-0.03}$	$3.16^{+2.40}_{-0.17}$	$2.03^{+0.40}_{-0.19}$	$0.60^{+0.16}_{-0.02}$
SMC_28	$8.06^{+3.21}_{-2.40}$	$4.12^{+1.12}_{-0.66}$	$1.66^{+0.30}_{-0.64}$	$7.86^{+4.15}_{-2.04}$	$4.58^{+0.83}_{-1.00}$	$1.41^{+0.59}_{-0.30}$	$6.99^{+4.74}_{-1.62}$	$3.36^{+1.63}_{-0.29}$	$1.30^{+0.56}_{-0.23}$
SMC_29	$3.35^{+1.82}_{-0.33}$	$2.06^{+0.28}_{-0.13}$	$0.68^{+0.31}_{-0.07}$	$4.37^{+2.54}_{-0.66}$	$1.83^{+0.79}_{-0.08}$	$0.82^{+0.23}_{-0.24}$	$3.87^{+2.93}_{-0.51}$	$1.89^{+0.55}_{-0.05}$	$0.59^{+0.71}_{-0.04}$
SMC_30	$3.37^{+0.86}_{-0.17}$	$2.04^{+0.46}_{-0.32}$	$0.98^{+0.24}_{-0.26}$	$4.13^{+1.50}_{-0.35}$	$1.82^{+1.55}_{-0.10}$	$0.99^{+0.17}_{-0.06}$	$3.81^{+0.71}_{-0.70}$	$2.04^{+0.82}_{-0.16}$	$1.00^{+0.44}_{-0.27}$
SMC_33	$3.60^{+0.75}_{-0.25}$	$2.38^{+0.41}_{-0.16}$	$0.90^{+0.27}_{-0.12}$	$3.64^{+0.69}_{-1.04}$	$2.04^{+0.48}_{-0.21}$	$0.86^{+0.21}_{-0.23}$	$3.51^{+0.60}_{-0.34}$	$2.16^{+0.24}_{-0.16}$	$0.82^{+0.28}_{-0.14}$
SMC_34	$3.34^{+1.26}_{-0.41}$	$2.13^{+0.47}_{-0.50}$	$0.64^{+0.16}_{-0.03}$	$3.15^{+1.42}_{-0.55}$	$1.97^{+0.29}_{-0.17}$	$0.59^{+0.08}_{-0.04}$	$5.33^{+0.92}_{-2.50}$	$2.12^{+0.19}_{-0.27}$	$0.58^{+0.15}_{-0.03}$
SMC_35	$4.02^{+0.83}_{-0.91}$	$2.62^{+0.61}_{-0.44}$	$1.44^{+0.72}_{-0.52}$	$4.72^{+1.71}_{-0.88}$	$2.27^{+1.44}_{-0.09}$	$1.59^{+0.36}_{-0.61}$	$4.65^{+1.11}_{-1.11}$	$2.49^{+1.06}_{-0.28}$	$1.77^{+0.30}_{-0.83}$
SMC_36	$3.44^{+1.95}_{-0.43}$	$2.02^{+0.38}_{-0.28}$	$0.66^{+0.25}_{-0.09}$	$4.55^{+1.01}_{-1.50}$	$2.00^{+0.34}_{-0.27}$	$0.74^{+0.13}_{-0.22}$	$3.96^{+1.86}_{-0.66}$	$2.11^{+0.50}_{-0.27}$	$0.77^{+0.20}_{-0.22}$
SMC_37	$3.70^{+2.18}_{-0.28}$	$2.14^{+1.16}_{-0.37}$	$0.61^{+0.36}_{-0.01}$	$3.96^{+0.37}_{-1.11}$	$2.01^{+0.43}_{-0.29}$	$0.64^{+0.10}_{-0.09}$	$3.75^{+0.58}_{-0.75}$	$2.27^{+0.41}_{-0.50}$	$0.63^{+0.06}_{-0.13}$
SMC_38	$6.77^{+0.88}_{-1.89}$	$3.23^{+0.53}_{-0.80}$	$0.77^{+0.56}_{-0.15}$	$7.37^{+2.22}_{-2.21}$	$3.26^{+1.20}_{-1.04}$	$0.70^{+0.70}_{-0.05}$	$6.28^{+1.29}_{-2.57}$	$3.18^{+1.35}_{-0.85}$	$0.82^{+0.31}_{-0.26}$
SMC_40	$2.91^{+0.87}_{-0.13}$	$1.80^{+0.32}_{-0.18}$	$0.60^{+0.16}_{-0.00}$	$3.06^{+1.57}_{-0.32}$	$1.64^{+0.51}_{-0.11}$	$0.66^{+0.10}_{-0.06}$	$3.16^{+1.55}_{-0.39}$	$1.76^{+0.54}_{-0.07}$	$0.60^{+0.40}_{-0.03}$
SMC_41	$3.76^{+0.90}_{-0.32}$	$1.38^{+0.32}_{-0.32}$	$0.63^{+0.19}_{-0.03}$	$4.01^{+1.85}_{-0.23}$	$1.54^{+0.37}_{-0.39}$	$0.68^{+0.13}_{-0.04}$	$3.79^{+0.43}_{-0.83}$	$1.59^{+0.22}_{-0.67}$	$0.59^{+0.09}_{-0.02}$
SMC_42	$3.06^{+1.01}_{-0.05}$	$1.91^{+0.76}_{-0.20}$	$0.82^{+0.16}_{-0.12}$	$3.06^{+1.58}_{-0.10}$	$1.83^{+0.33}_{-0.25}$	$0.76^{+0.14}_{-0.09}$	$3.38^{+0.88}_{-0.11}$	$1.94^{+0.47}_{-0.14}$	$0.77^{+0.49}_{-0.09}$
SMC_43	$4.97^{+0.66}_{-0.78}$	$2.48^{+0.47}_{-0.37}$	$0.79^{+0.20}_{-0.17}$	$5.23^{+0.89}_{-0.71}$	$2.40^{+0.89}_{-0.42}$	$0.77^{+0.10}_{-0.17}$	$5.24^{+0.89}_{-1.63}$	$2.37^{+0.65}_{-0.24}$	$0.89^{+0.20}_{-0.28}$
SMC_44	$4.66^{+0.90}_{-1.12}$	$2.60^{+0.53}_{-0.42}$	$0.70^{+0.24}_{-0.04}$	$4.71^{+1.22}_{-1.33}$	$2.31^{+0.86}_{-0.42}$	$0.64^{+0.31}_{-0.05}$	$5.17^{+1.58}_{-1.81}$	$2.40^{+0.63}_{-0.34}$	$0.64^{+0.24}_{-0.04}$
SMC_45	$3.10^{+1.79}_{-0.13}$	$1.78^{+0.17}_{-0.55}$	$0.67^{+0.11}_{-0.01}$	$5.11^{+1.33}_{-2.06}$	$1.81^{+0.35}_{-0.01}$	$0.69^{+0.07}_{-0.07}$	$3.26^{+0.67}_{-0.58}$	$1.54^{+0.44}_{-0.18}$	$0.52^{+0.11}_{-0.01}$
SMC_46	$3.02^{+1.69}_{-0.09}$	$1.86^{+0.66}_{-0.32}$	$0.56^{+0.08}_{-0.13}$	$4.54^{+2.63}_{-0.70}$	$2.10^{+0.64}_{-0.28}$	$0.53^{+0.11}_{-0.10}$	$2.62^{+1.22}_{-0.16}$	$1.56^{+0.52}_{-0.08}$	$0.44^{+0.08}_{-0.06}$
SMC_47	$5.27^{+1.44}_{-1.20}$	$1.76^{+1.54}_{-0.10}$	$0.46^{+0.59}_{-0.06}$	$5.68^{+1.47}_{-1.75}$	$2.05^{+1.65}_{-0.47}$	$0.39^{+0.66}_{-0.03}$	$3.01^{+1.38}_{-0.20}$	$2.02^{+0.24}_{-0.84}$	$0.52^{+0.48}_{-0.23}$
SMC_48	$5.91^{+1.82}_{-1.47}$	$1.92^{+1.93}_{-0.70}$	$0.27^{+0.20}_{-0.05}$	$6.15^{+4.36}_{-1.48}$	$2.24^{+1.21}_{-0.49}$	$0.27^{+0.17}_{-0.06}$	$5.53^{+2.77}_{-2.62}$	$1.60^{+0.81}_{-0.16}$	$0.12^{+0.25}_{-0.00}$
SMC_49	$3.34^{+1.51}_{-0.16}$	$2.04^{+1.16}_{-0.17}$	$0.95^{+0.40}_{-0.28}$	$4.18^{+1.94}_{-0.85}$	$2.01^{+0.67}_{-0.01}$	$1.05^{+0.13}_{-0.18}$	$2.99^{+0.96}_{-0.44}$	$1.74^{+0.68}_{-0.06}$	$0.55^{+0.79}_{-0.03}$
SMC_52	$5.11^{+1.27}_{-1.80}$	$1.41^{+1.80}_{-0.29}$	$0.26^{+0.42}_{-0.03}$	$4.27^{+2.30}_{-1.17}$	$2.02^{+1.21}_{-0.90}$	$0.24^{+0.42}_{-0.02}$	$4.59^{+0.93}_{-1.46}$	$1.55^{+1.23}_{-0.75}$	$0.21^{+0.48}_{-0.01}$
SMC_53	$4.21^{+3.01}_{-1.07}$	$2.15^{+1.40}_{-0.06}$	$0.66^{+0.34}_{-0.02}$	$4.31^{+1.84}_{-0.41}$	$2.16^{+1.50}_{-0.07}$	$0.67^{+0.18}_{-0.06}$	$3.50^{+4.14}_{-0.29}$	$1.91^{+0.71}_{-0.06}$	$0.49^{+0.40}_{-0.00}$
SMC_54	$2.85^{+0.57}_{-0.24}$	$1.85^{+0.33}_{-0.57}$	$0.70^{+0.09}_{-0.07}$	$3.43^{+0.93}_{-0.64}$	$1.73^{+0.52}_{-0.10}$	$0.71^{+0.21}_{-0.08}$	$2.76^{+0.68}_{-0.27}$	$1.77^{+0.42}_{-0.29}$	$0.54^{+0.19}_{-0.08}$
SMC_55	$2.84^{+1.91}_{-0.03}$	$2.03^{+0.82}_{-0.25}$	$0.84^{+0.30}_{-0.11}$	$4.36^{+2.17}_{-1.00}$	$2.17^{+0.61}_{-0.23}$	$0.93^{+0.77}_{-0.11}$	$2.64^{+2.37}_{-0.17}$	$1.86^{+0.64}_{-0.08}$	$0.65^{+0.31}_{-0.15}$
SMC_W1	$4.18^{+0.75}_{-0.76}$	$2.04^{+0.51}_{-0.64}$	$0.83^{+0.45}_{-0.15}$	$5.09^{+0.35}_{-1.33}$	$1.86^{+1.30}_{-0.25}$	$0.90^{+0.14}_{-0.17}$	$3.66^{+0.89}_{-0.64}$	$1.93^{+1.08}_{-0.22}$	$0.70^{+0.48}_{-0.09}$
SMC_W2	$4.99^{+1.71}_{-0.09}$	$4.52^{+1.31}_{-0.93}$	$3.23^{+2.09}_{-0.94}$	$8.33^{+1.51}_{-2.08}$	$6.49^{+2.03}_{-1.52}$	$3.44^{+3.94}_{-0.60}$	$5.59^{+2.10}_{-1.14}$	$4.49^{+1.84}_{-1.84}$	$3.65^{+1.41}_{-1.40}$
SMC_W3	$6.47^{+0.55}_{-1.49}$	$4.76^{+1.49}_{-0.80}$	$3.56^{+1.67}_{-1.43}$	$8.49^{+0.25}_{-2.24}$	$5.70^{+1.95}_{-1.05}$	$4.46^{+1.61}_{-2.32}$	$7.33^{+0.63}_{-1.56}$	$5.24^{+1.16}_{-1.29}$	$3.03^{+2.86}_{-0.56}$
SMC_W4	$8.46^{+1.14}_{-1.51}$	$7.96^{+0.15}_{-3.29}$	$3.82^{+1.18}_{-0.69}$	$8.49^{+0.17}_{-2.07}$	$5.45^{+1.57}_{-1.22}$	$3.34^{+2.61}_{-0.72}$	$7.76^{+1.76}_{-1.34}$	$4.66^{+3.39}_{-0.86}$	$3.35^{+3.00}_{-0.96}$
SMC_W5	$4.89^{+1.71}_{-0.20}$	$3.14^{+2.30}_{-0.22}$	$2.81^{+0.86}_{-0.51}$	$7.92^{+0.29}_{-2.58}$	$3.10^{+3.53}_{-0.32}$	$2.62^{+2.92}_{-0.30}$	$7.84^{+0.88}_{-1.51}$	$4.09^{+2.72}_{-0.44}$	$3.30^{+2.72}_{-0.49}$
SMC_W6	$4.18^{+0.60}_{-0.78}$	$2.32^{+0.36}_{-0.40}$	$0.83^{+0.13}_{-0.12}$	$5.04^{+0.66}_{-1.09}$	$2.17^{+1.40}_{-0.31}$	$0.81^{+0.16}_{-0.05}$	$3.95^{+2.10}_{-0.21}$	$2.08^{+1.43}_{-0.26}$	$0.80^{+0.13}_{-0.07}$
SMC_W7	$3.64^{+0.25}_{-0.57}$	$2.16^{+0.27}_{-0.27}$	$0.62^{+0.28}_{-0.03}$	$4.35^{+0.44}_{-0.64}$	$2.85^{+0.57}_{-1.07}$	$0.69^{+0.21}_{-0.13}$	$3.65^{+1.05}_{-0.26}$	$1.91^{+0.80}_{-0.18}$	$0.65^{+0.23}_{-0.11}$
SMC_A1	$4.52^{+0.37}_{-0.76}$	$2.79^{+0.80}_{-0.16}$	$1.48^{+0.27}_{-0.34}$	$5.13^{+0.86}_{-0.90}$	$3.29^{+0.95}_{-0.60}$	$1.23^{+0.24}_{-0.18}$	$4.44^{+0.98}_{-0.37}$	$2.98^{+1.20}_{-0.50}$	$1.48^{+0.33}_{-0.14}$
SMC_A2	$4.12^{+0.65}_{-0.81}$	$2.25^{+0.16}_{-0.45}$	$0.82^{+0.28}_{-0.26}$	$4.39^{+0.79}_{-0.47}$	$2.48^{+0.25}_{-0.65}$	$0.81^{+0.07}_{-0.27}$	$4.20^{+1.00}_{-0.71}$	$2.03^{+0.67}_{-0.25}$	$0.81^{+0.25}_{-0.31}$
SMC_A3	$3.86^{+0.50}_{-0.42}$	$2.55^{+0.82}_{-0.37}$	$0.89^{+0.31}_{-0.03}$	$4.64^{+0.81}_{-0.69}$	$3.02^{+0.89}_{-0.78}$	$0.92^{+0.23}_{-0.10}$	$3.96^{+0.64}_{-0.88}$	$2.22^{+1.16}_{-0.37}$	$0.97^{+0.13}_{-0.30}$
SMC_A4	$2.66^{+0.32}_{-0.11}$	$1.15^{+0.10}_{-0.29}$	$0.26^{+0.19}_{-0.01}$	$3.82^{+0.39}_{-0.76}$	$1.00^{+0.27}_{-0.23}$	$0.26^{+0.15}_{-0.01}$	$3.22^{+0.49}_{-1.06}$	$1.09^{+0.24}_{-0.32}$	$0.27^{+0.14}_{-0.02}$
SMC_A5	$4.07^{+0.86}_{-0.53}$	$2.45^{+1.24}_{-0.50}$	$1.08^{+0.32}_{-0.30}$	$4.51^{+0.73}_{-1.07}$	$2.22^{+1.17}_{-0.47}$	$0.87^{+0.11}_{-0.15}$	$4.59^{+0.36}_{-1.50}$	$2.28^{+1.36}_{-0.45}$	$1.04^{+0.38}_{-0.40}$
SMC_A6	$4.02^{+0.54}_{-0.87}$	$2.31^{+0.27}_{-0.35}$	$1.13^{+0.35}_{-0.21}$	$4.54^{+0.42}_{-0.93}$	$2.61^{+1.21}_{-0.75}$	$0.94^{+0.20}_{-0.09}$	$3.77^{+1.12}_{-0.41}$	$2.13^{+1.50}_{-0.20}$	$1.01^{+0.39}_{-0.19}$

Table 5
(Continued)

Field	PARSEC			MIST			BaSTI18		
	τ_{50} (Gyr)	τ_{75} (Gyr)	τ_{90} (Gyr)	τ_{50} (Gyr)	τ_{75} (Gyr)	τ_{90} (Gyr)	τ_{50} (Gyr)	τ_{75} (Gyr)	τ_{90} (Gyr)
SMC_A7	$3.79^{+0.56}_{-0.98}$	$2.22^{+0.39}_{-0.55}$	$0.82^{+0.39}_{-0.14}$	$4.58^{+0.28}_{-1.31}$	$2.01^{+1.38}_{-0.39}$	$0.84^{+0.10}_{-0.22}$	$3.80^{+0.85}_{-0.68}$	$2.02^{+1.42}_{-0.65}$	$0.72^{+0.57}_{-0.15}$
SMC_A8	$6.06^{+0.93}_{-1.14}$	$4.16^{+1.73}_{-0.48}$	$3.24^{+1.81}_{-0.27}$	$6.85^{+1.22}_{-0.66}$	$4.74^{+2.53}_{-0.38}$	$3.46^{+2.69}_{-0.22}$	$6.98^{+1.77}_{-1.19}$	$4.43^{+2.25}_{-0.94}$	$3.31^{+2.13}_{-0.68}$
SMC_A9	$5.19^{+0.99}_{-0.90}$	$4.00^{+0.78}_{-0.92}$	$1.90^{+1.02}_{-0.85}$	$6.74^{+1.58}_{-1.41}$	$4.37^{+1.36}_{-0.89}$	$1.61^{+1.41}_{-0.31}$	$5.99^{+1.84}_{-1.67}$	$3.61^{+0.81}_{-0.71}$	$1.75^{+1.15}_{-0.78}$
SMC_A10	$4.28^{+0.30}_{-1.23}$	$2.15^{+0.10}_{-0.30}$	$0.66^{+0.16}_{-0.23}$	$4.91^{+0.42}_{-0.92}$	$2.60^{+0.70}_{-0.92}$	$0.78^{+0.12}_{-0.18}$	$4.60^{+0.54}_{-1.06}$	$1.91^{+0.24}_{-0.15}$	$0.73^{+0.13}_{-0.13}$
SMC_A11	$4.60^{+0.21}_{-0.89}$	$2.28^{+0.09}_{-0.42}$	$0.56^{+0.21}_{-0.08}$	$5.14^{+0.21}_{-0.95}$	$2.41^{+0.14}_{-0.79}$	$0.54^{+0.45}_{-0.06}$	$4.53^{+0.22}_{-0.93}$	$1.91^{+0.25}_{-0.19}$	$0.59^{+0.58}_{-0.09}$
SMC_A12	$4.42^{+1.56}_{-0.51}$	$2.57^{+1.04}_{-0.47}$	$0.59^{+0.35}_{-0.00}$	$4.18^{+2.16}_{-0.26}$	$2.83^{+0.77}_{-0.79}$	$0.79^{+0.05}_{-0.22}$	$4.96^{+1.26}_{-1.06}$	$2.32^{+1.24}_{-0.23}$	$0.64^{+0.24}_{-0.08}$
SMC_A13	$4.52^{+0.30}_{-1.17}$	$2.64^{+0.70}_{-0.52}$	$1.14^{+0.49}_{-0.24}$	$5.03^{+0.46}_{-1.40}$	$2.96^{+0.84}_{-0.72}$	$1.01^{+0.19}_{-0.08}$	$4.64^{+0.37}_{-1.40}$	$2.72^{+0.62}_{-0.51}$	$1.28^{+0.26}_{-0.35}$
SMC_A14	$4.54^{+0.12}_{-1.09}$	$2.33^{+0.38}_{-0.34}$	$1.03^{+0.26}_{-0.31}$	$5.04^{+0.20}_{-1.28}$	$2.46^{+0.61}_{-0.65}$	$0.88^{+0.13}_{-0.09}$	$5.02^{+0.13}_{-1.40}$	$2.17^{+1.42}_{-0.12}$	$1.09^{+0.35}_{-0.28}$
SMC_A15	$4.12^{+0.41}_{-0.95}$	$2.52^{+0.42}_{-0.55}$	$0.90^{+0.33}_{-0.28}$	$5.07^{+0.27}_{-1.38}$	$2.86^{+0.88}_{-0.78}$	$0.99^{+0.08}_{-0.24}$	$4.59^{+0.17}_{-1.30}$	$2.34^{+0.89}_{-0.30}$	$1.04^{+0.37}_{-0.49}$
SMC_A16	$4.12^{+0.39}_{-0.55}$	$2.27^{+1.27}_{-0.21}$	$0.60^{+0.54}_{-0.08}$	$4.93^{+0.62}_{-0.83}$	$2.14^{+1.42}_{-0.28}$	$0.63^{+0.22}_{-0.10}$	$5.15^{+0.34}_{-1.44}$	$1.98^{+1.61}_{-0.13}$	$0.60^{+0.37}_{-0.06}$
SMC_A17	$4.16^{+0.58}_{-0.82}$	$2.89^{+0.41}_{-0.44}$	$1.51^{+0.24}_{-0.17}$	$5.26^{+0.51}_{-1.41}$	$3.10^{+1.03}_{-0.83}$	$1.24^{+0.88}_{-0.03}$	$5.50^{+0.01}_{-1.96}$	$2.86^{+0.67}_{-0.31}$	$1.54^{+0.19}_{-0.10}$
SMC_A18	$4.80^{+0.87}_{-0.44}$	$2.47^{+0.51}_{-0.30}$	$0.66^{+0.23}_{-0.30}$	$5.41^{+1.88}_{-0.57}$	$2.51^{+1.09}_{-0.56}$	$0.55^{+0.35}_{-0.20}$	$4.82^{+1.42}_{-0.80}$	$2.15^{+0.73}_{-0.09}$	$0.60^{+0.15}_{-0.16}$
SMC_A19	$4.75^{+1.42}_{-0.52}$	$3.34^{+1.78}_{-0.28}$	$1.38^{+0.72}_{-0.28}$	$5.90^{+0.54}_{-1.72}$	$4.17^{+0.52}_{-1.34}$	$1.48^{+0.59}_{-0.33}$	$4.98^{+0.59}_{-1.32}$	$3.59^{+0.53}_{-1.09}$	$1.52^{+0.34}_{-0.65}$
SMC_A20	$4.11^{+0.49}_{-0.68}$	$2.58^{+0.83}_{-0.20}$	$1.43^{+0.39}_{-0.26}$	$4.68^{+0.57}_{-0.67}$	$2.22^{+1.48}_{-0.07}$	$1.11^{+0.57}_{-0.01}$	$4.97^{+1.01}_{-0.84}$	$2.57^{+1.23}_{-0.03}$	$1.39^{+0.41}_{-0.02}$
SMC_A21	$4.88^{+0.25}_{-1.54}$	$2.37^{+0.96}_{-0.15}$	$0.90^{+0.40}_{-0.39}$	$5.66^{+0.01}_{-1.84}$	$2.10^{+1.75}_{-0.16}$	$1.02^{+0.05}_{-0.49}$	$4.57^{+1.70}_{-0.92}$	$2.20^{+1.56}_{-0.15}$	$1.26^{+0.21}_{-0.72}$
SMC_A22	$5.14^{+0.48}_{-1.00}$	$3.26^{+0.73}_{-0.38}$	$1.57^{+0.51}_{-0.10}$	$5.34^{+0.86}_{-0.58}$	$3.26^{+1.91}_{-0.31}$	$1.38^{+1.12}_{-0.10}$	$4.62^{+0.99}_{-0.93}$	$3.12^{+0.70}_{-0.39}$	$1.56^{+0.29}_{-0.14}$
SMC_A23	$5.84^{+0.90}_{-0.80}$	$3.78^{+1.43}_{-0.31}$	$1.91^{+1.63}_{-0.31}$	$5.68^{+1.59}_{-0.64}$	$3.67^{+2.10}_{-0.56}$	$1.69^{+1.32}_{-0.27}$	$6.26^{+2.01}_{-0.54}$	$3.44^{+2.89}_{-0.22}$	$1.70^{+1.97}_{-0.11}$
SMC_A24	$5.15^{+0.20}_{-1.16}$	$2.78^{+0.68}_{-0.29}$	$1.18^{+0.51}_{-0.35}$	$6.58^{+1.52}_{-1.50}$	$3.13^{+1.60}_{-0.21}$	$1.06^{+0.77}_{-0.20}$	$6.68^{+1.46}_{-2.26}$	$3.16^{+1.27}_{-0.47}$	$1.41^{+0.45}_{-0.43}$
SMC_A25	$4.83^{+1.15}_{-0.64}$	$3.82^{+0.57}_{-0.71}$	$2.37^{+0.88}_{-0.44}$	$5.35^{+1.61}_{-1.06}$	$3.05^{+2.14}_{-0.48}$	$2.25^{+1.26}_{-0.52}$	$5.90^{+0.63}_{-2.12}$	$3.06^{+0.81}_{-0.30}$	$2.02^{+0.63}_{-0.22}$
SMC_A26	$3.44^{+0.76}_{-0.02}$	$1.90^{+0.35}_{-0.12}$	$0.73^{+0.21}_{-0.09}$	$4.18^{+0.70}_{-0.61}$	$1.99^{+0.64}_{-0.38}$	$0.67^{+0.17}_{-0.01}$	$3.77^{+0.75}_{-0.06}$	$1.83^{+0.18}_{-0.19}$	$0.73^{+0.21}_{-0.04}$
SMC_A27	$4.64^{+0.90}_{-1.49}$	$2.61^{+0.53}_{-0.35}$	$1.79^{+0.54}_{-0.39}$	$5.08^{+1.90}_{-1.19}$	$2.48^{+0.67}_{-0.50}$	$1.78^{+0.12}_{-0.31}$	$6.21^{+2.48}_{-2.39}$	$2.72^{+1.16}_{-0.43}$	$1.87^{+0.31}_{-0.25}$
SMC_A28	$5.80^{+0.21}_{-1.38}$	$3.29^{+0.50}_{-0.84}$	$1.34^{+0.12}_{-0.44}$	$7.14^{+0.68}_{-2.35}$	$3.20^{+1.30}_{-0.99}$	$1.09^{+0.38}_{-0.16}$	$6.35^{+2.00}_{-1.92}$	$3.18^{+1.15}_{-0.63}$	$1.32^{+0.24}_{-0.36}$
SMC_A29	$5.35^{+1.42}_{-0.94}$	$4.47^{+0.03}_{-1.51}$	$1.33^{+0.36}_{-0.50}$	$6.43^{+0.76}_{-1.73}$	$3.02^{+2.06}_{-0.36}$	$1.09^{+0.74}_{-0.13}$	$7.98^{+0.81}_{-3.04}$	$3.00^{+2.52}_{-0.08}$	$1.21^{+0.38}_{-0.17}$
SMC_A30	$7.26^{+0.21}_{-1.62}$	$4.83^{+1.23}_{-0.42}$	$3.66^{+2.03}_{-0.45}$	$8.72^{+0.07}_{-2.44}$	$4.81^{+2.42}_{-0.31}$	$3.83^{+2.64}_{-0.63}$	$8.11^{+1.56}_{-1.37}$	$4.78^{+3.02}_{-0.31}$	$3.74^{+2.17}_{-0.49}$
SMC_A31	$8.58^{+0.32}_{-2.23}$	$5.80^{+1.69}_{-0.83}$	$3.89^{+2.06}_{-0.64}$	$9.62^{+1.24}_{-1.53}$	$6.24^{+2.21}_{-0.75}$	$3.66^{+2.75}_{-0.39}$	$8.55^{+1.27}_{-1.23}$	$5.62^{+2.14}_{-0.41}$	$3.68^{+2.09}_{-0.61}$
SMC_A32	$11.4^{+0.74}_{-5.24}$	$4.60^{+1.62}_{-1.04}$	$2.96^{+1.03}_{-0.52}$	$12.2^{+0.64}_{-6.17}$	$4.56^{+2.23}_{-1.13}$	$3.32^{+0.91}_{-0.92}$	$12.7^{+0.06}_{-6.57}$	$4.70^{+2.09}_{-1.05}$	$3.01^{+0.90}_{-0.50}$
SMC_A33	$12.7^{+0.02}_{-4.24}$	$4.60^{+2.16}_{-0.64}$	$3.05^{+1.39}_{-0.28}$	$12.6^{+0.04}_{-4.41}$	$4.31^{+2.73}_{-0.14}$	$2.80^{+2.19}_{-0.22}$	$12.6^{+0.18}_{-3.69}$	$4.91^{+1.24}_{-1.03}$	$2.76^{+1.44}_{-0.36}$

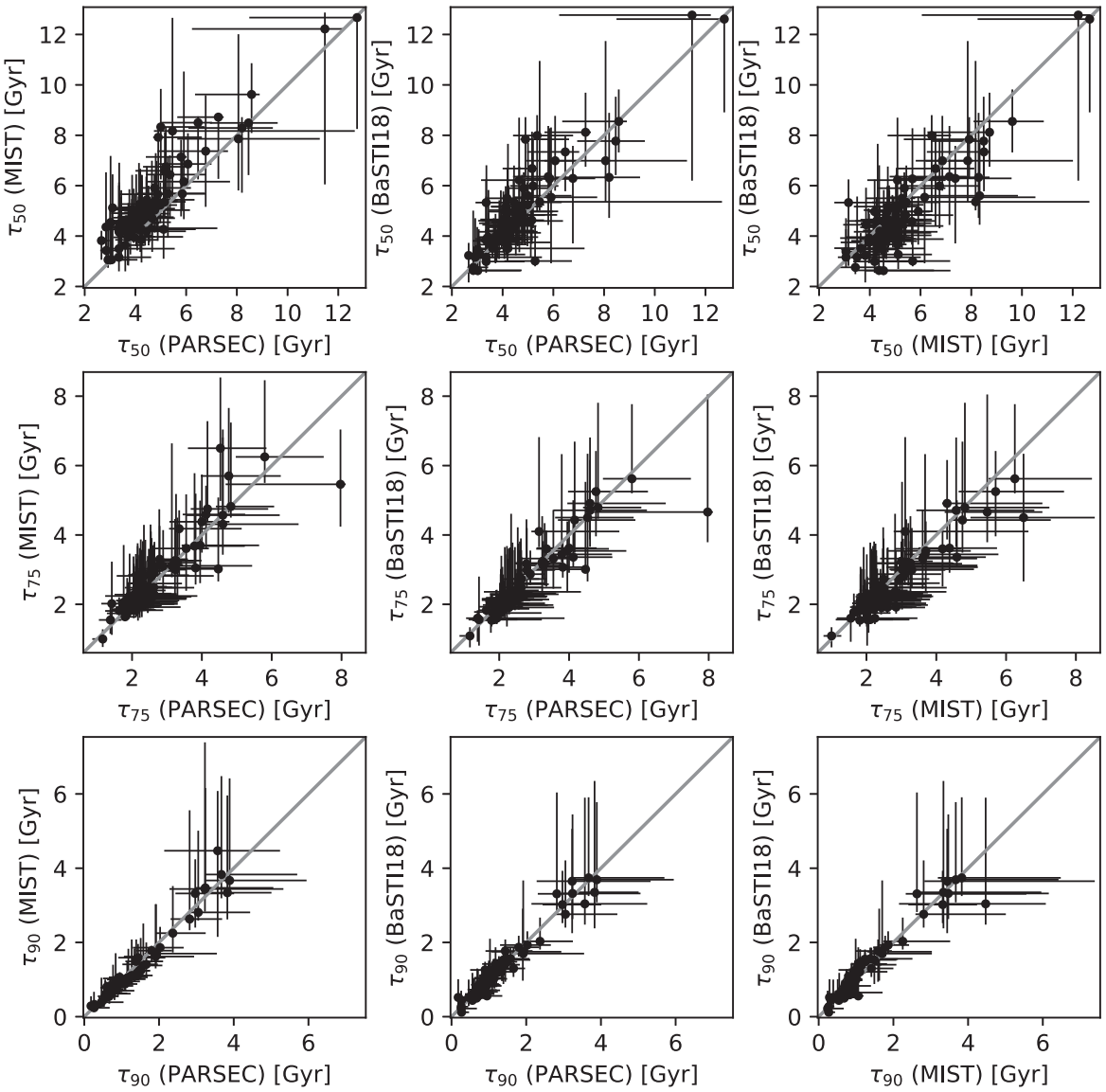

Figure 16. Comparison of our best-fit values for τ_{50} (top row), τ_{75} (middle row), and τ_{90} (bottom row) assuming different stellar evolutionary models for SFH fitting. Results are in agreement across different evolutionary models in nearly all (>97%) cases.

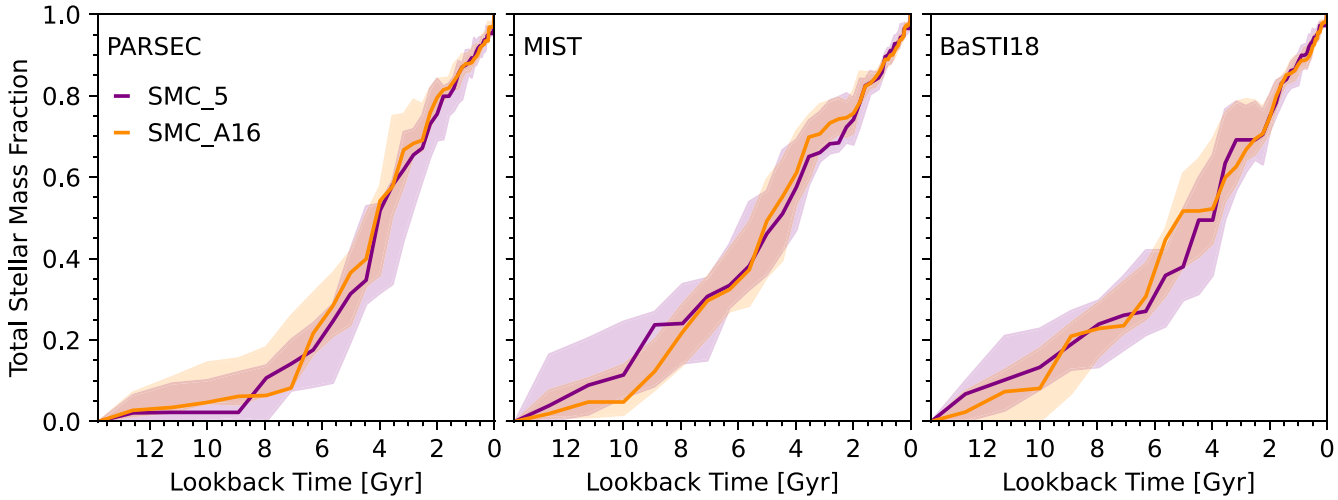

Figure 17. Comparison between CSFHs for two cospatial fields observed with different instrument and filter combinations: SMC_5 was observed with WFC3/UVIS F475W and F814W filters, and SMC_A16 was observed with ACS/WFC F606W and F814W filters. Each panel presents a comparison assuming a different stellar evolutionary library for SFH fitting. The best-fit CSFHs are in excellent agreement, showing no evidence of observational systematics.

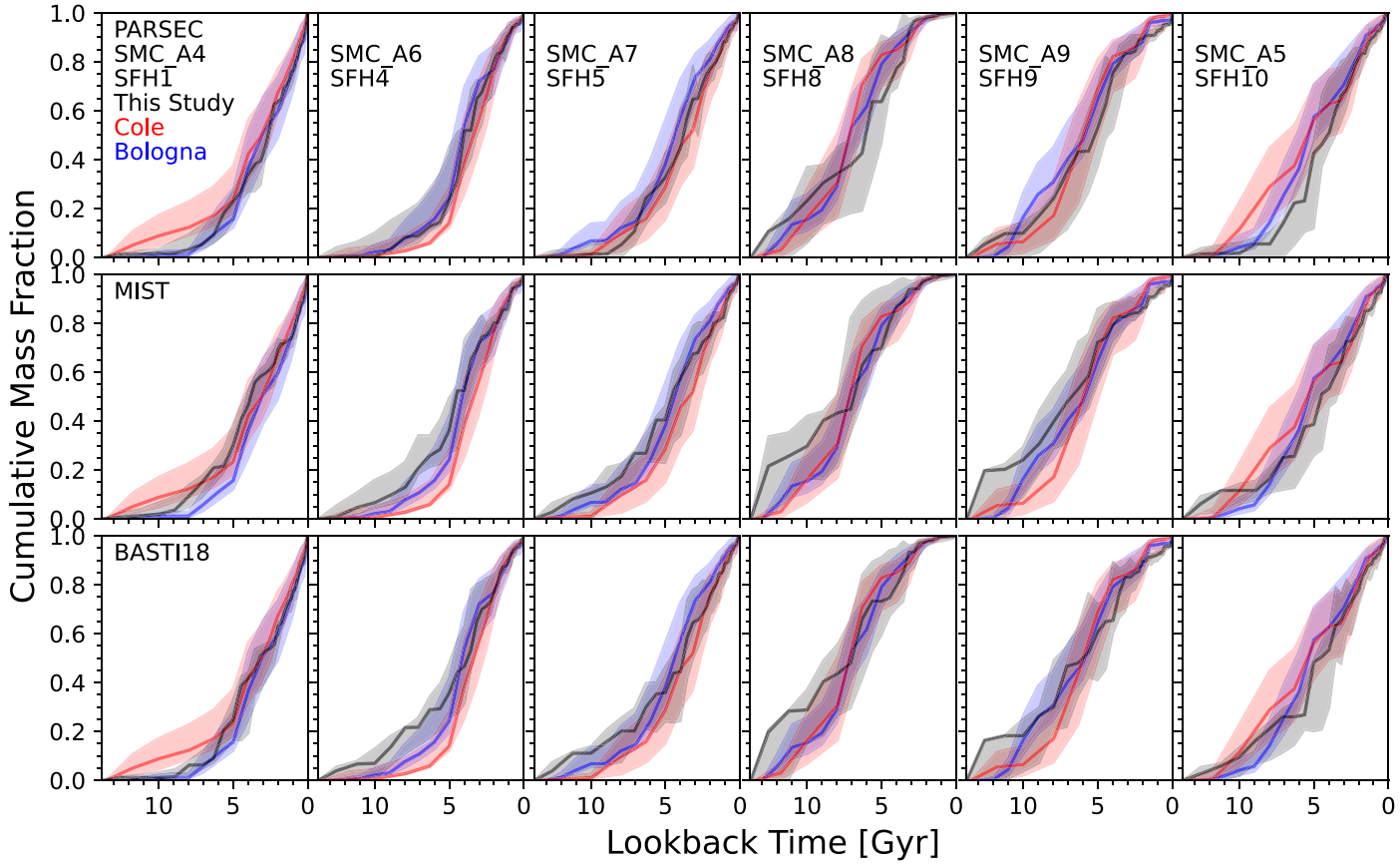

Figure 18. Per-field comparison between our CSFHs from MATCH (black) and those of M. Cignoni et al. (2012, 2013), who used both the Cole (red) and Bologna (blue) SFH fitting codes and then-recent Padova evolutionary models (G. Bertelli et al. 2008, 2009). Each row shows results for all six fields assuming a different set of evolutionary models for our SFH fitting. Each column is labeled with the corresponding field name used here, as well as the field name used by M. Cignoni et al. (2013).

ORCID iDs

Roger E. Cohen https://orcid.org/0000-0002-2970-7435
Kristen B. W. McQuinn https://orcid.org/0000-0001-5538-2614
Claire E. Murray https://orcid.org/0000-0002-7743-8129
Benjamin F. Williams https://orcid.org/0000-0002-7502-0597
Yumi Choi https://orcid.org/0000-0003-1680-1884
Christina W. Lindberg https://orcid.org/0000-0003-0588-7360
Clare Burhenne https://orcid.org/0009-0005-0339-015X
Karl D. Gordon https://orcid.org/0000-0001-5340-6774
Caroline Bot https://orcid.org/0000-0001-6118-2985
Andrew E. Dolphin https://orcid.org/0000-0001-8416-4093
Karoline M. Gilbert https://orcid.org/0000-0003-0394-8377
Steven Goldman https://orcid.org/0000-0002-8937-3844
Alec S. Hirschauer https://orcid.org/0000-0002-2954-8622
Karin M. Sandstrom https://orcid.org/0000-0002-4378-8534
O. Grace Telford https://orcid.org/0000-0003-4122-7749

References

Abdollahi, H., Javadi, A., Mirtorabi, M. T., et al. 2023, ApJ, 948, 63
Albers, S. M., Weisz, D. R., Cole, A. A., et al. 2019, MNRAS, 490, 5538
Almeida, A., Anderson, S. F., Argudo-Fernández, M., et al. 2023, ApJS, 267, 44
Almeida, A., Majewski, S. R., Nidever, D. L., et al. 2024, MNRAS, 529, 3858
Annibali, F., Nipoti, C., Ciotti, L., et al. 2016, ApJL, 826, L27
Annibali, F., & Tosi, M. 2022, NatAs, 6, 48
Astropy Collaboration, Price-Whelan, A. M., Lim, P. L., et al. 2022, ApJ, 935, 167
Avila, R. J., Hack, W., Cara, M., et al. 2015, in ASP Conf. Ser. 495, Astronomical Data Analysis Software and Systems XXIV, ed. A. R. Taylor & E. Rosolowsky (San Francisco, CA: ASP), 281
Beccari, G., Bellazzini, M., Fraternali, F., et al. 2014, A&A, 570, A78
Belokurov, V. A., & Erkal, D. 2019, MNRAS, 482, L9
Bertelli, G., Girardi, L., Marigo, P., et al. 2008, A&A, 484, 815
Bertelli, G., Nasi, E., Girardi, L., et al. 2009, A&A, 508, 355
Besla, G., Kallivayalil, N., Hernquist, L., et al. 2007, ApJ, 668, 949
Besla, G., Kallivayalil, N., Hernquist, L., et al. 2012, MNRAS, 421, 2109
Bettinelli, M., Hidalgo, S. L., Cassisi, S., et al. 2019, MNRAS, 487, 5862
Bica, E., Westera, P., Kerber, L. D. O., et al. 2020, AJ, 159, 82
Bitsakis, T., González-López lira, R. A., Bonfini, P., et al. 2018, ApJ, 853, 104
Bressan, A., Marigo, P., Girardi, L., et al. 2012, MNRAS, 427, 127
Cannon, J. M., O'Leary, E. M., Weisz, D. R., et al. 2012, ApJ, 747, 122
Carballo-Bello, J. A. 2019, MNRAS, 486, 1667
Carnall, A. C., Leja, J., Johnson, B. D., et al. 2019, ApJ, 873, 44
Carr, C., Johnston, K. V., Laporte, C. F. P., et al. 2022, MNRAS, 516, 5067
Carrera, R., Gallart, C., Aparicio, A., et al. 2008, AJ, 136, 1039
Chandra, V., Naidu, R. P., Conroy, C., et al. 2023, ApJ, 956, 110
Chiosi, E., & Vallenari, A. 2007, A&A, 466, 165
Choi, J., Dotter, A., Conroy, C., et al. 2016, ApJ, 823, 102
Choi, Y., Nidever, D. L., Olsen, K., et al. 2018a, ApJ, 866, 90
Choi, Y., Nidever, D. L., Olsen, K., et al. 2018b, ApJ, 869, 125
Choi, Y., Olsen, K. A. G., Besla, G., et al. 2022, ApJ, 927, 153
Choudhury, S., de Grijs, R., Rubele, S., et al. 2020, MNRAS, 497, 3746
Cignoni, M., Cole, A. A., Tosi, M., et al. 2012, ApJ, 754, 130
Cignoni, M., Cole, A. A., Tosi, M., et al. 2013, ApJ, 775, 83
Cioni, M.-R. L., Clementini, G., Girardi, L., et al. 2011, A&A, 527, A116
Cioni, M.-R. L., Storm, J., Bell, C. P. M., et al. 2019, Msngr, 175, 54
Cohen, R. E., McQuinn, K. B. W., Murray, C. E., et al. 2024, ApJ, 975, 42
Cole, A. A., Weisz, D. R., Dolphin, A. E., et al. 2014, ApJ, 795, 54

Crowl, H. H., Sarajedini, A., Piatti, A. E., et al. 2001, AJ, 122, 220
Cullinane, L. R., Mackey, A. D., Da Costa, G. S., et al. 2023, MNRAS, 518, L25
Dale, D. A., Anderson, K. R., Bran, L. M., et al. 2020, AJ, 159, 195
de Grijs, R., & Bono, G. 2015, AJ, 149, 179
de Grijs, R., Wicker, J. E., & Bono, G. 2014, AJ, 147, 122
De Leo, M., Carrera, R., Noël, N. E. D., et al. 2020, MNRAS, 495, 98
De Leo, M., Read, J. I., Noel, N. E. D., et al. 2023, arXiv:2303.08838
Deason, A. J., Wetzel, A. R., Garrison-Kimmel, S., et al. 2015, MNRAS, 453, 3568
del Pino, A., Łokas, E. L., Hidalgo, S. L., et al. 2017, MNRAS, 469, 4999
Di Teodoro, E. M., McClure-Griffiths, N. M., Jameson, K. E., et al. 2019, MNRAS, 483, 392
Dias, B., Angelo, M. S., Oliveira, R. A. P., et al. 2021, A&A, 647, L9
Dias, B., Kerber, L. O., Barbuy, B., et al. 2014, A&A, 561, A106
Dias, B., Parisi, M. C., Angelo, M., et al. 2022, MNRAS, 512, 4334
Diaz, J. D., & Bekki, K. 2012, ApJ, 750, 36
Dobbie, P. D., Cole, A. A., Subramaniam, A., & Keller, S. 2014a, MNRAS, 442, 1663
Dobbie, P. D., Cole, A. A., Subramaniam, A., & Keller, S. 2014b, MNRAS, 442, 1680
Dolphin, A. E. 2000, PASP, 112, 1383
Dolphin, A. E. 2002, MNRAS, 332, 91
Dolphin, A. E. 2012, ApJ, 751, 60
Dolphin, A. E. 2013, ApJ, 775, 76
Dolphin, A. E., Walker, A. R., Hodge, P. W., et al. 2001, ApJ, 562, 303
Dotter, A. 2016, ApJS, 222, 8
Duquennoy, A., & Mayor, M. 1991, A&A, 248, 485
El-Badry, K., Wetzel, A., Geha, M., et al. 2016, ApJ, 820, 131
El Youssoufi, D., Cioni, A.-L., Bell, C. P. M., et al. 2019, MNRAS, 490, 1076
El Youssoufi, D., Cioni, A.-L., Bell, C. P. M., et al. 2021, MNRAS, 505, 2020
El Youssoufi, D., Cioni, M.-R. L., Kacharov, N., et al. 2023, MNRAS, 523, 347
Engler, C., Pillepich, A., Joshi, G. D., et al. 2023, MNRAS, 522, 5946
Faria, D., Feltzing, S., Lundström, I., et al. 2007, A&A, 465, 357
Ford, H. C., Bartko, F., Bely, P. Y., et al. 1998, Proc. SPIE, 3356, 234
Foreman-Mackey, D., Hogg, D. W., Lang, D., et al. 2013, PASP, 125, 306
Fusco, F., Buonanno, R., Hidalgo, S. L., et al. 2014, A&A, 572, A26
Gaia Collaboration, Luri, X., Chemin, L., et al. 2021, A&A, 649, A7
Gaia Collaboration, Vallenari, A., Brown, A. G. A., et al. 2023, A&A, 674, A1
Gallart, C., Monelli, M., Mayer, L., et al. 2015, ApJL, 811, L18
Gallart, C., Zoccali, M., & Aparicio, A. 2005, ARA&A, 43, 387
Gatto, M., Ripepi, V., Bellazzini, M., et al. 2024, A&A, 690, A164
Geha, M., Wechsler, R. H., Mao, Y.-Y., et al. 2017, ApJ, 847, 4
Geha, M., Weisz, D., Grocholski, A., et al. 2015, ApJ, 811, 114
Geisler, D., Bica, E., Dottori, H., et al. 1997, AJ, 114, 1920
Gordon, K. D., Fouesneau, M., Arab, H., et al. 2016, ApJ, 826, 104
Grady, J., Belokurov, V., & Evans, N. W. 2021, ApJ, 909, 150
Graus, A. S., Bullock, J. S., Fitts, A., et al. 2019, MNRAS, 490, 1186
Hagen, L. M. Z., Siegel, M. H., Hoversten, E. A., et al. 2017, MNRAS, 466, 4540
Harris, C. R., Millman, K. J., van der Walt, S. J., et al. 2020, Natur, 585, 357
Harris, J., & Zaritsky, D. 2004, AJ, 127, 1531
Hatzidimitriou, D., & Hawkins, M. R. S. 1989, MNRAS, 241, 667
Hidalgo, S. L., Aparicio, A., Skillman, E., et al. 2011, ApJ, 730, 14
Hidalgo, S. L., Monelli, M., Aparicio, A., et al. 2013, ApJ, 778, 103
Hidalgo, S. L., Pietrinferni, A., Cassisi, S., et al. 2018, ApJ, 856, 125
Hill, A., & Zaritsky, D. 2006, AJ, 131, 414
Hindman, J. V., Kerr, F. J., & McGee, R. X. 1963, AuJPh, 16, 570
Holtzman, J. A., Afonso, C., & Dolphin, A. 2006, ApJS, 166, 534
Hony, S., Gouliermis, D. A., Galliano, F., et al. 2015, MNRAS, 448, 1847
Hunter, J. D. 2007, CSE, 9, 90
Jacyszyn-Dobrzeniecka, A. M., Skowron, D. M., Mróz, P., et al. 2016, AcA, 66, 149
Jacyszyn-Dobrzeniecka, A. M., Skowron, D. M., Mróz, P., et al. 2017, AcA, 67, 1
James, D., Subramanian, S., Omkumar, A. O., et al. 2021, MNRAS, 508, 5854
Jameson, K. E., Bolatto, A. D., Leroy, A. K., et al. 2016, ApJ, 825, 12
Kado-Fong, E., Greene, J. E., Huang, S., et al. 2020, ApJ, 900, 163
Kado-Fong, E., Robinson, A., Nyland, K., et al. 2024, ApJ, 963, 37
Kallivayalil, N., van der Marel, R. P., Alcock, C., et al. 2006, ApJ, 638, 772
Kimble, R. A., MacKenty, J. W., O'Connell, R. W., et al. 2008, Proc. SPIE, 7010, 70101E
Kroupa, P. 2001, MNRAS, 322, 231
Lazzarini, M., Williams, B. F., Durbin, M. J., et al. 2022, ApJ, 934, 76
Lewis, A. R., Dolphin, A. E., Dalcanton, J. J., et al. 2015, ApJ, 805, 183
Lucchini, S., D'Onghia, E., Fox, A. J., et al. 2020, Natur, 585, 203
Mackey, D., Koposov, S., Da Costa, G., et al. 2018, ApJL, 858, L21
Maia, F. F. S., Dias, B., Santos, J. F. C., et al. 2019, MNRAS, 484, 5702
Martin, G., Jackson, R. A., Kaviraj, S., et al. 2021, MNRAS, 500, 4937
Martínez-Delgado, D., Romanowsky, A. J., Gabany, R. J., et al. 2012, ApJL, 748, L24
Martínez-Delgado, D., Vivas, A. K., Grebel, E. K., et al. 2019, A&A, 631, A98
Martinez-Vazquez, C. E., Monelli, M., Bono, G., et al. 2015, MNRAS, 454, 1509
Massana, P., Nidever, D. L., & Olsen, K. 2024, MNRAS, 527, 8706
Massana, P., Noël, N. E. D., Nidever, D. L., et al. 2020, MNRAS, 498, 1034
Massana, P., Ruiz-Lara, T., Noël, N. E. D., et al. 2022, MNRAS, 513, L40
McClure-Griffiths, N. M., Dénes, H., Dickey, J. M., et al. 2018, NatAs, 2, 901
McConnachie, A. W. 2012, AJ, 144, 4
McCumber, M. P., Garnett, D. R., & Dufour, R. J. 2005, AJ, 130, 1083
McQuinn, K. B. W., Boyer, M. L., Mitchell, M. B., et al. 2017, ApJ, 834, 78
McQuinn, K. B. W., Mao, Y.-Y., Buckley, M. R., et al. 2023, ApJ, 944, 14
McQuinn, K. B. W., Skillman, E. D., Dalcanton, J. J., et al. 2012, ApJ, 759, 77
McQuinn, K. B. W., Skillman, E. D., Heilman, T. N., et al. 2018, MNRAS, 477, 3164
Meurer, G. R., Bicknell, G. V., & Gingold, R. A. 1985, PASA, 6, 195
Monelli, M., Gallart, C., Hidalgo, S. L., et al. 2010a, ApJ, 722, 1864
Monelli, M., Hidalgo, S. L., Stetson, P. B., et al. 2010b, ApJ, 720, 1225
Mucciarelli, A., Minelli, A., Bellazzini, M., et al. 2023, A&A, 671, A124
Muraveva, T., Subramanian, S., Clementini, G., et al. 2018, MNRAS, 473, 3131
Murray, C. E., Hasselquist, S., Peek, J. E. G., et al. 2024, ApJ, 962, 120
Murray, C. E., Lindberg, C. W., Merica-Jones, P. Y., et al. 2024, ApJS, 275, 5
Nidever, D. L., Majewski, S. R., & Butler Burton, W. 2008, ApJ, 679, 432
Nidever, D. L., Majewski, S. R., Muñoz, R. R., et al. 2011, ApJL, 733, L10
Nidever, D. L., Monachesi, A., Bell, E. F., et al. 2013, ApJ, 779, 145
Nidever, D. L., Olsen, K., Walker, A. R., et al. 2017, AJ, 154, 199
Niederhofer, F., Cioni, a.-L., Rubele, S., et al. 2021, MNRAS, 502, 2859
Noël, N. E. D., Aparicio, A., Gallart, C., et al. 2009, ApJ, 705, 1260
Noël, N. E. D., Conn, B. C., Carrera, R., et al. 2013, ApJ, 768, 109
Noël, N. E. D., Gallart, C., Costa, E., et al. 2007, AJ, 133, 2037
Oey, M. S., Dorigo Jones, J., Castro, N., et al. 2018, ApJL, 867, L8
Oliveira, R. A. P., Maia, F. F. S., Barbuy, B., et al. 2023, MNRAS, 524, 2244
Olsen, K. A. G., & Salyk, C. 2002, AJ, 124, 2045
Olsen, K. A. G., Zaritsky, D., Blum, R. D., et al. 2011, ApJ, 737, 29
Omkumar, A. O., Subramanian, S., Niederhofer, F., et al. 2021, MNRAS, 500, 2757
Pace, A. B., Kaplinghat, M., Kirby, E., et al. 2020, MNRAS, 495, 3022
Parisi, M. C., Geisler, D., Carraro, G., et al. 2016, AJ, 152, 58
Parisi, M. C., Geisler, D., Clariá, J. J., et al. 2015, AJ, 149, 154
Parisi, M. C., Gramajo, L. V., Geisler, D., et al. 2022, A&A, 662, A75
Parisi, M. C., Oliveira, R. A. P., Angelo, M. S., et al. 2024, MNRAS, 527, 10632
Patel, E., Besla, G., & Sohn, S. T. 2017, MNRAS, 464, 3825
Piatti, A. E. 2012, MNRAS, 422, 1109
Piatti, A. E. 2015, MNRAS, 451, 3219
Piatti, A. E., & Geisler, D. 2013, AJ, 145, 17
Piatti, A. E., Santos, J. F. C., Clariá, J. J., et al. 2005, A&A, 440, 111
Pieres, A., Santiago, B. X., Drlica-Wagner, A., et al. 2017, MNRAS, 468, 1349
Pingel, N. M., Dempsey, J., McClure-Griffiths, N. M., et al. 2022, PASA, 39, e005
Povick, J. T., Nidever, D. L., Massana, P., et al. 2023, arXiv:2310.14299
Privon, G. C., Stierwalt, S., Patton, D. R., et al. 2017, ApJ, 846, 74
Radburn-Smith, D. J., Roškar, R., Debattista, V. P., et al. 2012, ApJ, 753, 138
Ramachandran, V., Oskinova, L. M., & Hamann, W.-R. 2021, A&A, 646, A16
Rezaei kh, S., Javadi, A., Khosroshahi, H., et al. 2014, MNRAS, 445, 2214
Ripepi, V., Cioni, M.-R. L., Moretti, M. I., et al. 2017, MNRAS, 472, 808
Roman-Duval, J., Proffitt, C. R., Taylor, J. M., et al. 2020, RNAAS, 4, 205
Rubele, S., Girardi, L., Kerber, L., et al. 2015, MNRAS, 449, 639
Rubele, S., Pastorelli, G., Girardi, L., et al. 2018, MNRAS, 478, 5017
Ruiz-Lara, T., Gallart, C., Monelli, M., et al. 2021, MNRAS, 501, 3962
Rusakov, V., Monelli, M., Gallart, C., et al. 2021, MNRAS, 502, 642
Sabbi, E., Gallagher, J. S., Tosi, M., et al. 2009, ApJ, 703, 721
Sacchi, E., Cignoni, M., Aloisi, A., et al. 2018, ApJ, 857, 63
Sakowska, J. D., Noël, N. E. D., Ruiz-Lara, T., et al. 2024, MNRAS, 532, 4272
Santana, F. A., Muñoz, R. R., de Boer, T. J. L., et al. 2016, ApJ, 829, 86
Savino, A., Weisz, D. R., Skillman, E. D., et al. 2023, ApJ, 956, 86
Schlafly, E. F., & Finkbeiner, D. P. 2011, ApJ, 737, 103
Shapley, H. 1940, BHarO, 914, 8
Skibba, R. A., Engelbracht, C. W., Aniano, G., et al. 2012, ApJ, 761, 42
Skillman, E. D., Hidalgo, S. L., Weisz, D. R., et al. 2014, ApJ, 786, 44

Skillman, E. D., Monelli, M., Weisz, D. R., et al. 2017, ApJ, 837, 102
Skowron, D. M., Skowron, J., Udalski, A., et al. 2021, ApJS, 252, 23
Stanimirović, S., Staveley-Smith, L., & Jones, P. A. 2004, ApJ, 604, 176
Staudaher, S. M., Dale, D. A., & van Zee, L. 2019, MNRAS, 486, 1995
Stierwalt, S., Besla, G., Patton, D., et al. 2015, ApJ, 805, 2
Stierwalt, S., Liss, S. E., Johnson, K. E., et al. 2017, NatAs, 1, 0025
Stinson, G. S., Dalcanton, J. J., Quinn, T., et al. 2009, MNRAS, 395, 1455
Subramanian, S., Rubele, S., Sun, N.-C., et al. 2017, MNRAS, 467, 2980
Subramanian, S., & Subramaniam, A. 2009, A&A, 496, 399
Subramanian, S., & Subramaniam, A. 2012, ApJ, 744, 128
Tatton, B. L., van Loon, J. T., Cioni, M.-R. L., et al. 2021, MNRAS, 504, 2983
Tolstoy, E., Hill, V., & Tosi, M. 2009, ARA&A, 47, 371
Trauger, J. T., Ballester, G. E., Burrows, C. J., et al. 1994, ApJL, 435, L3
Vasiliev, E. 2024, MNRAS, 527, 437
Weisz, D. R., Dalcanton, J. J., Williams, B. F., et al. 2011, ApJ, 739, 5
Weisz, D. R., Dolphin, A. E., Skillman, E. D., et al. 2013, MNRAS, 431, 364
Weisz, D. R., Dolphin, A. E., Skillman, E. D., et al. 2014, ApJ, 789, 147
Weisz, D. R., Dolphin, A. E., Skillman, E. D., et al. 2015, ApJ, 804, 136
Wetzel, A. R., Deason, A. J., & Garrison-Kimmel, S. 2015, ApJ, 807, 49
Wetzel, A. R., Tollerud, E. J., & Weisz, D. R. 2015, ApJL, 808, L27
Williams, B. F., Dalcanton, J. J., Dolphin, A. E., et al. 2009, ApJL, 695, L15
Williams, B. F., Dalcanton, J. J., Johnson, L. C., et al. 2011, ApJL, 734, L22
Williams, B. F., Dolphin, A. E., Dalcanton, J. J., et al. 2017, ApJ, 846, 145
Williams, B. F., Durbin, M. J., Dalcanton, J. J., et al. 2021, ApJS, 253, 53
Williams, B. F., Lang, D., Dalcanton, J. J., et al. 2014, ApJS, 215, 9
Williams, M. L., Bekki, K., & McKenzie, M. 2022, MNRAS, 512, 4086
Yanchulova Merica-Jones, P., Sandstrom, K. M., Johnson, L. C., et al. 2021, ApJ, 907, 50
Zaritsky, D., Harris, J., Grebel, E. K., et al. 2000, ApJL, 534, L53
Zhang, S., Mackey, D., & Da Costa, G. S. 2021, MNRAS, 508, 2098
Zivick, P., Kallivayalil, N., Besla, G., et al. 2019, ApJ, 874, 78
Zivick, P., Kallivayalil, N., & van der Marel, R. P. 2021, ApJ, 910, 36
Zivick, P., Kallivayalil, N., van der Marel, R. P., et al. 2018, ApJ, 864, 55